5-2018

Grid-connected photovoltaic systems based on nonlinear control.

Pablo R. Rivera
University of Louisville

Recommended Citation

GRID-CONNECTED PHOTOVOLTAIC SYSTEMS BASED ON NONLINEAR
CONTROL

By

Pablo R. Rivera
B.S., National Polytechnic University, 1986
M.S., University of Bradford, 1993

A Dissertation
Submitted to the Faculty of the
J. B. Speed School of the University of Louisville
in Partial Fulfillment of the Requirements
for the Degree of

Doctor of Philosophy
in Electrical Engineering

Department of Electrical and Computer Engineering
University of Louisville
Louisville, Kentucky

May 2018

GRID-CONNECTED PHOTOVOLTAIC SYSTEMS BASED ON NONLINEAR
CONTROL

By

Pablo R. Rivera
B.S., National Polytechnic School, 1986
M.S., University of Bradford, 1993

A Dissertation Approved On

March 2, 2018

by the following Dissertation Committee:

_____

Michael L. McIntyre (Dissertation Director)

_____

Tamer Inanc

_____

Robert Cohn

_____

Christopher Richards

ACKNOWLEDGMENTS

I would like to thanks to Dr. Michael McIntyre, my thesis supervisor, for his guidance and support on succeeding with this research work. My thanks to Dr. Robert Cohn, Dr. Tamer Inanc and Dr. Christopher Richards, committee members, for the time they dedicated to read and review this dissertation. I would also like to express my special appreciation to Dr. Robert Cohn for his assistance and advice to pursue the Ph.D. studies.

ABSTRACT

GRID-CONNECTED PHOTOVOLTAIC SYSTEMS BASED ON NONLINEAR

CONTROL

Pablo R. Rivera

March 2, 2018

Solar energy, considered as abundant and clean renewable energy source, has been utilized for a variety of applications such as generation of electricity for low and medium power. Nowadays, due to the high-scale penetration of photovoltaic systems, reliable and efficient grid-connected photovoltaic (PV) systems using the advances of power electronics and control system technology are desirable. Thus, single-stage grid-connected photovoltaic systems, have gained attention, especially in low voltage applications. However, PV systems exhibit nonlinear behavior due to the intrinsic features of the PV cell and nonlinear switching functions of the inverter that could negatively affect the performance of the system if they are not adequately compensated for. In this dissertation, using the general structure for the synchronous $dq0$ frame, a single-stage three-phase grid-connected photovoltaic inverter with a nonlinear control strategy is developed to track the maximum power regardless of the atmospheric conditions and to control the active and reactive power without the necessity of an additional power converter. A novel trajectory of the reference current is obtained online taking into account the dynamics of the DC link capacitor and the switching function of the inverter.

Furthermore, due to increased penetration of low-power single-phase PV systems in residential applications, a single-stage single-phase grid-connected PV system with a nonlinear control strategy is proposed in this dissertation. Unlike to the three-phase system, the single-phase system includes a novel method to mitigate the double line-frequency current ripple of the PV array, which is the major drawback of the single-phase PV inverter. Moreover, based on the preceded work, the nonlinear controller is combined with adaptive control to estimate the unknown disturbances that physically could appear in the circuit and affect the performance of the system.

Additionally, in this study, the stability of the system and boundedness of signals of the closed-loop system are demonstrated by Lyapunov stability analysis for both the three-phase system and the single-phase system respectively. Simulation results show the effectiveness and robustness of the proposed controllers to track the maximum power and to control the active and reactive power to sudden changes in the atmospheric conditions and changes in the load.

TABLE OF CONTENTS

LIST OF TABLES

LIST OF FIGURES

CHAPTER I

INTRODUCTION

Solar energy is the most abundant and the cleanest renewable energy source available in the world, technically ready to use for a variety of applications, such as the generation of electricity for residential, commercial, or industrial consumption [1], [2]. It has become an essential part of modern energy systems due to the reduction in the photovoltaic (PV) module costs and the evolution of the classic power converter from the point of view of efficiency, reliability, and costs [2]. Power electronics technology has become an important component in distributed generation (DG) and in facilitating the incorporation of renewable energy sources into the grid [3].

Photovoltaic converters are widely used to convert the DC voltage generated by the PV array to AC voltage. Two-stage power conversion is currently the most common approach to cope with the DC voltage range produced by the PV panel [2]. This configuration consists of a DC-DC power converter, which achieves maximum power point tracking (MPPT) in combination with maximum power point (MPP) algorithms and a DC-AC power converter stage to supply power to the grid or the grid and local loads. Well-known control approaches such as Perturb and Observe (P&O), Incremental Conductance (INC), Constant Voltage (CV) algorithms, and improved versions of them have been developed to track the MPP operation as in [17]-[23]. Multiple-stage power conversion systems decrease the overall energy efficiency and reliability of the PV

installation besides increasing the cost [2], [4]. Therefore, from the point of view of efficiency and reliability, single-stage grid-connected photovoltaic systems, which consist of a PV array and a DC-AC converter with MPPT, have been reported in some papers to control the active power and reactive power using conventional linear control techniques as in [4] – [12]. Most of the studies have been developed for three-phase systems, which are widely utilized in PV systems but, due to the high-scale penetration of low-power single-phase PV systems, in last years some researchers have aimed their studies to single-phase systems not only from the efficiency and reliability point of view but also for grid support. Giving grid support could alleviate the adverse effects that could cause disconnecting the PV system from the grid in case of a grid fault as is required by current grid standards of some countries (for instance the IEEE 1547 standard) [60]. In [60] it is stated that in the near future PV systems should become more dynamic with functionalities such as low-voltage ride-through (LVRT) and grid support capability. However, to date, current grid standards of some countries are still in effect and should be revised [16], [42] to enable such additional functionalities for PV systems.

PV systems exhibit nonlinear behavior due to the intrinsic features of the PV cell and nonlinear switching functions of the inverter [24] that could negatively affect the performance of the system if they are not adequately compensated. Since nonlinear controllers deal with nonlinearities directly [51], in the literature, there are some advanced and efficient nonlinear control techniques and schemes applied to grid-connected PV systems. Techniques such as backstepping control, sliding control, and feedback linearization, have been presented in [24]-[39]. Most of those studies involve the two-stage topology either for three-phase or single-phase systems.

2

For the case of two-stage topology, a three-phase system with a nonlinear backstepping controller to inject active and reactive power to the grid is presented in [24]. The scheme proposed in [24] is classified as a two-stage power converter because it uses a DC-DC converter to regulate the voltage of the DC link capacitor ensuring MPPT as a first stage, and a three-phase inverter to control the active and reactive power injected to the grid as a second stage. In [25], [26], [27], and [28] describe a two-stage single-phase grid-connected PV system based on backstepping control for power factor correction and maximum power tracking. These works utilize a DC-DC boost converter to track the maximum power from the PV array and to regulate the input voltage to the inverter, and a single-phase full-bridge DC-AC converter (inverter) to supply active power with unity power factor on the grid side. The principal difference between these works is the way in which the input voltage to the inverter is regulated. In [25] the squared output voltage of the DC-DC converter tracks a given squared reference voltage, which reference voltage is a given value higher than the peak voltage of the grid. In [26] and [28] a PI controller is utilized to regulate the output voltage of the DC-DC boost converter. In [27], the derivative of the squared output voltage of the DC-DC converter is modeled as an integrator perturbed with a cosine signal of double frequency to track the output reference voltage and to reject any disturbance.

In [29] a two-stage three-phase system based on sliding control technique is described. The first stage is a DC-DC converter with a coupled inductor topology for voltage boosting. It applies the adaptive sliding surface for MPP tracking. A DC-AC three-phase converter for power factor correction forms the second stage. In [30] is presented a sliding control for a PV system. The sliding controller of a boost converter

3

drives the PV voltage to follow the reference voltage obtained from an MPPT algorithm. The sliding surface is designed taking into account the voltage dynamics of the DC link capacitor, which voltage derivative is acquired by measuring the capacitor current. However, this method to obtain the capacitor current could be a cause of divide-by-zero singularity problems [31]. The sliding control is a robust control technique that deals with model uncertainties. Nevertheless, the sliding mode controller generates a very harsh switching control input [32], which results in chattering phenomenon, which is undesirable for power electronic systems.

The linearization technique transforms the nonlinear system into a full or partial linear equivalent by canceling the nonlinearities. Then, linearizing the states equations, the controller can be designed for either stabilization or tracking purposes [51]. Some works related to PV system applications have been reported applying the linearization technique. A two-stage three-phase inverter based on linearization technique to inject maximum power into the grid from the PV array is presented in [33]. However, the linearization technique could lead to stability issues when the parameters of the system vary, or the operating conditions change.

Two-stages PV systems based on nonlinear control techniques have shown good performance. Still, two-stage power conversion system reduces the overall energy efficiency and reliability of the PV system besides increasing the cost [2]. To date, only a few works have been reported for single-stage power conversion applying nonlinear control techniques. In [34], a partial feedback linearization technique for three-phase systems is presented considering uncertainties of the PV system model. Based on the same control technique, in [35] is reported a nonlinear current control scheme for a single-phase

grid-connected photovoltaic (PV) system. In [36] an input-output feedback linearization technique for a three-phase inverter modeled in *dq0* reference frame is presented. All these works based on feedback linearization have obtained the desired results. However, the feedback linearization technique is susceptible to the variation of parameters [24].

In [31] is proposed a sliding mode controller for a single-stage single-phase grid-connected photovoltaic system. The sliding surface is designed using the error of the inductor current. An MPPT algorithm generates the power reference instead of the voltage reference. Therefore, the sliding surface is designed to control both the inductor current and the PV power. The reference current is obtained as a function of the reference power based on the power-balance relationship. A similar controller is presented in [37] for a single-stage three-phase grid-connected photovoltaic system. In this case, the three-phase system is analyzed in *dq0* reference frame. As it was mentioned, the sliding mode controller has robust control property under parameters uncertainties; however, determination of the sliding surface is a harsh command [32].

An ideal averaged model of a single-stage three-phase PV system is reported in [38]. It uses a nonlinear backstepping controller to control only the active power, but it does not consider the exact switching topology of the system [24]. In [38] is presented a new technique to achieve MPP using an optimal voltage reference generator, which voltage regulation involves the squared DC voltage. In [39], a single-stage three-phase grid-connected PV system using a Lyapunov-based nonlinear control to manage the active power is presented. The research presented in [39] does not take into account the voltage dynamics of the DC link capacitor, which includes nonlinearities due to the switching functions of the inverter. The voltage dynamics of the DC link capacitor could lead to

oscillation of the DC link voltage or injection of non-sinusoidal current to the grid if they are not incorporated therefore affecting the efficiency and the power quality.

In this dissertation, using a single-stage three-phase grid-connected photovoltaic system a nonlinear control strategy based on Lyapunov analysis is proposed. The controller is designed to achieve maximum power point operation regardless of the atmospheric conditions without the necessity of a DC-DC converter and to control the active and reactive power, thus to guarantee unity power factor on the grid side. The voltage dynamics of the DC link capacitor that contains the switching function of the inverter are considered in the design of the nonlinear controller. For that, a novel method to obtain the reference current taking into account the voltage dynamics of the DC link capacitor is developed. The structure for synchronous *dq0* frame control configuration is adopted in this dissertation because the control variables become constant values, therefore facilitating the design of the controller [40]. Furthermore, the Incremental Conductance algorithm is utilized in this research based on its applications, performance, and reliability [19], [20] to track the MPP operation, thus to obtain the reference voltage regardless of the atmospheric conditions. Moreover, a Lyapunov analysis is developed to prove the stability of the system and boundedness of the signals in the closed-loop system. Simulations results demonstrate the control objectives are met along with the effectiveness and robustness of the nonlinear controller in the proposed control scheme.

Nowadays, the PV market has been dominated by residential applications with low-power single-phase PV systems [42]. From the point of view of efficiency, cost, and size, single-stage inverters have gained attention, especially in low voltage applications [9]. Unlike the three-phase grid-connected PV system, the single-phase PV system has an AC

component of double line frequency on the DC bus. This AC component negatively affects the PV voltage causing a deviation from the voltage at maximum power point (Vmpp); therefore, it can result in a reduction of the efficiency [43]. The use of two-stage power converter decreases the negative effect of the DC bus voltage ripple that could perturb the maximum power point operation of the solar array [44]. In a single-stage converter, the 120 Hz current ripple is filtered by the DC link capacitor, but an important amount of the current ripple could propagate to the solar array as in the two-stage topology [45]. Based on the voltage cancelation principle presented by [44] for two-stage power conversion, in this dissertation, it is proposed a novel method to mitigate the current ripple without the necessity of a DC-DC converter. Moreover, the proposed nonlinear control approach; developed for the three-phase system using the *dq0* frame, is applied in the single-phase topology to obtain maximum power and to control the active and reactive power supplied to the grid. However, the *dq0* transformation method utilized in the three-phase system is not straightforward for single-phase systems. Then, the method proposed in [46] is adopted in this dissertation to obtain the model of the single-phase system in *dq* frame. Additionally, based on the preceded work, the nonlinear controller is combined with adaptive control to adaptively estimate the unknown disturbances that physically appear in the circuit such as imperfect switching timing [41]. The stability of the control algorithm is verified by Lyapunov analysis. Simulations results demonstrate the effectiveness and robustness of the nonlinear control schemes.

The rest of this work is organized as follows: In Chapter II an overview of photovoltaic systems is detailed. This section covers the characteristics of the PV array and a brief analysis of the configurations used in PV systems. In addition, this chapter

contains the description of the Incremental Conductance algorithm utilized in this work for maximum power point tracking. Moreover, the basis of the control system for grid-connected PV systems is explained in this section. Chapter III covers the model of the three-phase grid-connected inverter in *abc* frame along with the transformation of the system to *dq0* frame considering the cross-coupling dependence of the active and reactive power that appear due to the *dq0* transformation. Chapter IV contains the development of the controller to obtain maximum power point operation and to control the active and reactive power based on Lyapunov theory. Additionally, a new trajectory of the reference current to control the active power is developed. Furthermore, this chapter contains the stability analysis based on Lyapunov theorems to show the convergence of the error signals of current and voltage. Simulation results of the proposed scheme are shown in this chapter. Chapter V covers the analysis of the single-phase system model including the proposed approach to mitigate the current ripple. The model of the single-phase system in *dq* frame including the current ripple mitigation is developed in this section. Chapter VI covers the design of the control signals to achieve maximum power point operation and to control the active and reactive power in a single-phase scheme based on Lyapunov approach. Additionally, this chapter contains the design of the new trajectory to obtain the reference current considering the current ripple. Furthermore, the stability analysis of the proposed controller is reported in this section. Simulation results are shown in this chapter to validate the proposed approach to mitigate the current ripple and to confirm the effectiveness of the proposed controller. Chapter VII covers the design of the nonlinear controller combined with adaptive control to estimate the unknown disturbances that physically could appear in the circuit and negatively affect the

performance of the system. A Lyapunov analysis is developed to show the stability and boundedness of the signals in the closed loop system. Simulation results validate the performance and robustness of the controller when unknown disturbances appear in the circuit. Finally, Chapter VIII contains the conclusions.

CHAPTER II

OVERVIEW OF PHOTOVOLTAIC SYSTEMS

2.1 PV Array System Model

PV arrays exhibit nonlinear characteristics, which change as the irradiation and temperature change. A variety of models of PV cells has been reported in the literature for MPPT. An equivalent circuit of the PV cell model; known as a single-diode model, is shown in Figure 2.1 [47].
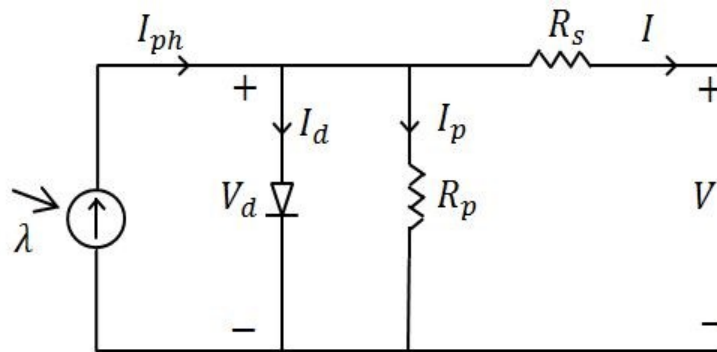
Figure 2.1 Solar cell equivalent circuit

The equations that represent the current-voltage (I-V) characteristics are as follows [5]:

$$I = I_{ph} - I_d - \frac{V_d}{R_p} \qquad (2\text{-}1)$$

$$V_d = IR_s + V \tag{2-2}$$

$$I_d = I_0 \left[exp\left(\frac{qV_d}{AKT}\right) - 1 \right] \tag{2-3}$$

$$I_{ph} = [I_{sc} + K_l(T - T_r)]\lambda \tag{2-4}$$

where I_{ph} is the photocurrent, I_d is the average current through the diode, and V_d is the average voltage of the photovoltaic cell. I_0 is the reverse saturation current at the reference temperature T_r [5], A is the diode ideal factor, T is the solar cell panel temperature in absolute scale (^oK), I_{sc} is the short circuit current at the reference temperature and radiation, K_l is the short circuit current temperature coefficient, and λ is the solar radiation. K is the Boltzmann constant $= 1.38x10^{-23}J/\,^oK$, q is the electron charge $q = 1.6x10^{-19}$ Coulombs.

The current-voltage and power-voltage characteristics of a PV module for various values of irradiance at 25 ^{o}C are shown in Fig. 2.2, and the characteristics of the PV module for various values of temperature at 1000 W/m^2 are shown in Figure 2.3. Depending on the power rate, the PV array consists of strings of N_p photovoltaic modules connected in parallel. Each string consists of N_s modules connected in series. Then, the output voltage V_{pv} and output current I_{pv} of the PV array are given by the following equations:

$$V_{pv} = N_s(V_d - IR_s) \tag{2-5}$$

$$I_{pv} = N_p I \tag{2-6}$$

$$P_{pv} = V_{pv}I_{pv}. \tag{2-7}$$
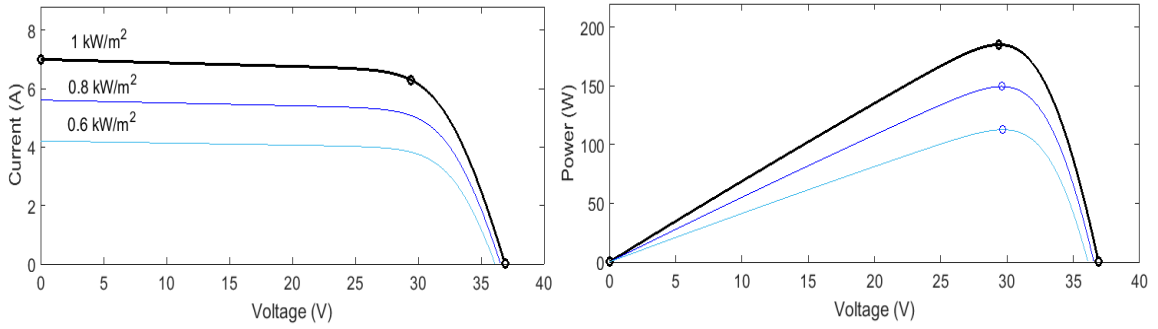
Figure 2.2 Solar cell characteristics at 25 $^{\circ}$C
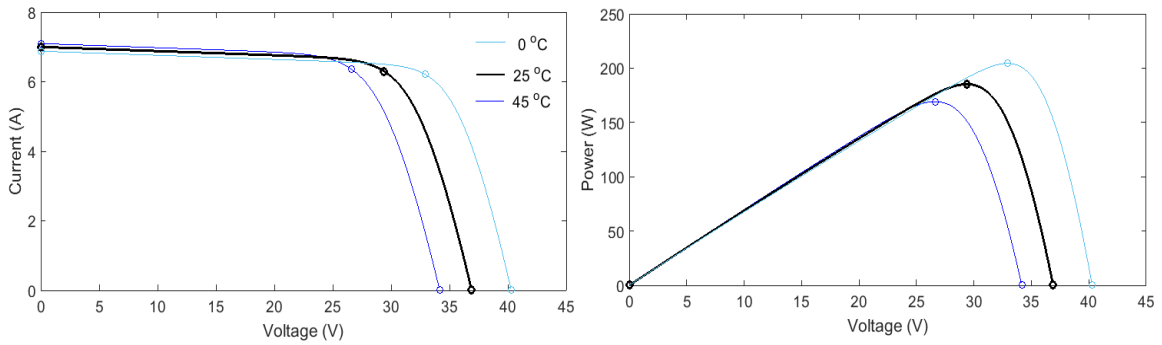
Figure 2.3 Solar cell characteristics at 1000 W/m^2

Due to shadowing or anything obstructing the PV module, connections of PV modules in series and parallel could lead to decrease the efficiency of the PV module and therefore of the PV array [48]. One way of mitigating the effect of shadows is to connect bypass diodes, but they do not solve the issue entirely [49].

For grid-connected PV systems applications, it is necessary to have an interface between the PV array and the grid to regulate the PV voltage thus to obtain the maximum power of the PV array and to inject sinusoidal current to the grid. The configurations shown in Figure 2.4 are used to achieve these requirements [50]:
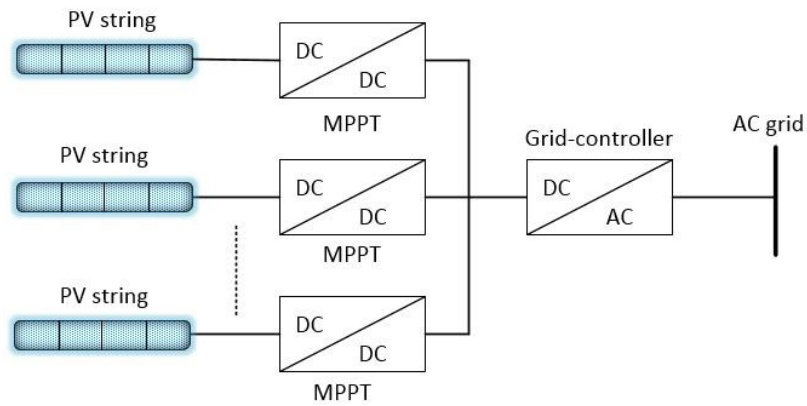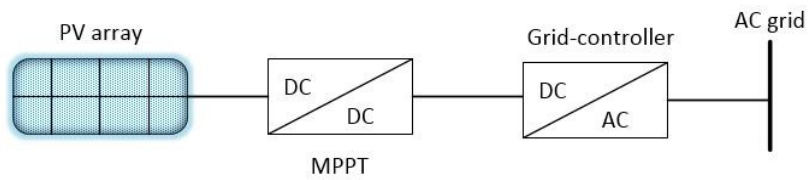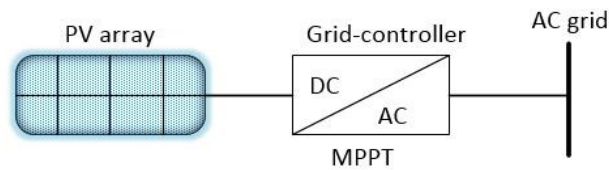
Figure 2.4 a) Multi-stage, b) Two-stage, c) Single-stage PV systems configurations

From efficiency and reliability point of view, single-stage PV systems; as is shown in Figure 2.4 c), have gained attention in the research world. Single-stage PV systems have been reported by researchers using many circuits topologies and different control approaches to managing the active and reactive power of grid-connected PV systems with MPPT. Depending on the range of the electric power, PV systems are classified as three-

phase or single-phase systems. For low power application of about few kilowatts, single-phase PV systems are required to operate at unity power factor (PF) with maximum power point tracking [42].

The power generated by the PV system has to supply the grid or local loads and the grid when the PV system output power is greater than the load demand. The active power flow direction; on the grid side, depends on the power generated by the PV system or on the power required by the load. Figure 2.5 shows the power flow when it is required to have unity power factor on the grid side according to current grid standard for low and medium power applications.
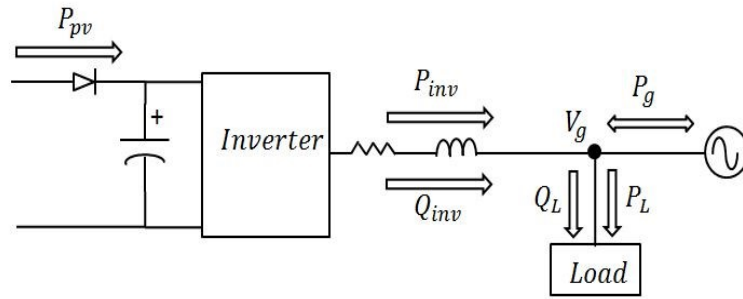
Figure 2.5 Power flow of the PV system for unity power factor

The total active power and reactive power of a three-phase grid-connected voltage source inverter (VSI), considering the *dq0* reference frame are given by the following equations [4]:

$$P_g = \frac{3}{2}\left(V_{gd}I_d + V_{gq}I_q\right) \tag{2-8}$$

$$Q_g = \frac{3}{2}\left(V_{gd}I_q - V_{gq}I_d\right) \tag{2-9}$$

14

where, V_{gd} and V_{gq} are the *d*-axis and *q*-axis voltage components of the grid, and I_d and I_q are the *d*-axis and *q*-axis current components of the inverter. The voltage of the grid is assumed to be a zero averaged sinusoid with low harmonic components. Therefore, the *q*-axis component of the grid voltage $V_{gq} = 0$, then:

$$P_g = \frac{3}{2}\left(V_{gd}I_d\right) \qquad (2\text{-}10)$$

$$Q_g = \frac{3}{2}\left(V_{gd}I_q\right). \qquad (2\text{-}11)$$

Considering the inverter as lossless and dismissing the power loss on the filter inductor, the steady state PV power given by Eq. (2-7) is equal to the active power of the grid given by Eq. (2-10) for three-phase systems, thus:

$$V_{pv}I_{pv} = \frac{3}{2}\left(V_{gd}I_d\right). \qquad (2\text{-}12)$$

For single-phase systems, the active power and reactive power of the grid, and power of the PV array are as follows:

$$P_g = \frac{1}{2}\left(V_{gd}I_d\right) \qquad (2\text{-}13)$$

$$Q_g = \frac{1}{2}\left(V_{gd}I_q\right) \qquad (2\text{-}14)$$

$$V_{pv}I_{pv} = \frac{1}{2}\left(V_{gd}I_d\right). \qquad (2\text{-}15)$$

2.2   Maximum Power Point Tracking Algorithm

An MPPT algorithm is required to match the solar PV power to changes in the atmospheric conditions and operate to obtain maximum power. The Incremental

Conductance algorithm is utilized in this dissertation based on its applications, performance, and reliability to track the MPP operation and hence to obtain the reference voltage regardless of the atmospheric conditions [19], [20]. For a PV array, the derivative of the output power with its voltage is given by the following equation [19]:

$$\frac{dP}{dV} = \frac{d(IV)}{dV} = I + \frac{VdI}{dV}.$$

(2-16)

Then, Eq. (2-16) can be written as:

$$\frac{dP}{dV} \approx I + \frac{V\Delta I}{\Delta V}.$$

(2-17)

The solution of Eq. (2-17) is zero at MPP, positive on the left of the MPP, and negative on the right of the MPP. Therefore, Eq. (2-17) can be expressed as:

$$\begin{cases} I + \dfrac{\Delta I}{\Delta V}V = 0 \quad at\ MPP \\ I + \dfrac{\Delta I}{\Delta V}V > 0 \ at\ left\ of\ MPP \\ I + \dfrac{\Delta I}{\Delta V}V < 0 \ at\ right\ of\ MPP. \end{cases}$$

(2-18)
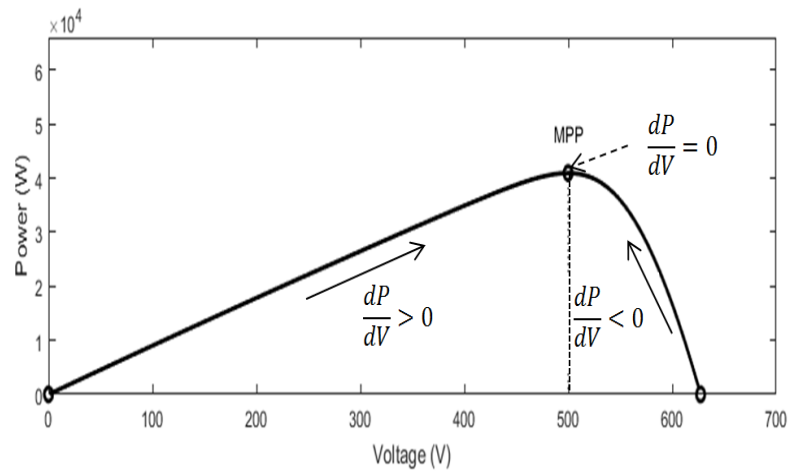
Figure 2.6 Power and voltage variation for Incremental Conductance algorithm [20]

16

As it is shown in Figure 2.6, if the MPP lies on the right side, the reference voltage must decrease to reach the MPP. On the other hand, if MPP lies on the left side, the reference voltage must increase to reach the MPP. Moreover, when a change in ΔI is presented, the algorithm decrements the voltage if $\Delta I > 0$ or it increments the voltage if $\Delta I < 0$ to track the new MPP. In this work, the reference voltage, required as a part of controller design, is directly obtained from the INC algorithm. The initial operating point of the reference voltage is set at 80% the open circuit voltage (Voc) of the PV array [21] during the first cycle to avoid misleading of the MPP. As soon the MPP is reached, the output voltage of the solar array oscillates around the ideal operating point voltage. Since in this work the INC algorithm is applied with fixed step size, the step size of the voltage (v_{step}) was obtained by trial – error method to find a satisfactory working point between the dynamics and steady-state oscillation [19].

2.3   Control System for Grid-Connected PV Systems

Grid-connected PV systems need a power-conditioning unit to be connected between the PV array and the grid. These systems are designed to operate in parallel with the grid as is shown in Figure 2.7 [1]. An MPPT scheme, the power converter, the grid interface, and the control system compose the power conditioning. For grid-connected PV applications, the control system is designed to obtain a good performance of the PV system with maximum power point operation and low total harmonic distortion of the grid current with unity power factor on the grid side [1]. The MPPT scheme finds the voltage or current at maximum power point at which the PV array should work to extract

17

the maximum power despite the atmospheric conditions. The power converter changes the DC current generated by the PV array to AC current. In the two-stage topology, a DC-DC converter generally performs the MPP operation and sometimes voltage boosting, and a DC-AC converter changes the DC current to AC current with unity power factor for grid-connected systems. In a single-stage topology, a DC-AC converter is utilized to track the MPP, to change the DC current generated by the PV array to AC current, and to control the active and reactive power supplied to the grid. The grid interface is utilized to filter the high frequency components of the AC inverter current and obtain an AC current with low total harmonic distortion to be injected into the grid.
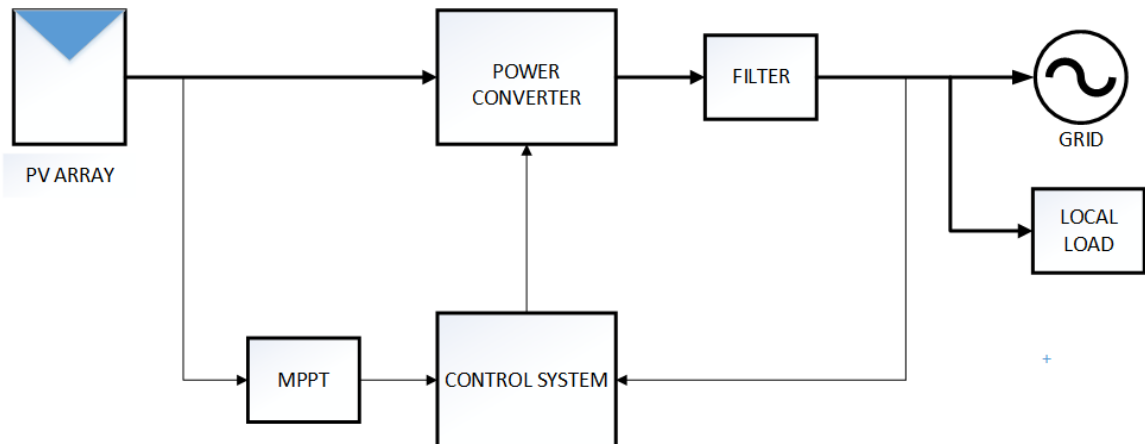
Figure 2.7 Block diagram of a grid-connected PV system

Classical linear control techniques such as PI controller, Proportional Resonant (PR) controller, Hysteresis controller, and Predictive controller have been presented in [4]-[14] for grid-connected PV applications. PV systems exhibit nonlinear behavior due to the intrinsic features of the PV cell and nonlinear switching function of the DC-AC converter [34]. Since these nonlinearities could negatively affect the performance of the

18

system if they are not adequately compensated for, new control solutions have been proposed using advanced nonlinear control techniques such as feedback linearization, sliding-mode control, and backstepping control. The backstepping control technique has shown good tracking performance, stability and system dynamics in standalone inverters [41].

The tasks of the control system are divided into two categories; i) stabilization and ii) tracking [51]. In a stabilization problem, the control system is designed so that the state of the closed-loop system is stabilized around the equilibrium point of the system. In tracking control problem, the objective is to build a controller so that the output of the system tracks the desired trajectory keeping the entire system stabilized. Since tracking problem covers stabilization problem, it is more challenging to solve a tracking problem than stabilization problem [51]. The Lyapunov theory is based on mathematical concepts so that if a differentiable function is positive definite and its time derivative is negative or zero, then the function will decrease to zero or some positive constant [54]. Based on this theory, the control law, which is composed of a feedforward and a feedback parts, is designed to track the desired trajectory along with stabilizing the system. The feedforward part provides the needed input for following the desired trajectory and canceling the effects of known disturbances, while the feedback part stabilizes the tracking error dynamics [51]. The basis of Lyapunov theory can be found in nonlinear control systems reference books as in [51]-[53].

CHAPTER III

SINGLE-STAGE THREE-PHASE GRID-CONNECTED PHOTOVOLTAIC
SYSTEMS

3.1   Three-Phase Inverter System Model

A single-stage three-phase grid-connected photovoltaic system, as is shown in Figure 3.1, is used to control the active and the reactive grid power while achieving maximum power point tracking of the PV array. In this work, a three-phase Voltage Source Inverter (VSI) with the Space Vector PWM technique is utilized because the voltage stress and losses in the switching devices are reduced [5]. Moreover, the voltage of the PV array is chosen to be greater than the peak voltage of the grid [1] to be able to control the active and the reactive power without the necessity of a DC-DC boost stage.
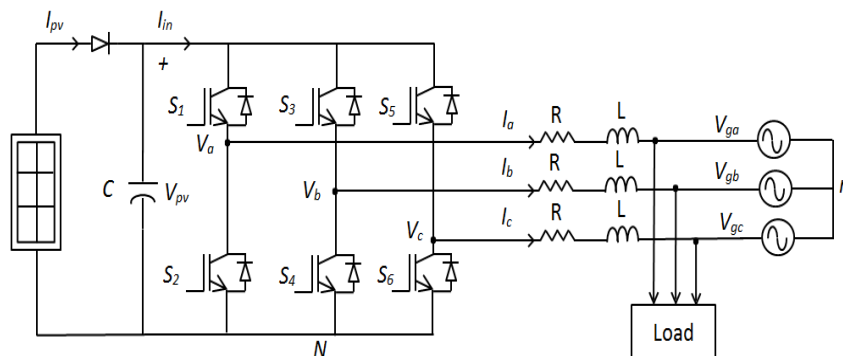
Figure 3.1 Three-phase PV system with output filter R-L

From Figure 3.1, the equations that represent the dynamic analytical model in *abc* frame are as follows:

$$v_{aN} = L\frac{di_a}{dt} + Ri_a + v_{ga} + v_{com} \tag{3-1}$$

$$v_{bN} = L\frac{di_b}{dt} + Ri_b + v_{gb} + v_{com} \tag{3-2}$$

$$v_{cN} = L\frac{di_c}{dt} + Ri_c + v_{gc} + v_{com} \tag{3-3}$$

$$I_{pv} = C\frac{dv_{pv}}{dt} + I_{in} \tag{3-4}$$

where R and L are the equivalent series resistance and inductance of the output filter and the grid supply respectively, C is the capacitance of the input filter of the inverter, v_{com} is the DC common mode voltage between the neutral point $\boldsymbol{n}$ and the negative point N, v_{ga}, v_{gb}, v_{gc} are the phase voltages of the grid, i_a, i_b, i_c are the phase output currents of the inverter, I_{in} is the input current to the inverter. Assuming that v_{an}, v_{bn}, v_{cn} are the three-phase switching-average voltages to be synthesized [56], which are sinusoidal and they are lagging each other by 120 degrees, and the grid frequency is much lower than the switching frequency [4], the DC common mode voltage v_{com} is given by the following equation

$$v_{com} = \frac{1}{3}(v_{aN} + v_{bN} + v_{cN}). \tag{3-5}$$

The control functions $d_1, d_2,$ and d_3 of the scheme shown in Figure 3.2 are defined by the following equations [56]:

$$d_1 = \frac{v_{aN}}{V_{pv}}, d_2 = \frac{v_{bN}}{V_{pv}}, d_3 = \frac{v_{cN}}{V_{pv}}. \tag{3-6}$$

From Figure 3.2, the input current to the inverter is given by:

$$I_{in} = d_1 i_a + d_2 i_b + d_3 i_c. \tag{3-7}$$
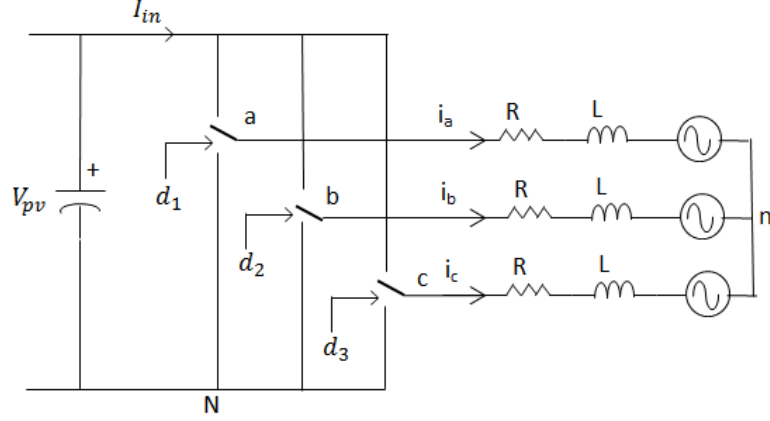
Figure 3.2 Equivalent circuit of the switch-mode three-phase inverter [56]

Substituting Eq. (3-5) and Eq. (3-6) into equations (3-1), (3-2), and (3-3), and Eq. (3-7) into Eq. (3-4), the equations that represent the state-space model of the system in *abc* frame are obtained:

$$\frac{di_a}{dt} = -\frac{R}{L} i_a + \frac{V_{pv}}{3L}(2d_1 - d_2 - d_3) - \frac{1}{L} v_{ga} \tag{3-8}$$

$$\frac{di_b}{dt} = -\frac{R}{L} i_b + \frac{V_{pv}}{3L}(-d_1 + 2d_2 - d_3) - \frac{1}{L} v_{gb} \tag{3-9}$$

$$\frac{di_c}{dt} = -\frac{R}{L} i_c + \frac{V_{pv}}{3L}(-d_1 - d_2 + 2d_3) - \frac{1}{L} v_{gc} \tag{3-10}$$

$$\frac{dV_{pv}}{dt} = \frac{1}{C} I_{pv} - \frac{1}{C}(d_1 i_a + d_2 i_b + d_3 i_c) \tag{3-11}$$

From equations (3-8), (3-9), and (3-10), the relationship between the switching function vectors $[d_1 \quad d_2 \quad d_3]^T$ and the phase-voltages can be expressed as follows:

22

$$\begin{bmatrix} v_{an} \\ v_{bn} \\ v_{cn} \end{bmatrix} = \frac{V_{pv}}{3} \begin{bmatrix} 2 & -1 & -1 \\ -1 & 2 & -1 \\ -1 & -1 & 2 \end{bmatrix} \begin{bmatrix} d_1 \\ d_2 \\ d_3 \end{bmatrix} \qquad (3\text{-}12)$$

where d_1, d_2, and d_3 can get the state ON (1) or OFF (0) to drive the upper (S_1, S_3, and S_5) and the lower transistors (S_2, S_4, and S_6) showed in Figure 3.1. The states of the lower transistors are the complement of the upper transistors. The switching states of the corresponding vectors to generate the phase-voltages of the three-phase system are obtained from Eq. (3-12). The states of the corresponding transistors are shown in Table 3.1. As it was stated, in this work is used the SVPWM algorithm, which switching patterns are well known and can be found in any related reference as in [5]. The line-voltage waveform of the inverter applying the PWM technique is shown in Figure 3.3.
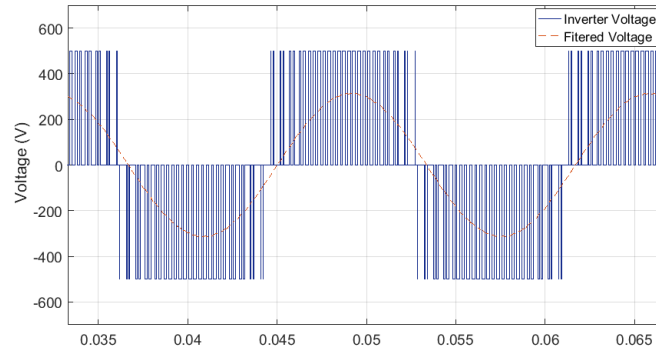
Figure 3.3 Inverter voltage applying the PWM technique

Table 3.1 Switching states and voltage values

Vector	Transistor			Phase-Voltage			Line-Voltage		
	S_1	S_3	S_5	V_{an}	V_{bn}	V_{cn}	V_{ab}	V_{bc}	V_{ca}
V_1	1	0	0	$\frac{2}{3}V_{pv}$	$-\frac{1}{3}V_{pv}$	$-\frac{1}{3}V_{pv}$	V_{pv}	0	$-V_{pv}$
V_2	1	1	0	$\frac{1}{3}V_{pv}$	$\frac{1}{3}V_{pv}$	$-\frac{2}{3}V_{pv}$	0	V_{pv}	$-V_{pv}$
V_3	0	1	0	$-\frac{1}{3}V_{pv}$	$\frac{2}{3}V_{pv}$	$-\frac{1}{3}V_{pv}$	$-V_{pv}$	V_{pv}	0
V_4	0	1	1	$-\frac{2}{3}V_{pv}$	$\frac{1}{3}V_{pv}$	$\frac{1}{3}V_{pv}$	$-V_{pv}$	0	V_{pv}
V_5	0	0	1	$-\frac{1}{3}V_{pv}$	$-\frac{1}{3}V_{pv}$	$\frac{2}{3}V_{pv}$	0	$-V_{pv}$	V_{pv}
V_6	1	0	1	$\frac{1}{3}V_{pv}$	$-\frac{2}{3}V_{pv}$	$\frac{1}{3}V_{pv}$	V_{pv}	$-V_{pv}$	0
V_7	0	0	0	0	0	0	0	0	0
V_8	1	1	1	0	0	0	0	0	0

3.2 Synchronous Reference Frame Control for Three-Phase Systems

Synchronous reference frame control, known as *dq* control, utilizes the reference frame transformation matrix named Park's transformation to transform the grid currents and voltages into a synchronous reference frame that rotates at the angular frequency *ω* of the grid [40].

Change of variables from the *abc* frame to *qd0* frame is used in electric machine analysis because it eliminates the time-varying inductances in the voltage equations [57]. However, Park's transformation has been used widely in grid-connected inverter because the control variables become DC values, thus facilitating the design of the controller [40].

The change of variable from three-phase *abc* frame to *qd0* synchronous frame rotating at the angular frequency *ω* of the grid is represented as a trigonometric relationship between the phase-voltages (or currents) projected to the *qd*-axis as can be seen in Figure 3.4 [57].
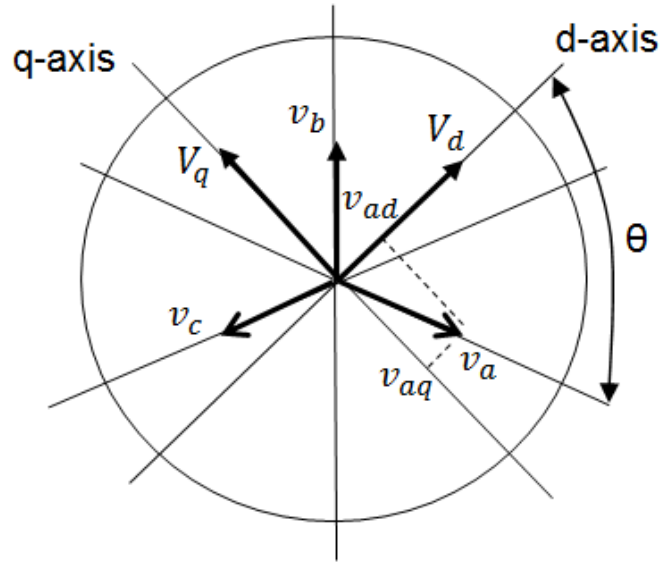
Figure 3.4 dq0 transformation diagram

The angular frequency *ω* and the angular displacement θ are related by Eq. (3-13)

$$\theta = \int_{t_0}^{t} \omega(\tau)\, d\tau + \theta_0 \tag{3-13}$$

The *d*-axis component V_d and *q*-axis component V_q are given by Eq. (3-14) and Eq. (3-15) respectively

$$V_d = \left(v_a cos\theta + v_b cos\left(\theta - \frac{2\pi}{3}\right) + v_c cos\left(\theta + \frac{2\pi}{3}\right) \right) \tag{3-14}$$

$$V_q = \left(v_a sin\theta + v_b sin\left(\theta - \frac{2\pi}{3}\right) + v_c sin\left(\theta + \frac{2\pi}{3}\right) \right). \tag{3-15}$$

The representation of Eq. (3-14) and Eq. (3-15) in matrix form is as follows:

$$\begin{bmatrix} V_d \\ V_q \\ V_0 \end{bmatrix} = \frac{2}{3} \begin{bmatrix} \cos\theta & \cos\left(\theta - \frac{2\pi}{3}\right) & \cos\left(\theta + \frac{2\pi}{3}\right) \\ \sin\theta & \sin\left(\theta - \frac{2\pi}{3}\right) & \sin\left(\theta + \frac{2\pi}{3}\right) \\ \frac{1}{2} & \frac{1}{2} & \frac{1}{2} \end{bmatrix} \begin{bmatrix} v_a \\ v_b \\ v_c \end{bmatrix}. \tag{3-16}$$

Then, the Park's transformation matrix $K_s \in \mathbb{R}^{3x3}$ to transform the *abc* frame model to the synchronous $dq0$ frame rotating at the angular frequency of the grid is given by the following equation [4]:

$$K_s = \frac{2}{3} \begin{bmatrix} \cos\theta & \cos\left(\theta - \frac{2\pi}{3}\right) & \cos\left(\theta + \frac{2\pi}{3}\right) \\ \sin\theta & \sin\left(\theta - \frac{2\pi}{3}\right) & \sin\left(\theta + \frac{2\pi}{3}\right) \\ \frac{1}{2} & \frac{1}{2} & \frac{1}{2} \end{bmatrix}. \tag{3-17}$$

The inverse matrix K_s^{-1} is given by Eq. (3-18)

$$K_s^{-1} = \begin{bmatrix} \cos\theta & \sin\theta & 1 \\ \cos\left(\theta - \frac{2\pi}{3}\right) & \sin\left(\theta - \frac{2\pi}{3}\right) & 1 \\ \cos\left(\theta + \frac{2\pi}{3}\right) & \sin\left(\theta + \frac{2\pi}{3}\right) & 1 \end{bmatrix}. \tag{3-18}$$

Thus, the general relationships to transform the *abc* frame to *dq0* frame and vice versa are:

$$\begin{bmatrix} F_d \\ F_q \\ F_0 \end{bmatrix} = K_s \begin{bmatrix} f_a \\ f_b \\ f_c \end{bmatrix} \tag{3-19}$$

$$\begin{bmatrix} f_a \\ f_b \\ f_c \end{bmatrix} = K_s^{-1} \begin{bmatrix} F_d \\ F_q \\ F_0 \end{bmatrix} \tag{3-20}$$

$[F_{dq0}]$ and $[f_{abc}]$ stand for voltage or current in *dq* frame and *abc* frame respectively.

The model in *abc* frame, represented by equations (3-8) - (3-11), is time-variant and nonlinear [4]. Then, as it was stated above, the $dq0$ frame has been adopted in this work because the control variables become DC values, therefore, facilitating the nonlinear

control design. The *abc* model is transformed to the synchronous $dq0$ frame utilizing the Park's transformation matrix given by (3-17). Then, writing equations (3-8) - (3-11) in matrix form, the following expressions are obtained:

$$\frac{d}{dt}\begin{bmatrix} i_a \\ i_b \\ i_c \end{bmatrix} = -\frac{R}{L}\begin{bmatrix} i_a \\ i_b \\ i_c \end{bmatrix} + \frac{V_{pv}}{3L}\begin{bmatrix} 2 & -1 & -1 \\ -1 & 2 & -1 \\ -1 & -1 & 2 \end{bmatrix}\begin{bmatrix} d_1 \\ d_2 \\ d_3 \end{bmatrix} - \frac{1}{L}\begin{bmatrix} v_{ga} \\ v_{gb} \\ v_{gc} \end{bmatrix} \qquad (3\text{-}21)$$

$$C\frac{dV_{pv}}{dt} = I_{pv} - \begin{bmatrix} d_1 & d_2 & d_3 \end{bmatrix}\begin{bmatrix} i_a \\ i_b \\ i_c \end{bmatrix}. \qquad (3\text{-}22)$$

From Eq. (3-19), the equation of the current in *dq0* frame is as follows:

$$\begin{bmatrix} I_d \\ I_q \\ I_0 \end{bmatrix} = K_s\begin{bmatrix} i_a \\ i_b \\ i_c \end{bmatrix}. \qquad (3\text{-}23)$$

From Eq. (3-20), the transformation of the current from *dq0* frame to *abc* frame is as follows:

$$\begin{bmatrix} i_a \\ i_b \\ i_c \end{bmatrix} = K_s^{-1}\begin{bmatrix} I_d \\ I_q \\ I_0 \end{bmatrix}. \qquad (3\text{-}24)$$

Taking the time derivative of Eq. (3-23) and then, substituting Eq. (3-24), the following equation is obtained:

$$\frac{d}{dt}\begin{bmatrix} I_d \\ I_q \\ I_0 \end{bmatrix} = \left(\frac{d}{dt}K_s\right)K_s^{-1}\begin{bmatrix} I_d \\ I_q \\ I_0 \end{bmatrix} + K_s\frac{d}{dt}\begin{bmatrix} i_a \\ i_b \\ i_c \end{bmatrix}. \qquad (3\text{-}25)$$

Multiplying Eq. (3-21) by the matrix $K_s \in \mathbb{R}^{3 \times 3}$, Eq. (3-26) is obtained.

$$K_s\frac{d}{dt}\begin{bmatrix} i_a \\ i_b \\ i_c \end{bmatrix} = -\frac{R}{L}K_s\begin{bmatrix} i_a \\ i_b \\ i_c \end{bmatrix} + \frac{V_{pv}}{3L}K_s\begin{bmatrix} 2 & -1 & -1 \\ -1 & 2 & -1 \\ -1 & -1 & 2 \end{bmatrix}\begin{bmatrix} d_1 \\ d_2 \\ d_3 \end{bmatrix}$$
$$-\frac{1}{L}K_s\begin{bmatrix} v_{ga} \\ v_{gb} \\ v_{gc} \end{bmatrix} \qquad (3\text{-}26)$$

27

Substituting Eq. (3-26) and the time derivative of Eq. (3-17) into Eq. (3-25), after some mathematical work, the following equation is obtained:

$$\frac{d}{dt}\begin{bmatrix} I_d \\ I_q \\ I_0 \end{bmatrix} = \begin{bmatrix} -\frac{R}{L} & \omega & 0 \\ -\omega & -\frac{R}{L} & 0 \\ 0 & 0 & 0 \end{bmatrix}\begin{bmatrix} I_d \\ I_q \\ I_0 \end{bmatrix} + \frac{V_{pv}}{L}\begin{bmatrix} 1 & 0 & 0 \\ 0 & 1 & 0 \\ 0 & 0 & 0 \end{bmatrix}\begin{bmatrix} d_d \\ d_q \\ d_0 \end{bmatrix} - \frac{1}{L}\begin{bmatrix} 1 & 0 & 0 \\ 0 & 1 & 0 \\ 0 & 0 & 0 \end{bmatrix}\begin{bmatrix} V_{gd} \\ V_{gq} \\ V_{g0} \end{bmatrix}. \qquad (3\text{-}27)$$

The voltage dynamics of the DC link capacitor is given by Eq. (3-22), then, the $dq0$ transformation of it is as follows:

$$C\frac{dV_{pv}}{dt} = I_{pv} - \left[K_s^{-1}\begin{bmatrix} d_d \\ d_q \\ 0 \end{bmatrix} \right]^T K_s^{-1}\begin{bmatrix} I_d \\ I_q \\ 0 \end{bmatrix}. \qquad (3\text{-}28)$$

Substituting Eq. (3-18) into Eq. (3-28), after some mathematical work, the expression that represents the dynamics of the DC link capacitor in $dq0$ frame is:

$$C\frac{dV_{pv}}{dt} = I_{pv} - d_d I_d - d_q I_q. \qquad (3\text{-}29)$$

From Eq. (3-27) and Eq. (3-29), the dynamic equations of the PV system model in $dq0$ frame in dot notation are as follows:

$$\dot{I}_d = -\frac{R}{L}I_d + \omega I_q + \frac{d_d}{L}V_{pv} - \frac{1}{L}V_{gd} \qquad (3\text{-}30)$$

$$\dot{I}_q = -\frac{R}{L}I_q - \omega I_d + \frac{d_q}{L}V_{pv} - \frac{1}{L}V_{gq} \qquad (3\text{-}31)$$

$$\dot{V}_{pv} = -\frac{d_d}{C}I_d - \frac{d_q}{C}I_q + \frac{1}{C}I_{pv}. \qquad (3\text{-}32)$$

where, I_d and I_q are the d-axis and q-axis current components of the three-phase output current of the inverter, V_{gd} and V_{gq} are the d-axis and q-axis voltage components of the phase-voltage of the grid, V_{pv} and I_{pv} are the voltage and current of the PV array

28

respectively, ω is the angular frequency of the grid, and d_d and d_q are the control functions of the inverter in *qd0* frame. From Eq. (3-30) and Eq. (3-31), a cross-coupling dependence of I_d and I_q currents are apparent. To decouple the active and reactive power loops and facilitate the model analysis [40], the auxiliary control functions d'_d and d'_q are defined as follows [7]:

$$d'_d = d_d + \frac{\omega L}{V_{pv}} I_q \tag{3-33}$$

$$d'_q = d_q - \frac{\omega L}{V_{pv}} I_d. \tag{3-34}$$

Replacing the switching functions d_d and d_q of Eq. (3-33) and Eq. (3-34) respectively into equations (3-30), (3-31), and (3-32), the new dynamic system equations to design the nonlinear controller are obtained.

$$L\dot{I}_d = -RI_d + d'_d V_{pv} - V_{gd} \tag{3-35}$$

$$L\dot{I}_q = -RI_q + d'_q V_{pv} - V_{gq} \tag{3-36}$$

$$C\dot{V}_{pv} = -d'_d I_d - d'_q I_q + I_{pv}. \tag{3-37}$$

CHAPTER IV

CONTROL SYSTEM DEVELOPMENT OF THE THREE-PHASE
PHOTOVOLTAIC SYSTEM

PV systems are by nature nonlinear due to the nonlinear characteristics of the PV array and the voltage dynamics of the DC link capacitor, which includes nonlinearities due to the switching functions of the inverter. Since the nonlinear effects could be significant in the dynamics of the PV system, in this work, it is proposed a nonlinear controller based on Lyapunov analysis to control a three-phase PV system in a single-stage topology.

In this dissertation, a novel trajectory of the *d*-axis reference current taking into account the voltage dynamics of the DC link capacitor is determined. The nonlinear controller is designed to track the MPP operation of the PV array and to control the active and reactive power to obtain unity power factor on the grid side. Thus, it is not necessary the use of a DC-DC converter as is required in other works based on nonlinear control as in [24] and [33]. The block diagram of the proposed controller is shown in Figure 4.1.

4.1   Control Design

The proposed controller should ensure that the *d*-axis inverter output current $I_d(t)$ tracks the *d*-axis reference current $I_{dref}(t)$, which novel trajectory is obtained online from the voltage dynamics of the DC link capacitor, and that the *q*-axis current I_q tracks the *q*-axis reference current I_{qref} obtained from the load requirement.
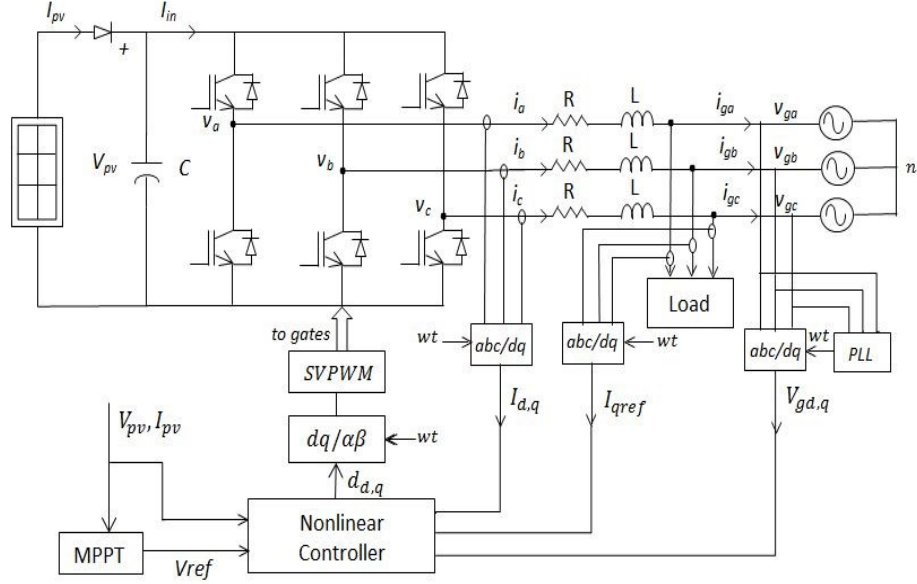
Figure 4.1 Single-stage three-phase PV system with nonlinear controller

Therefore, the objective of the control scheme is to design the control signals $d_d(t)$ and $d_q(t)$ such that $I_d(t) \to I_{dref}(t)$ and $I_q(t) \to I_{qref}(t)$ as t $\to \infty$, thus controlling the active and the reactive power of the system to keep the unity power factor on the grid side. Moreover, the PV system must operate at the maximum power point while maintaining the other objectives. To achieve MPP operation, the control law must also ensure that $V_{pv}(t) \to V_{ref}(t)$ as $t \to \infty$, where $V_{ref}(t)$ is the reference voltage obtained from the INC algorithm.

To facilitate the control development, the following assumptions are considered:

Assumption 1. $R, L, C \in \mathbb{R}^+$ are known constant parameters of the system.

Assumption 2. The q-axis reference current $I_{qref}(t)$ is a known constant value; it is measurable and sufficiently differentiable. Thus, $I_{qref}(t)$ and $\dot{I}_{qref}(t)$ are bounded.

31

Assumption 3. The voltage of the grid is sinusoidal and symmetrical. Therefore, the *d*-axis grid voltage is a known value, and *q*-axis grid voltage is zero.

Assumption 4. The reference voltage V_{ref} is measurable and sufficiently differentiable. Thus, $V_{ref}(t)$ and $\dot{V}_{ref}(t)$ are bounded.

Assumption 5. $I_{pv}(t)$ is bounded on the condition that of the voltage $V_{pv}(t)$ is bounded.

To meet all the control objectives, the errors signals $e_d(t), e_q(t), e_v(t) \in \mathbb{R}$, are defined as follows:

$$e_d \triangleq I_d - I_{dref} \tag{4-1}$$

$$e_q \triangleq I_q - I_{qref} \tag{4-2}$$

$$e_v \triangleq V_{pv} - V_{ref}. \tag{4-3}$$

These signals will facilitate the subsequent analysis. Multiplying equations (4-1) and (4-2) by the inductance *L*, and Eq. (4-3) by the capacitance *C*, and then, taking the time derivative of those equations, the following equations are obtained:

$$L\dot{e}_d = L\dot{I}_d - L\dot{I}_{dref} \tag{4-4}$$

$$L\dot{e}_q = L\dot{I}_q - L\dot{I}_{qref} \tag{4-5}$$

$$C\dot{e}_v = C\dot{V}_{pv} - C\dot{V}_{ref}. \tag{4-6}$$

Substituting equations (3-35), (3-36), and (3-37) into equations (4-4), (4-5), and (4-6) respectively, the open-loop error system is developed as follows:

$$L\dot{e}_d = -RI_d + d_d'V_{pv} - LV_{gd} - L\dot{I}_{dref} \tag{4-7}$$

32

$$L\dot{e}_q = -RI_q + d'_q V_{pv} - L\dot{I}_{qref} \tag{4-8}$$

$$C\,\dot{e}_v = -d'_d I_d - d'_q I_q + I_{pv} - C\dot{V}_{ref}. \tag{4-9}$$

To guarantee that the error signals $e_d(t)$ and $e_q(t) \to 0$ as $t \to \infty$, the current closed loop error signals are chosen as:

$$L\dot{e}_d = -K_1 e_d \tag{4-10}$$

$$L\,\dot{e}_q = -K_2 e_q \tag{4-11}$$

where K_1, K_2 are positive constant control gains.

Then, from Eq. (4-7) and Eq. (4-8) along with Eq. (4-10) and Eq. (4-11), the control functions d'_d and d'_q are designed as follows:

$$d'_d = \frac{1}{V_{pv}}\left(-K_1 e_d + RI_d + V_{gd} + L\dot{I}_{dref}\right) \tag{4-12}$$

$$d'_q = \frac{1}{V_{pv}}\left(-K_2 e_q + RI_q + L\dot{I}_{qref}\right). \tag{4-13}$$

4.2   Design of the *d*-Axis Reference Current Trajectory

For three-phase grid-connected PV systems based on nonlinear control, some works obtain the reference current through a DC-DC converter as in [24] and [33], thus using the two-stage scheme. For a single-stage scheme, the reference current is directly obtained from the MPPT algorithm without taking into account the voltage dynamics of the DC link capacitor as in [39]. The voltage dynamics of the DC link capacitor and the switching functions of the inverter could affect the dynamics of the PV system under sudden changes of the atmospheric conditions or any perturbation as a quick change of

the load. Failing to consider the voltage dynamics of the DC link capacitor and the switching functions of the inverter could lead to oscillation of the DC link voltage or injection of non-sinusoidal current into the grid, therefore affecting the efficiency and the power quality.

In this work, the design of the d-axis reference current trajectory is developed using the dynamics of the DC link capacitor given by Eq. (3-37). It can be seen that the control signal, given by Eq. (4-12), depends on the time derivative of the d-axis reference current. Then, substituting Eq. (4-12) and Eq. (4-13) into Eq. (4-9), equation (4-14) is obtained.

$$
C\dot{e}_v = -\frac{I_d}{V_{pv}}\left(-K_1 e_d + RI_d + V_{gd} + L\dot{I}_{dref}\right) - \frac{I_q}{V_{pv}}\left(-K_2 e_q + RI_q + L\dot{I}_{qref}\right)
$$
$$
+ I_{pv} - C\dot{V}_{ref}
$$

(4-14)

To guarantee that the error signal $e_v \to 0$ as $t \to \infty$ the voltage closed loop error signal is chosen as:

$$
C\,\dot{e}_v = -K_3 e_v
$$

(4-15)

where K_3 is a positive constant control gain. Substituting the closed-loop error signal given by Eq. (4-15) into Eq. (4-14), after some mathematical work, the differential equation $\dot{I}_{dref}$ to obtain the trajectory of I_{dref} is designed as:

$$
\dot{I}_{dref} = \frac{K_2}{L} e_q \frac{I_q}{I_d} + \frac{K_3}{L} e_v \frac{V_{pv}}{I_d} + \frac{1}{L}\frac{V_{pv}I_{pv}}{I_d} - \frac{C}{L}\frac{V_{pv}}{I_d}\dot{V}_{ref} - \frac{I_q}{I_d}\dot{I}_{qref} - \frac{R}{L}\frac{I_q^2}{I_d} +
$$
$$
\frac{K_1}{L} e_d - \frac{R}{L} I_d - \frac{1}{L} V_{gd}.
$$

(4-16)

34

4.3　Stability Analysis

A common and general approach for studying the stability of nonlinear control systems is the Lyapunov stability theory. Useful properties and the mathematical analysis in the related field can be found in reference books as in [51]-[53]. In this dissertation, it will be shown that the origin holds exponential stability, which is the strongest form of stability [52]. It is important to emphasize that exponential stability implies asymptotic stability. However, asymptotic stability does not guarantee exponential stability [51].

To prove the stability of the proposed controller, the following theorem is stated:

Theorem 1: Using the closed loop error system given by equations (4-10), (4-11), and (4-15), the error signals defined by equations (4-1), (4-2), and (4-3) are exponentially regulated as follows:

$$e_d(t), e_q(t), e_v(t) \rightarrow 0 \ as \ t \rightarrow \infty \tag{4-17}$$

According to *Definition 3.5* of [51], it will be shown that:

$$\|x(t)\| \leq \|x_0\| \left(\frac{\lambda_{Zmax}}{\lambda_{Zmin}}\right)^{1/2} exp^{-\gamma t} \tag{4-18}$$

where $x(t) = [e_d(t) \quad e_q(t) \quad e_v(t)]^T$, $\|x\| = \left(e_d^2 + e_q^2 + e_v^2\right)^{1/2}$, $\gamma = \frac{\lambda_{Kmin}}{\lambda_{Zmax}}$ known as rate of exponential convergence [51].

λ_{Zmax} and λ_{Zmin} are the maximum and minimum eigenvalues of matrix Z .

$$Z = \begin{bmatrix} L & 0 & 0 \\ 0 & L & 0 \\ 0 & 0 & C \end{bmatrix}$$

λ_{Kmax} and λ_{Kmin} are the maximum and minimum eigenvalues of matrix K

$$K = \begin{bmatrix} K_1 & 0 & 0 \\ 0 & K_2 & 0 \\ 0 & 0 & K_3 \end{bmatrix}$$

Proof: Choosing a positive definite Lyapunov function candidate as:

$$V_1(x) = \frac{1}{2}Le_d^2 + \frac{1}{2}Le_q^2 + \frac{1}{2}Ce_v^2 \tag{4-19}$$

$V_1(x)$ can be written in matrix form as:

$$V_1(x) = \frac{1}{2}\begin{bmatrix} e_d & e_q & e_v \end{bmatrix}\begin{bmatrix} L & 0 & 0 \\ 0 & L & 0 \\ 0 & 0 & C \end{bmatrix}\begin{bmatrix} e_d \\ e_q \\ e_v \end{bmatrix} = \frac{1}{2}x^T Z x \tag{4-20}$$

From *Definition 2.11* of [52], the symmetric matrix Z is positive definite; therefore the eigenvalues of the matrix Z are real and positive. The eigenvalues of the matrix Z are: $\lambda_1 = L$, $\lambda_2 = L$, $\lambda_3 = C$. The values of L and C utilized in this design are: $C = \lambda_{Zmax} = 0.0022$ and $L = \lambda_{Zmin} = 0.002$.

Utilizing Theorem 2.5 (*Rayleigh Theorem*) stated in [52], for any $x \epsilon \mathbb{R}^n$, the following inequality is true for $V_1(x)$.

$$\frac{1}{2}\lambda_{Zmin}\|x\|^2 \leq V_1(x) \leq \frac{1}{2}\lambda_{Zmax}\|x\|^2 \tag{4-21}$$

Taking the time derivative of Eq. (4-19) the following equation is obtained:

$$\dot{V}_1 = Le_d\dot{e}_d + Le_q\dot{e}_q + Ce_v\dot{e}_v. \tag{4-22}$$

To guarantee that the error signals $e_d, e_q,$ and $e_v \to 0$ as $t \to \infty$ the closed loop error signals were defined by (4-10), (4-11), and (4-15). Then, substituting these equations into (4-22), the equation (4-23) is obtained:

36

$$\dot{V}_1 = -K_1 e_d^2 - K_2 e_q^2 - K_3 e_v^2 \tag{4-23}$$

Since the control gains $K_1, K_2, K_3 \in \mathbb{R}^+$, it is clear that $\dot{V}_1$ is negative definite function.

Writing Eq. (4-23) in matrix form, it is expressed as follows:

$$\dot{V}_1 = -[e_d \quad e_q \quad e_v]K \begin{bmatrix} e_d \\ e_q \\ e_v \end{bmatrix} = -x^T K x \tag{4-24}$$

Then, applying the *Rayleigh Theorem* to the matrix K of Eq. (4-24), $\dot{V}_1$ can be upper bounded as follows:

$$\dot{V}_1 \leq -\lambda_{Kmin} \|x\|^2 \tag{4-25}$$

From (4-21), the square norm is:

$$\|x\|^2 \geq \frac{2V_1}{\lambda_{Zmax}} \tag{4-26}$$

Then, substituting Eq. (4-26) into Eq. (4-25), $\dot{V}_1$ is upper bounded as follows:

$$\dot{V}_1 \leq -\lambda_{Kmin} \frac{2V_1}{\lambda_{Zmax}} \tag{4-27}$$

Hence, Eq. (4-27) can be written as:

$$\dot{V}_1 \leq -2\gamma V_1 \tag{4-28}$$

Solving the differential equation given by Eq. (4-28), the Eq. (4-29) is obtained:

$$V_1(x) \leq V_1(x_0)exp^{-2\gamma t} \tag{4-29}$$

Taking the left-hand side term of (4-21), $\|x\|$ can be written as follows:

$$\|x\| \leq \left(\frac{2V_1}{\lambda_{Zmin}}\right)^{1/2} \tag{4-30}$$

Substituting (4-29) into (4-30), the following equation is obtained:

$$\|x\| \leq \left(\frac{2V_1(x_0)exp^{-2\gamma t}}{\lambda_{Zmin}}\right)^{1/2} \tag{4-31}$$

Applying for x_0 the right-hand side of the inequality given by (4-21), the Eq. (4-32) is obtained:

$$V_1(x_0) \leq \frac{1}{2}\lambda_{Zmax}\|x_0\|^2 \tag{4-32}$$

Substituting (4-32) into (4-31) the following inequality is obtained:

$$\|x(t)\| \leq \|x_0\|\left(\frac{\lambda_{Zmax}}{\lambda_{Zmin}}\right)^{1/2} exp^{-\gamma t} \tag{4-33}$$

where $\lambda_{Zmax} = 0.0022$, $\lambda_{Zmin} = 0.002$. The values of the matrix K obtained for this design are: $K_1 = 296$, $K_2 = 494$, $K_3 = 44$. Then, $\lambda_{Kmax} = 494$, $\lambda_{Kmin} = 44$, and $\gamma = \frac{\lambda_{Kmin}}{\lambda_{Zmax}} = 20000$. Thus, given by Eq. (4-33) the origin $\left(e_d(t), e_q(t), e_v(t)\right) = (0,0,0)$ is exponential stable.

From Eq. (4-19) and (4-23), it is clear that $e_d(t)$, $e_q(t)$, and $e_v(t)$ are square integrable and bounded. To show that all the signals of the closed loop system are bounded the assumptions given in section 4.1 are considered. From Assumption 4, V_{ref} is bounded, then from Eq. (4-3) it is shown that V_{pv} is bounded. Thus, from Assumption 5 I_{pv} is bounded. From Assumption 3 and knowing that V_{pv} and I_{pv} are shown to be bounded, from the fact that in steady state the PV power is equal to the grid power according to the power balance relationship, then I_d is bounded. Therefore, from Eq. (4-1) along with the above boundedness statements, I_{dref} is bounded. From Assumption 2 and knowing that $e_q(t)$ is bounded, Eq. (4-2) is used to show that the current I_q is bounded. From Assumption 2 $\dot{I}_{qref}$ is bounded. From Assumption 2, Assumption 3, and Assumption 4 along with the above boundedness statements, Eq. (4-16) is utilized to show that $\dot{I}_{dref}$ is bounded. Using the above boundedness statements, from Eq. (4-12) and Eq. (4-13) it can

be demonstrated that d'_d and d'_q are bounded. Similarly, based on the above boundedness statements, from equations (3-35), (3-36), and (3-37) it is shown that $\dot{I}_d$, $\dot{I}_q$, and $\dot{V}_{pv}$ are bounded. Finally, from Assumption 4 along with the above boundedness statements, equations (4-7), (4-8), and (4-9) are utilized to show that $\dot{e}_d$, $\dot{e}_q$, and $\dot{e}_v$ are bounded. Thus, completing the proof of the theorem.

4.4 Simulation Results of the Three-Phase PV System

The Matlab/Simulink package with Simscape Power System was used to model the circuit dynamics of the PV system and the control scheme. Then, a numerical simulation was performed to validate the control design. The parameters utilized for the PV system including the control gains are summarized in Table 4.1.

Table 4.1 System Parameters of the Three-Phase PV System

Parameter	Value	Units	Parameter	Value	Units
R	0.1	Ω	K_1	296	–
L	2	mH	K_2	494	–
C	2200	μF	K_3	44	–
f_{sw}	12	Khz	V_g	127	V(rms)
f	60	Hz	v_{step}	$5e^{-3}$	V

f_{sw} is the switching frequency and v_{step} is the voltage step of the MPPT algorithm.

The values of the control gains K_1, K_2, and K_3 were obtained by a trial-error method until it was achieved the desired error signals. For the simulation, it was utilized the Sunpreme SNPM-F60-02-185 PV module available in the SimPower library of the

Matlab/Simulink package. The parameters of the PV module are summarized in Table 4.2.

Table 4.2 Photovoltaic Module Parameters

Module Sunpreme SNPM-F60-02-185	
Maximum Power (185.22 W)	*Cells per module (60)*
Open circuit voltage Voc	36.9 V
Short circuit current Isc	7 A
Voltage MPP	29.4 V
Current MPP	6.3
Parallel string	13
Series strings	17
Vmax at 25 °C	499.8 V
Imax at 25 °C	81.9 A
Pmax at 25 °C and 1000 W/m^2	40.94 KW
Pmax at 25 °C and 800 W/m^2	33.03KW
Pmax at 25 °C and 600 W/m^2	24.91 KW

First, to evaluate the performance of the control scheme under various atmospheric conditions, a constant temperature of 25^oC was set and the irradiance was changed in steps from 0 to 600 to 800, to 1000 and finally back to 800 W/m^2 at t= 0, 0.2, 0.4, and 0.6 seconds respectively. The irradiance changes are shown in Figure 4.2. Figure 4.3 shows the steady state and dynamics response of the PV power to variations of the irradiance. The steady state power values are close to the ideal maximum values given in Table 4.2. The deviation of the mean power related to the maximum values is about 0.01 % at 600 W/m^2, 0.05% at 800 W/m^2 and 0.07% at 1000 W/m^2. These small

percentages of power deviation validate the use of the incremental conductance algorithm to get the reference voltage and therefore the maximum power.
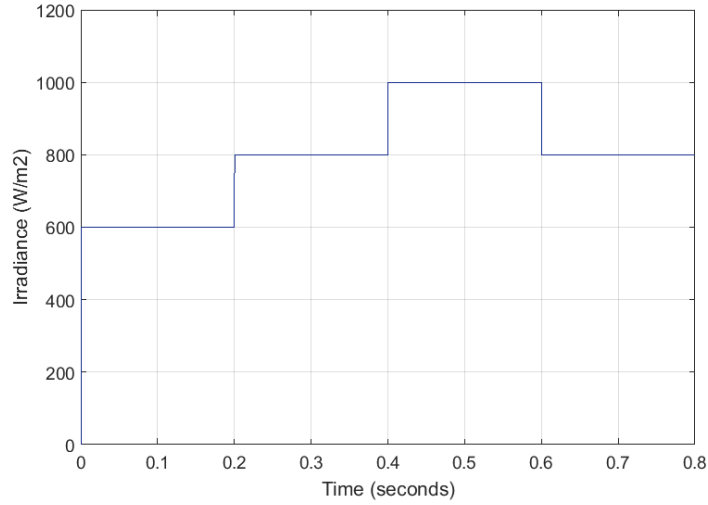
Figure 4.2 Irradiance for various atmospheric conditions
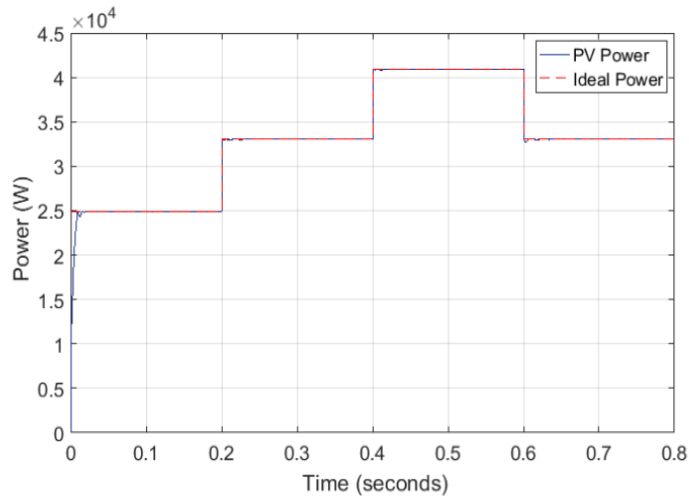
Figure 4.3 PV array power and ideal maximum power

The tracking errors signals $e_d(t)$, $e_q(t)$, and $e_v(t)$ are shown in Figures 4.4 a), b) and c) respectively. These figures show that the tracking errors are approximately regulated to zero, hence validating the analysis.
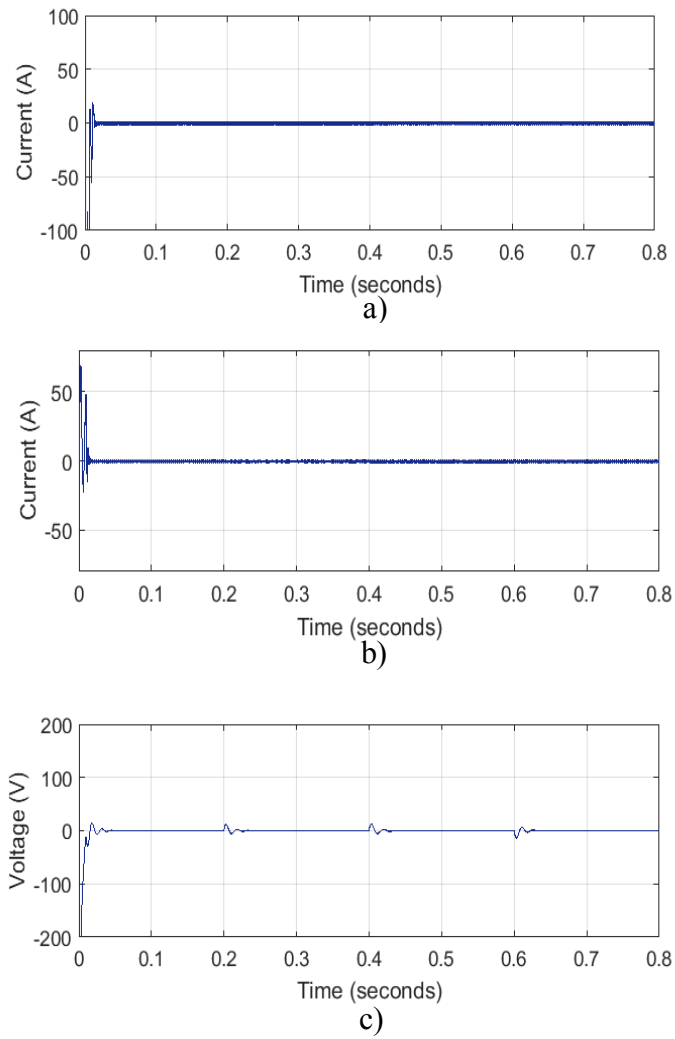
Figure 4.4 Tracking errors: a) $e_d(t)$, b) $e_q(t)$, and c) $e_v(t)$

Figure 4.5 shows the *d*-axis and *q*-axis currents both with their respective reference currents. It is clear that the current $I_d(t)$ follows the reference current $I_{dref}(t)$, which trajectory was obtained using Eq. (4-16). The current $I_q(t)$ follows the reference current $I_{qref}(t)$, which is equal to the reactive current required by the load. In this case, it was assumed that there is no load connected to the point of common coupling; therefore $I_{qref}(t)$ is zero.
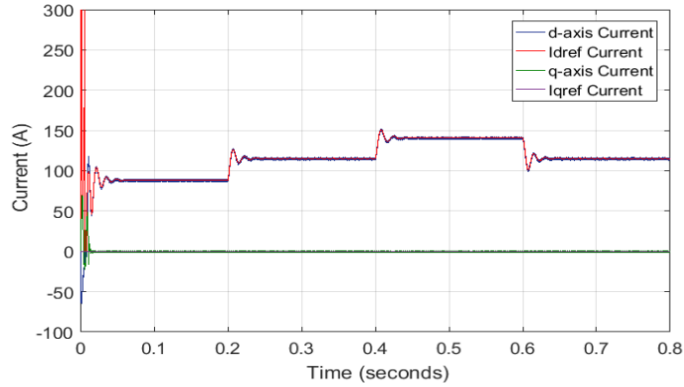
Figure 4.5 $I_d(t)$ and $I_q(t)$ currents with $I_{dref}(t)$ and $I_{qref}(t)$ reference currents

Figure 4.6 shows the reference voltage $V_{ref}(t)$, obtained from the INC algorithm, and the

voltage of the PV array $V_{pv}(t)$. It can be seen that the voltage of the PV array follows the

reference voltage and it is kept steady despite the sudden change of the irradiance.
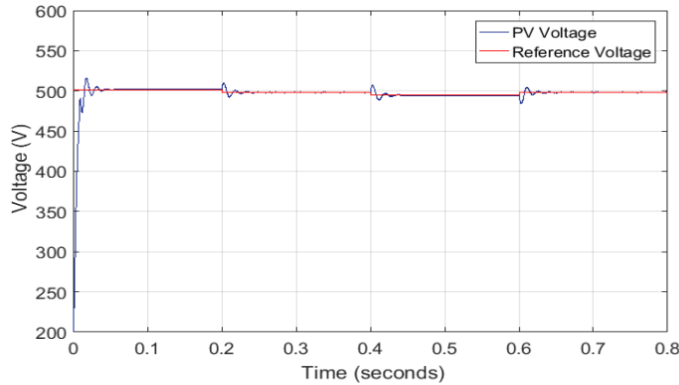
Figure 4.6 Reference voltage $V_{ref}(t)$ and PV array voltage $V_{pv}(t)$

Figure 4.7 shows the active and reactive power injected into the grid for different values

of irradiance. It can be seen that the reactive power supplied to the grid is zero, as it was

desired. Figure 4.8 shows the phase-voltage and the phase-current of the grid. Figure 4.9

shows a zoom-in version of Figure 4.8 where it can be seen that both the voltage and the

current are sinusoidal and in phase.
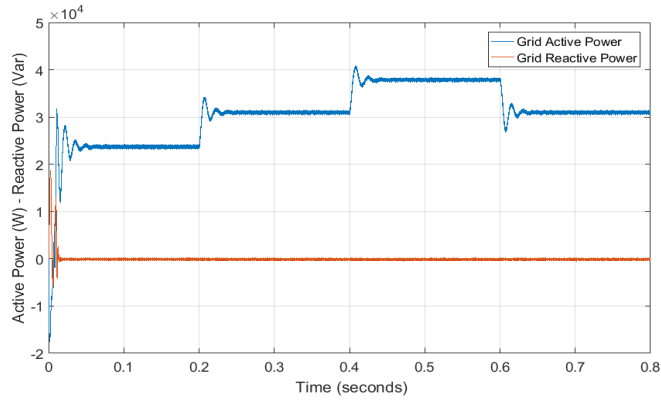
Figure 4.7 Active and reactive power injected to the grid
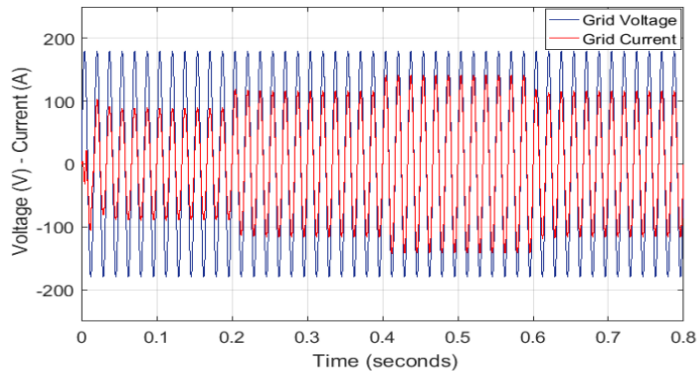
Figure 4.8 Grid phase-voltage and phase-current
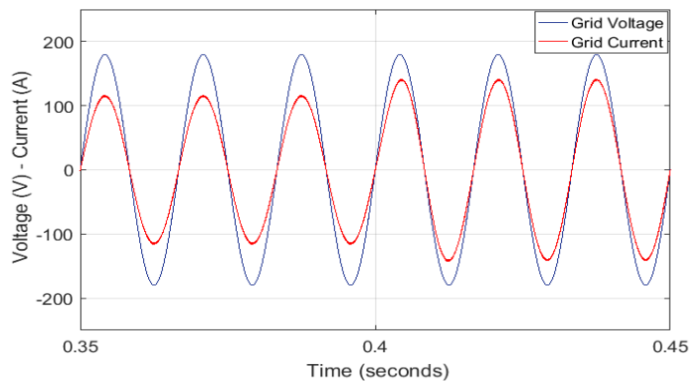
Figure 4.9 Grid voltage and current response to changes of irradiance at t= 0.4 s.

Additionally, Figure 4.9 shows the transient behavior of the grid current when the irradiance changes from 800 W/m^2 to 1000 W/m^2 at t= 0.4 seconds. The transient

44

time to get the new steady state and therefore the synchronism between the phase-voltage and current is approximately less than two cycles, thus showing the robustness of the proposed nonlinear closed loop controller. Furthermore, Figure 4.10 shows the three-phase currents of the grid, which are sinusoidal and they are in phase with the corresponding three-phase voltages. Thus, demonstrating that the power factor on the grid side is unity, as it was desired.
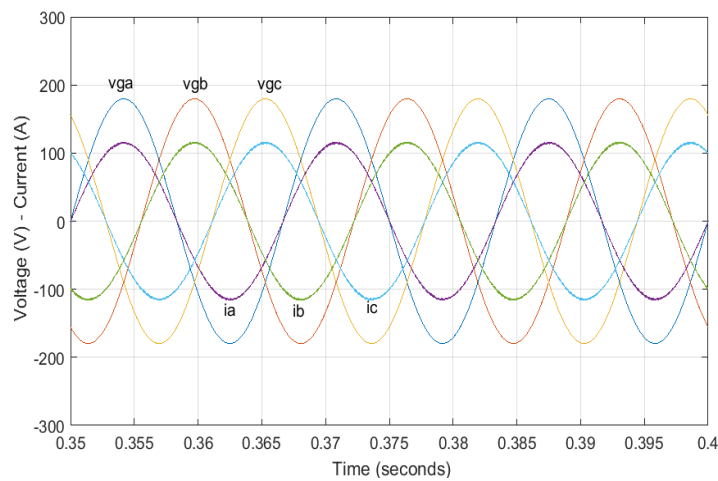
Figure 4.10 Three-phase grid voltage and current at $800\ W/m^2$

Figure 4.11 shows the harmonic components of the grid current when the irradiance is $600\ W/m^2$. It shows that the values of harmonic components of the current are less than 0.1%, with a total harmonic distortion (THD) of about 1.09 %.

Second, at irradiance of $600\ W/m^2$, an *R-L* load of 15 KW, 15 KVar was connected to the point of common coupling at t = 0.2 seconds to see the performance of the controller on compensating the reactive power and therefore to obtain unity power factor on the grid side.
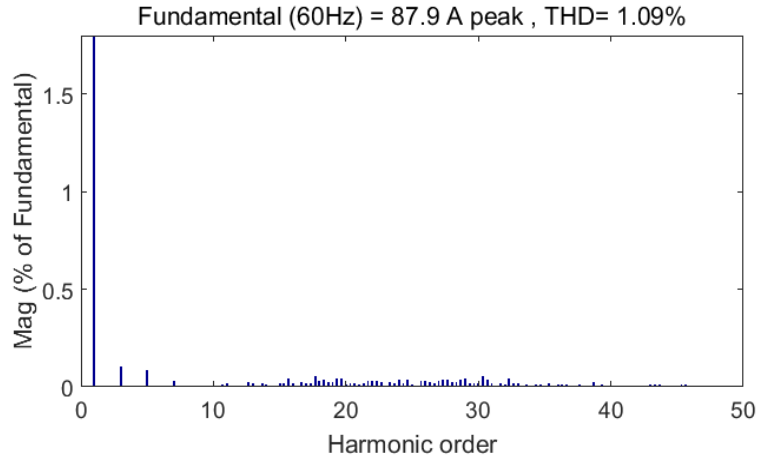
Figure 4.11 Grid current harmonic components at $600\ W/m^2$

Figures 4.12 and 4.13 show the active and reactive power of the PV system respectively. When the load is connected at t =0.2 seconds, it can be seen in Figure 4.12 that the inverter is supplying the active power required by the load and the remaining of active power is supplied to the grid. Figure 4.13 shows that the reactive power; required by the load, is supplied by the inverter. Thus, the reactive power on the grid side is approximately zero. Figure 4.14 shows the voltage and the current of the load. It can be seen that the load current is lagging an angle of about 45 degrees after the load is connected as it was expected.
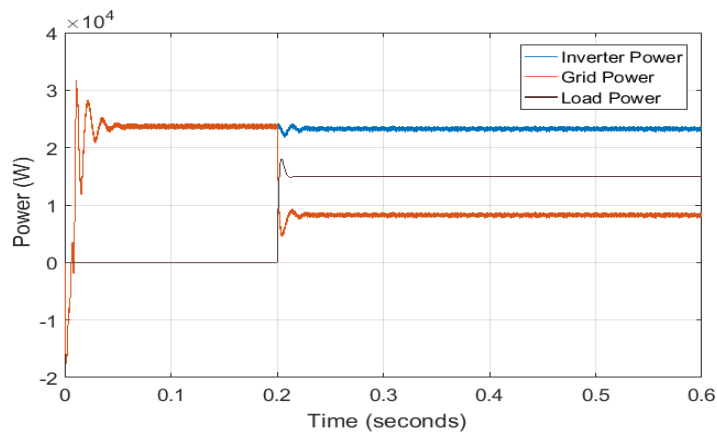
Figure 4.12 Active power of the PV system with *R-L* load
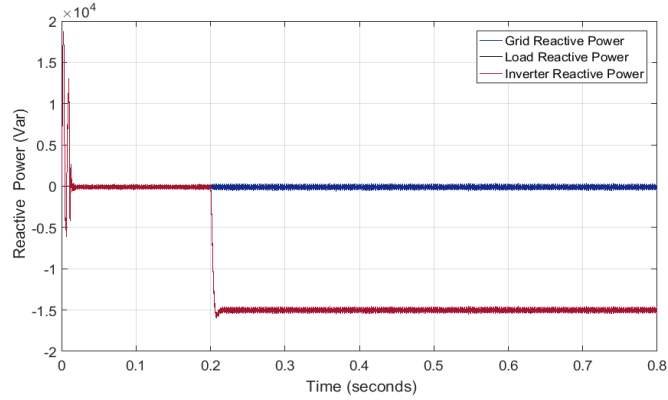
Figure 4.13 Reactive power of the PV system with *R-L* load
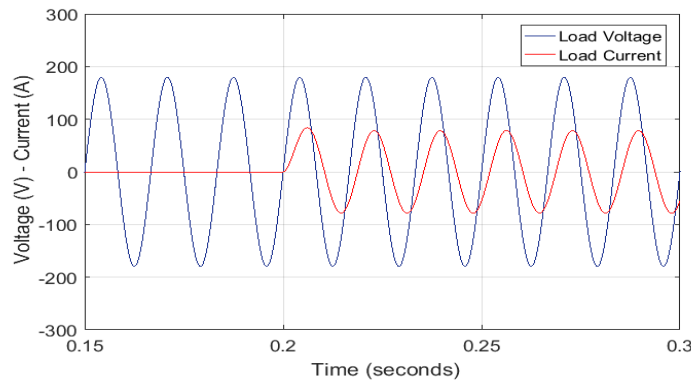
Figure 4.14 Load voltage and current

Figure 4.15 shows the grid voltage and current. It shows that the voltage and current are sinusoidal and in phase, showing that the inverter is supplying the reactive power required by the load and therefore the power factor on the grid side is the unity as it was desired. Moreover, it can be seen that the transient time is less than two cycles to reach the new steady state after the change of load, thus, showing the robustness of the proposed nonlinear controller to fast changes of the load. The total harmonic distortion of the grid current, when an *R-L* load of about 60% the maximum power at 600 W/m^2 is connected to the point of common coupling, is approximately 2.87%, as it can be seen in Fig. 4.16. The THD of the current is less than 5% , which fulfills the IEEE-519 standard.

47
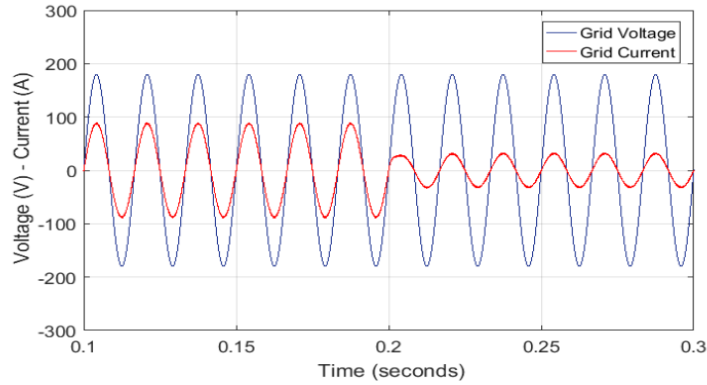
Figure 4.15 Grid voltage and current with a load connected at t=0.2 s.
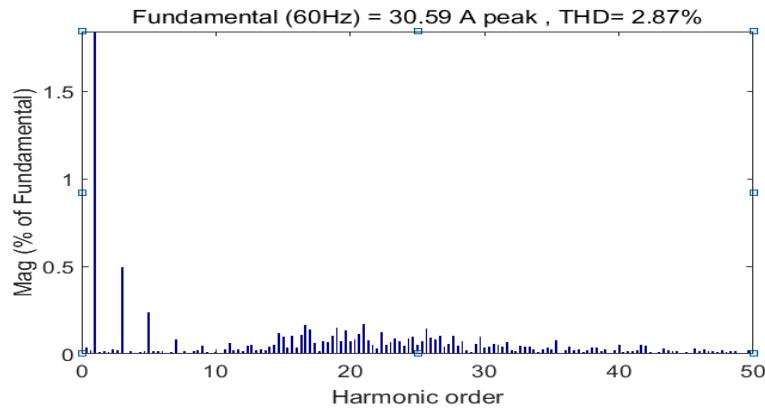
Figure 4.16 Grid current harmonic components with R-L load at 600 W/m^2

Finally, the controller reported by [39] was simulated for the same atmospheric conditions utilized in this work without load to see the performance of the proposed controller compared with an existing controller. In [39] are not considered the voltage dynamics of the DC link capacitor to obtain the reference current, and there is not control of the reactive power. From the obtained results, in Figure 4.17 can be seen that the proposed controller shows better performance related to voltage overshoot, stabilization time and steady state of the voltage generated by the PV array. As the PV voltage is the input voltage of the DC-AC converter utilized to transfer power to the grid, the quality of the voltage influences directly on the efficiency and power quality.
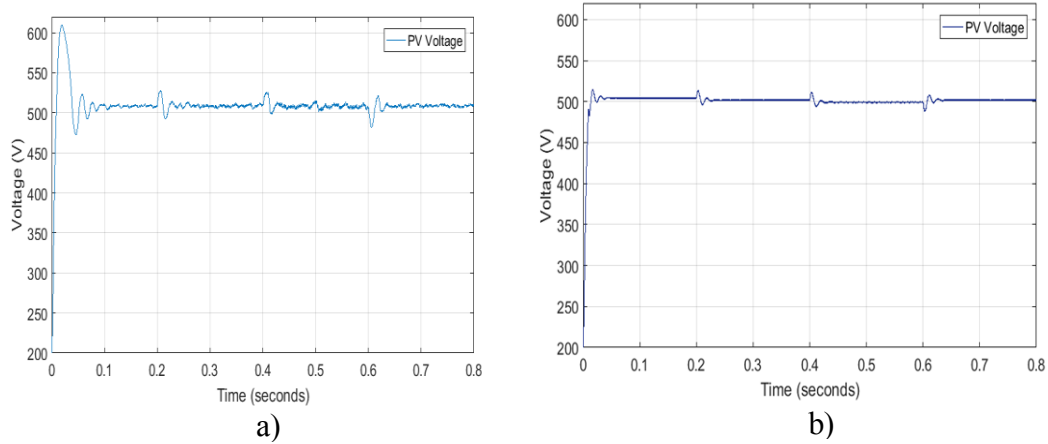
Figure 4.17 Photovoltaic voltage a) existing controller b) proposed controller

Figure 4.18 shows the power generated by the PV array. It can be seen from Figure 4.18a) that the PV power of the existing controller is more oscillatory than the proposed controller. Thus, the grid current of the existing controller is not a pure sine wave as can be seen in Figure 4.19. A zoom-in version of Figure 4.19 with a time range from 0.35 seconds to 0.45 seconds is shown in Figure 4.20. In this figure, it is clear that the grid current of the existing controller is not pure sine wave.
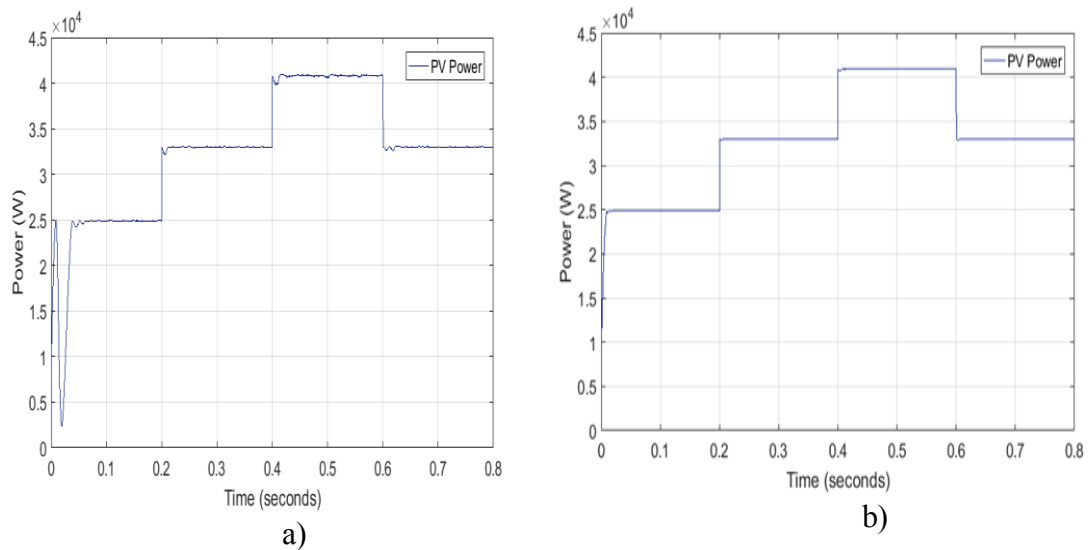
Figure 4.18 Photovoltaic power a) existing controller b) proposed controller

a)   b)
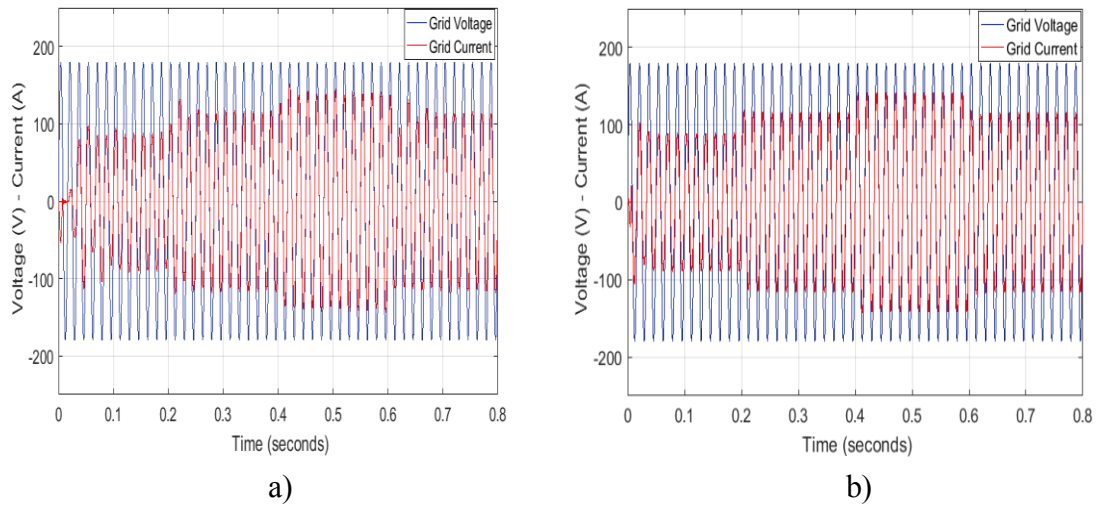
Figure 4.19 Grid voltage and current a) existing controller b) proposed controller

a)   b)
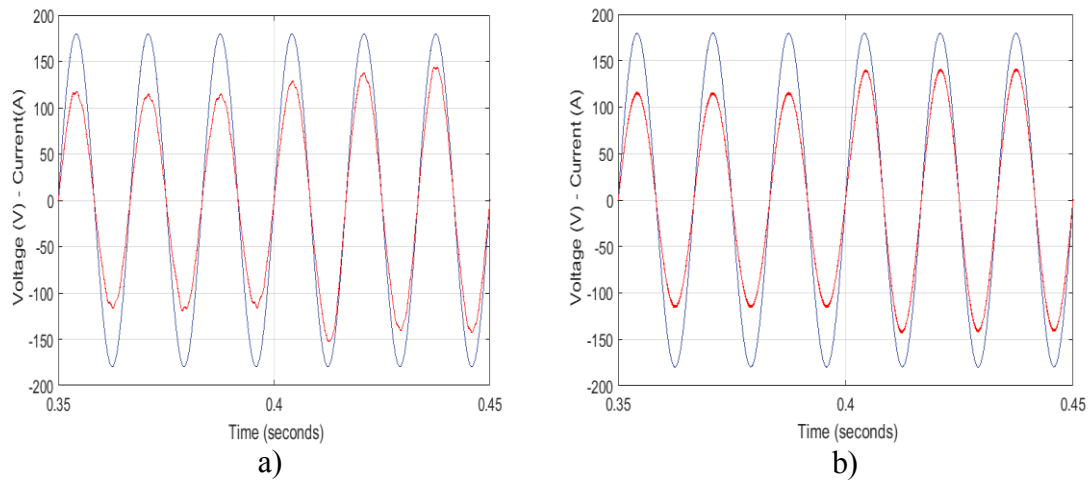
Figure 4.20 Grid voltage and current a) existing controller b) proposed controller. Time range from (0.35, 0.45 seconds)

Although the THD of the current obtained from the existing controller meets with the IEEE 519 standard, the harmonic content of the current is bigger than the harmonic content of the proposed controller. The values of the total harmonic distortion of the current for both controllers are presented in Table 4.3 for various atmospheric conditions.

Table 4.3 Total Harmonic Distortion Comparison Results

Irradiance (W/m^2)	Existing Controller [39]		Proposed Controller	
	THD (%)	Grid Current (A rms)	THD (%)	Grid Current (A rms)
1000	1.86	98.4	0.65	99.30
800	1.97	81.07	0.82	81.25
600	2.85	62.1	1.09	62.16
Filter Inductance	3mH		2mH	
Maximum overshoot	22%		2%	
Settle time	≈3 to 6 cycles		≈2cycles	

Thus, the proposed controller performs well showing better working characteristics as voltage overshoot, stabilization time and steady state of the voltage generated by the PV array. Moreover, the proposed controller showed better power quality with low total harmonic distortion of the grid current.

CHAPTER V

SINGLE-STAGE SINGLE-PHASE GRID-CONNECTED PHOTOVOLTAIC
SYSTEMS

Nowadays, due to the high-scale penetration of single-phase PV systems for residential applications, single-phase grid-connected photovoltaic systems have attracted the attention of researchers to control the active and reactive power with MPPT. Different approaches for single-stage and two-stage configurations applying conventional linear control techniques such as PI controllers, Proportional Resonant controllers, Hysteresis controllers, Fuzzy controllers, and Predictive controllers have been reported in [9]-[15]. Two-stage power conversion is currently the most common approach utilized to convert the DC current generated by the PV array into AC current through a DC-DC converter. However, from the point of view of efficiency, reliability, and cost, it is clear that the two-stage topology is not a good option especially for low voltage applications [9].

To date, only a few studies have been presented applying nonlinear control techniques for single-stage single-phase (SSSP) PV systems to transfer maximum power to the grid with unity power factor as in [31] and [35]. However, the major drawback of the single-phase voltage source inverter utilized in PV systems is the AC component of double line frequency on the DC bus, which causes deviation of the PV voltage away from the voltage at maximum power point (Vmpp) therefore, an increase in power losses [43]. The advantages related to the efficiency of the single-stage approach for single-phase systems [43] may not be significant due to the double line frequency current ripple that the

52

inverter tends to draw in single-phase PV systems. Then, in this work, first, it is proposed a novel approach to mitigate the current ripple without the necessity of a DC-DC power converter based on the studies presented by [44]. Second, using the general structure for synchronous *dq0* reference frame, configuration widely utilized in three-phase systems, the nonlinear control strategy proposed for three-phase systems in Chapter IV, is applied to the SSSP grid-connected PV systems. The controller is designed to achieve maximum power point operation regardless of atmospheric conditions and to control the active and reactive power flow to the grid. The *d*-axis current tracks the reference current I_{dref}, which novel trajectory is obtained online, taking into account the voltage dynamics of the DC link capacitor and the second harmonic current ripple. The *q*-axis current tracks the reference current I_{qref} obtained from the load requirements to guarantee unity power factor on the grid side as is required by current grid standard for low-power (e.g., several kilowatts) single-phase PV systems [42].

5.1   System Model

The full-bridge inverter topology has been widely adopted for single-phase PV systems [58]. The conventional full-bridge single-phase topology shows some features such as simple circuit structure, low cost, efficiency, and low leakage current if it is operated with bipolar SPWM [59]. For that, in this work, an SSSP grid-connected photovoltaic SPWM inverter; as shown in Figure 5.1, is utilized to control the active and the reactive power with maximum power point tracking.

From Figure 5.1, the differential equations that describe the dynamics of the single-phase model are as follows:
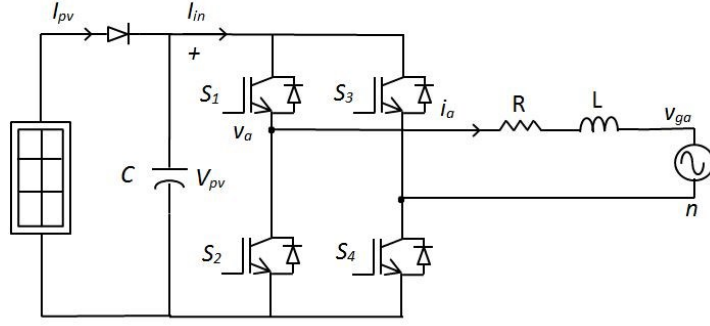
Figure 5.1 Single-stage single-phase grid-connected PV inverter

$$L\frac{di_a}{dt} = v_{an} - Ri_a - v_{ga} \tag{5-1}$$

$$C\frac{dV_{pv}}{dt} = I_{pv} - I_{in} \tag{5-2}$$

where R and L are the series equivalent resistance and inductance of the output filter and the grid impedance respectively, C is the capacitance of the input filter of the inverter, v_{ga} is the phase to neutral voltage of the grid, i_a is the output current of the inverter, I_{in} is the input current to the inverter, and I_{pv} is the current of the PV array.

5.2 Current Ripple Mitigation

In this work, in a single-stage configuration, it is proposed a novel method to mitigate the second harmonic current ripple of the PV array without the necessity of an additional power stage. For that, the estimated current ripple I_r is considered on the voltage dynamics of the DC link capacitor to model a single-stage PV system, beyond choosing an appropriate capacitor value. The estimated current ripple is subtracted from the current of the PV as is shown in Eq. (5-3).

$$C\frac{dV_{pv}}{dt} = I_{pv} - I_{in} - I_{r.} \tag{5-3}$$

The estimated current ripple is obtained assuming that the power factor on the grid side is unity. Then, neglecting the stored energy of the filter inductor, the instantaneous power p_{ac} flowing through the inverter is as follows [44].

$$p_{ac} = V_{gm}I_{am}sin^2\omega t \tag{5-4}$$

where V_{gm} is the peak voltage of the grid, I_{am} is the peak output current of the inverter, and ω is the angular frequency of the grid. Eq. (5-4) can be written as follows:

$$p_{ac} = \frac{V_{gm}I_{am}}{2}(1 - cos2\omega t). \tag{5-5}$$

The instantaneous power (p_{dc}) on the DC side of the inverter is:

$$p_{dc} = V_{pv}I_{in}. \tag{5-6}$$

From the power balance relationship and assuming that the converter is lossless,

$$p_{dc} = p_{ac}. \tag{5-7}$$

Replacing Eq. (5-5) and Eq. (5-6) into Eq. (5-7), the following equation is obtained.

$$V_{pv}I_{in} = \frac{V_{gm}I_{am}}{2} - \frac{V_{gm}I_{am}}{2}cos2\omega t \tag{5-8}$$

From Eq. (5-8), it can be seen that the power of the PV array has a DC power component and an AC power component of double line-frequency. Therefore, from the AC component of Eq. (5-8), the estimated current ripple component I_r is as follows:

$$I_r = -\frac{V_{gm}I_{am}}{2V_{pv}}cos2\omega t \tag{5-9}$$

5.3 Single-Phase Voltage Source Inverter PV Model in $\alpha\beta$ Frame

The switching functions of a single-phase inverter introduce nonlinearities and discontinuities in the converter operation. As it was mentioned in Section 3.2 of this work, the controller can be designed and easily implemented in the synchronously rotating *dq0* frame because the control variables become DC values. The *dq0* transformation, well known for three-phase systems, is utilized for the proposed single-phase system topology. However, the *dq* transformation is not straightforward for single-phase systems. In this work, it is adopted the basis of the *dq* transformation presented by [46].

Firstly, before doing the *dq* transformation, the technique is to generate a fictitious component (β component) with a phase shift of 90 degrees with respect to the original signal. The β component orthogonal to the original signal is created utilizing the phase delay of 1/4 the phase of the original signal (α component).

Assuming that the voltage of the grid is sinusoidal and symmetrical, and the grid frequency is much lower than the switching frequency [4], from Eq. (5-1) and Eq. (5-3), the equations that represent the PV system in $\alpha\beta$ frame are as follows:

$$L\frac{dI_\alpha}{dt} = -RI_\alpha + d_\alpha V_{pv} - V_{g\alpha} \qquad (5\text{-}10)$$

$$L\frac{dI_\beta}{dt} = -RI_\beta + d_\beta V_{pv} - V_{g\beta} \qquad (5\text{-}11)$$

$$C\frac{dV_{pv}}{dt} = I_{pv} - \left(d_\alpha I_\alpha + d_\beta I_\beta\right) - \left(I_{r\alpha} + I_{r\beta}\right) \qquad (5\text{-}12)$$

where I_α and I_β are the α and β components of the output current of the inverter respectively, d_α and d_β are the control functions of the inverter in $\alpha\beta$ frame, $V_{g\alpha}$ and $V_{g\beta}$

are the α and β components of the grid voltage respectively, V_{pv} and I_{pv} are the voltage and current of the PV array, $I_{r\alpha}$ and $I_{r\beta}$ are the $\alpha\beta$ components of the second harmonic current ripple. From Eq. (5-9), the $\alpha\beta$ components of the second harmonic current ripple are given by the following equations:

$$I_{r\alpha} = -\frac{V_{gm}I_{am}}{2V_{pv}}cos2\omega t \tag{5-13}$$

$$I_{r\beta} = -\frac{V_{gm}I_{am}}{2V_{pv}}sin2\omega t \tag{5-14}$$

5.4 Single-Phase Voltage Source Inverter PV Model in *dq* Frame

5.4.1 *dq* Transformation of Single-Phase Systems

Once, the two orthogonal $\alpha\beta$ components (Clarke components) are obtained, it is possible to represent the model of the single-phase PV system in *dq* reference frame rotating at the angular frequency ω of the grid applying the transformation matrix T, which is obtained from Figure 5.2 using trigonometric relationships [57].
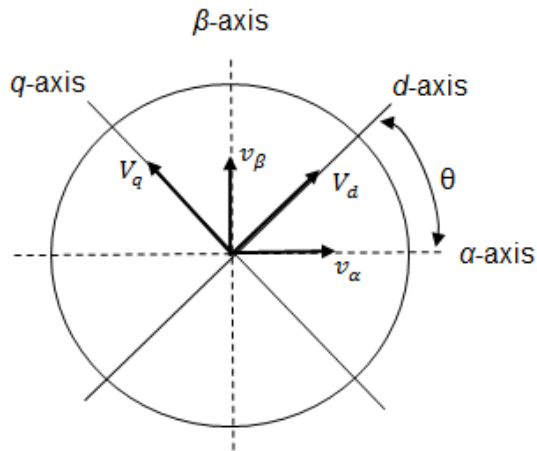
Figure 5.2 $\alpha\beta$ and *dq* components relationship

Then, the d-axis and q-axis components are given by the following equations:

$$V_d = v_\alpha \cos\theta + v_\beta \sin\theta \qquad (5\text{-}15)$$

$$V_q = -v_\alpha \sin\theta + v_\beta \cos\theta. \qquad (5\text{-}16)$$

From Eq. (5-15) and Eq. (5-16), transformation matrix $T \in \mathbb{R}^{2x2}$ is given by the following expression [46]

$$T = \begin{bmatrix} \cos\theta & \sin\theta \\ -\sin\theta & \cos\theta \end{bmatrix} \qquad (5\text{-}17)$$

where the displacement angle θ is given by Eq. (3-13). The inverse of the transformation matrix is as follows:

$$T^{-1} = \begin{bmatrix} \cos\theta & -\sin\theta \\ \sin\theta & \cos\theta \end{bmatrix}. \qquad (5\text{-}18)$$

The generalized forms of the transformation from $\alpha\beta$ components to dq components and vice versa are:

$$\begin{bmatrix} F_d \\ F_q \end{bmatrix} = T \begin{bmatrix} F_\alpha \\ F_\beta \end{bmatrix} \qquad (5\text{-}19)$$

$$\begin{bmatrix} F_\alpha \\ F_\beta \end{bmatrix} = T^{-1} \begin{bmatrix} F_d \\ F_q \end{bmatrix} \qquad (5\text{-}20)$$

$\begin{bmatrix} F_{dq} \end{bmatrix}$ and $\begin{bmatrix} F_{\alpha\beta} \end{bmatrix}$ stand for voltage or current in dq frame and $\alpha\beta$ frame respectively.

5.4.2   Single-Phase Grid-Connected PV System Model

The stationary $\alpha\beta$ model given by Eq. (5-10) and Eq. (5-11), is transformed to the dq synchronously rotating frame using the transformation matrix T given by Eq. (5-17). Then, from (5-19)

$$\begin{bmatrix} I_d \\ I_q \end{bmatrix} = \begin{bmatrix} cos\theta & sin\theta \\ -sin\theta & cos\theta \end{bmatrix} \begin{bmatrix} I_\alpha \\ I_\beta \end{bmatrix} \tag{5-21}$$

where $\theta = \omega t$ for the frequency of the grid.

Taking the time derivative of Eq. (5-21) and then, utilizing Eq. (5-20) for current, the following equation is obtained:

$$\begin{bmatrix} \dot{I}_d \\ \dot{I}_q \end{bmatrix} = \omega \begin{bmatrix} -sin\omega t & cos\omega t \\ -cos\omega t & -sin\omega t \end{bmatrix} \begin{bmatrix} cos\omega t & -sin\omega t \\ sin\omega t & cos\omega t \end{bmatrix} \begin{bmatrix} I_d \\ I_q \end{bmatrix} + \begin{bmatrix} cos\omega t & sin\omega t \\ -sin\omega t & cos\omega t \end{bmatrix} \begin{bmatrix} \dot{I}_\alpha \\ \dot{I}_\beta \end{bmatrix}. \tag{5-22}$$

After some mathematical work in Eq. (5-22), Eq. (5-23) is obtained.

$$\begin{bmatrix} \dot{I}_d \\ \dot{I}_q \end{bmatrix} = \begin{bmatrix} 0 & w \\ -w & 0 \end{bmatrix} \begin{bmatrix} I_d \\ I_q \end{bmatrix} + \begin{bmatrix} cos\omega t & sin\omega t \\ -sin\omega t & cos\omega t \end{bmatrix} \begin{bmatrix} \dot{I}_\alpha \\ \dot{I}_\beta \end{bmatrix} \tag{5-23}$$

From Eq. (5-10) and Eq. (5-11), the matrix form is as follows:

$$\begin{bmatrix} \dot{I}_\alpha \\ \dot{I}_\beta \end{bmatrix} = -\frac{R}{L} \begin{bmatrix} I_\alpha \\ I_\beta \end{bmatrix} + \frac{V_{pv}}{L} \begin{bmatrix} 1 & 0 \\ 0 & 1 \end{bmatrix} \begin{bmatrix} d_\alpha \\ d_\beta \end{bmatrix} - \frac{1}{L} \begin{bmatrix} V_{g\alpha} \\ V_{g\beta} \end{bmatrix}. \tag{5-24}$$

Multiplying Eq. (5-24) by T matrix and then, the obtained result replacing into Eq. (5-23), after some mathematical work, the following equation is obtained:

$$\begin{bmatrix} \dot{I}_d \\ \dot{I}_q \end{bmatrix} = \begin{bmatrix} 0 & w \\ -w & 0 \end{bmatrix} \begin{bmatrix} I_d \\ I_q \end{bmatrix} - \frac{R}{L} \begin{bmatrix} I_d \\ I_q \end{bmatrix} + \frac{V_{pv}}{L} \begin{bmatrix} d_d \\ d_q \end{bmatrix} - \frac{1}{L} \begin{bmatrix} V_{gd} \\ V_{gq} \end{bmatrix}. \tag{5-25}$$

Equation (5-25) can be written as:

$$L\dot{I}_d = -RI_d + L\omega I_q + d_d V_{pv} - V_{gd} \tag{5-26}$$

$$L\dot{I}_q = -RI_q - L\omega I_d + d_q V_{pv} - V_{gq} \tag{5-27}$$

where $I_d(t)$ and $I_q(t)$ are the d-axis and q-axis current components of the output current of the inverter, $V_{gd}(t)$ and $V_{gq}(t)$ are the *d*-axis and *q*-axis voltage component of the

voltage of the grid, ω is the angular frequency of the grid, and $d_d(t)$ and $d_q(t)$ are the control signals of the inverter in qd frame.

Similarly, the $\alpha\beta$ components of the voltage dynamics of the DC link capacitor given by Eq. (5-12) are transformed to the dq frame utilizing the transformation matrix T. First, the component $d_\alpha I_\alpha + d_\beta I_\beta$ of Eq. (5-12) can be written in matrix form as follows:

$$d_\alpha I_\alpha + d_\beta I_\beta \triangleq [d_\alpha \quad d_\beta] \begin{bmatrix} I_\alpha \\ I_\beta \end{bmatrix} \tag{5-28}$$

Then, utilizing Eq. (5-20), Eq. (5-28) can be written as:

$$d_\alpha I_\alpha + d_\beta I_\beta = \left[\begin{bmatrix} cos\omega t & -sin\omega t \\ sin\omega t & cos\omega t \end{bmatrix} \begin{bmatrix} d_d \\ d_q \end{bmatrix} \right]^T \begin{bmatrix} cos\omega t & -sin\omega t \\ sin\omega t & cos\omega t \end{bmatrix} \begin{bmatrix} I_d \\ I_q \end{bmatrix} \tag{5-29}$$

After some mathematical work in Eq. (5-29), the following equation is obtained:

$$d_\alpha I_\alpha + d_\beta I_\beta = d_d I_d + d_q I_q. \tag{5-30}$$

Second, the component $(I_{r\alpha} + I_{r\beta})$ of Eq. (5-12), that represents the estimation of the second harmonic current ripple, is transformed to dq reference frame utilizing the transformation matrix given by Eq. (5-17) with the angle $\theta = 2\omega t$. Then, the dq transformation of the referred component is as follows:

$$\begin{bmatrix} I_{rd} \\ I_{rq} \end{bmatrix}^T = \left[\begin{bmatrix} cos2wt & sin2wt \\ -sin2wt & cos2wt \end{bmatrix} \begin{bmatrix} I_{r\alpha} \\ I_{r\beta} \end{bmatrix} \right]^T. \tag{5-31}$$

Replacing Eq. (5-13) and Eq. (5-14) into Eq. (5-31), after some mathematical work, the dq components of the estimated second harmonic current ripple are:

$$I_{rd} = -\frac{V_{gd} I_d}{2V_{pv}} \tag{5-32}$$

60

$$I_{rq} = 0 \qquad \text{(5-33)}$$

Then, replacing equations (5-30), (5-32) and (5-33) into Eq. (5-12), the equation that represents the dynamics of the DC link capacitor including the estimation of the second harmonic current ripple in *dq* synchronously rotating reference frame is as follows:

$$C\frac{dV_{pv}}{dt} = I_{pv} - d_a I_d - d_q I_q - \left(-\frac{V_{gd}I_d}{2V_{pv}}\right). \qquad \text{(5-34)}$$

It can be seen that Eq. (5-26) and Eq. (5-27) are similar to those of the three-phase system given by Eq. (3-30) and Eq. (3-31). This similarity facilitates the design of the single-phase controller because the basis of the nonlinear controller design; stated for three-phase systems in chapter IV, are utilized for the design of the single-phase controller. It is clear that, the voltage dynamics of the DC link capacitor given by Eq. (5-34) differs from that of the three-phase system given by Eq. (3-32) in the added component to mitigate the second harmonic current ripple. Furthermore, it can be seen from (5-26) and (5-27) that there is a cross-coupling dependence of I_d and I_q currents. Hence, as it was stated in chapter IV the auxiliary control functions d'_d and d'_q defined to decouple the active and reactive currents loops and facilitate the model analysis are as follows:

$$d'_d = d_d + \frac{\omega L}{V_{pv}} I_q \qquad \text{(5-35)}$$

$$d'_q = d_q - \frac{\omega L}{V_{pv}} I_d \qquad \text{(5-36)}$$

Substituting (5-35) and (5-36) into (5-26), (5-27), and (5-34) the equations of the model are:

$$L\dot{I}_d = -RI_d + d'_d V_{pv} - V_{gd} \qquad (5\text{-}37)$$

$$L\dot{I}_q = -RI_q + d'_q V_{pv} - V_{gq} \qquad (5\text{-}38)$$

$$C\dot{V}_{pv} = I_{pv} - d'_d I_d - d'_q I_q - I_{rd} \qquad (5\text{-}39)$$

CHAPTER VI

CONTROL SYSTEM DEVELOPMENT OF THE SINGLE-PHASE
PHOTOVOLTAIC SYSTEM

A nonlinear control strategy for SSSP grid-connected PV inverter in synchronous *dq* reference frame is proposed to achieve maximum power point operation, regardless of the atmospheric conditions, and to control the active and reactive power. The control scheme forces the *d*-axis current to track the novel trajectory reference current $I_{dref}(t)$, obtained online. It provides for energy balance from the input to the output of the system along with mitigating the PV second harmonic current ripple, which is a major drawback of the single-phase PV inverters. Additionally, the grid-connected PV system must work at MPP, for that, the voltage of the PV array must track the reference voltage obtained from the Incremental Conductance algorithm. The block diagram of the single-stage single-phase PV system based on nonlinear control is shown in Figure 6.1.
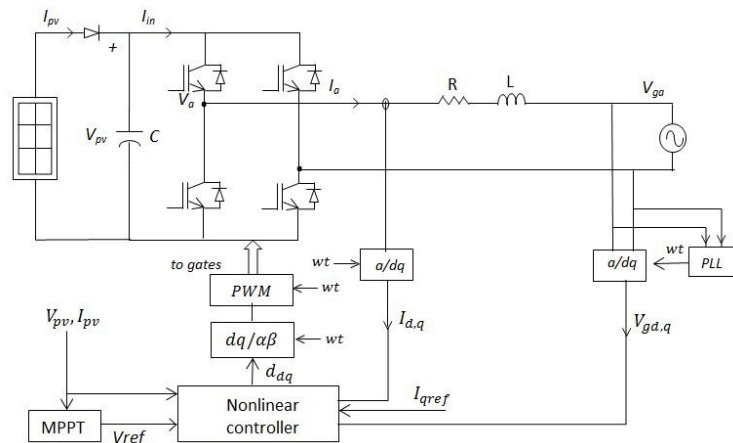
Figure 6.1 Single-stage single-phase PV system with nonlinear controller

6.1 Control Design

The objective of the control scheme is to design the duty ratio control signals $d'_d(t)$ and $d'_q(t)$ such that $I_d(t) \to I_{dref}(t)$ and $I_q(t) \to I_{qref}(t)$ as $t \to \infty$, thus controlling the active and the reactive power of the system to keep the unity power factor on the grid side. Moreover, the control law must also ensure that $V_{pv}(t) \to V_{ref}(t)$ as $t \to \infty$ to achieve MPP. $I_{dref}(t)$, $I_{qref}(t)$, and $V_{ref}(t)$ are the desired values of current and voltage respectively.

To facilitate the control development, the assumptions considered in chapter IV for three-phase systems are valid for single-phase system because the models in dq frame for both three-phase and single-phase are similar. Thus, for the single-phase system the following is assumed:

Assumption 1. $R, L, C \in \mathbb{R}^+$ are known constant parameters of the system.

Assumption 2. The q axis reference current I_{qref} is measurable and sufficiently differentiable. Thus, I_{qref} and $\dot{I}_{qref}$ are bounded.

Assumption 3. The voltage of the grid is sinusoidal and symmetrical. The d-axis grid voltage is equal to 170 V., and q-axis grid voltage is zero.

Assumption 4. The reference voltage V_{ref} is measurable and sufficiently differentiable. Thus, V_{ref} and $\dot{V}_{ref}$ are bounded.

Assumption 5. The current I_{pv} is bounded on the condition that the voltage V_{pv} is bounded.

To meet with the desired currents and voltage to achieve MPPT and to control the active and reactive power, the tracking errors signal of the current $e_d(t)$ and $e_q(t)$, and the tracking error signal of the PV voltage $e_v(t)$ are defined as follows:

$$e_d \triangleq I_d - I_{dref} \tag{6-1}$$

$$e_q \triangleq I_q - I_{qref} \tag{6-2}$$

$$e_v \triangleq V_{pv} - V_{ref}. \tag{6-3}$$

where $e_d(t)$, $e_q(t)$, $e_v(t) \in \mathbb{R}$. These signals will facilitate the design of the auxiliary control signals d'_d, d'_q, and the d-axis reference current I_{dref}.

The time derivative of the equations (6-1), (6-2), and (6-3) are as follows:

$$\dot{e}_d = \dot{I}_d - \dot{I}_{dref} \tag{6-4}$$

$$\dot{e}_q = \dot{I}_q - \dot{I}_{qref} \tag{6-5}$$

$$\dot{e}_v = \dot{V}_{pv} - \dot{V}_{ref}. \tag{6-6}$$

Multiplying both sides of Eq. (6-4) and Eq. (6-5) by the inductance L and Eq. (6-6) by the capacitance C, then substituting the system dynamic equations (5-37), (5-38), and (5-39) into the obtained equations respectively, the open loop system is developed as follows:

$$L\dot{e}_d = -RI_d + d'_d V_{pv} - V_{gd} - L\dot{I}_{dref} \tag{6-7}$$

$$L\dot{e}_q = -RI_q + d'_q V_{pv} - L\dot{I}_{qref} \tag{6-8}$$

$$C\dot{e}_v = I_{pv} - d'_d I_d - d'_q I_q - I_{rd} - C\dot{V}_{ref} \tag{6-9}$$

To design the control signals $d'_d(t)$ and $d'_q(t)$ ensuring that the error signals e_d and $e_q \to$ 0 as $t \to \infty$, the closed loop error signals are designed as follows:

$$L \dot{e}_d = -K_4 e_d \tag{6-10}$$

$$L \dot{e}_q = -K_5 e_q \tag{6-11}$$

where K_4 and K_5 are positive constant control gains.

Replacing Eq. (6-10) and Eq. (6-11) into Eq. (6-7) and Eq. (6-8) respectively, after some mathematical work, the auxiliary control signals d'_d and d'_q are obtained:

$$d'_d = \frac{1}{V_{pv}} \left(-K_4 e_d + R I_d + V_{gd} + L \dot{I}_{dref} \right) \tag{6-12}$$

$$d'_q = \frac{1}{V_{pv}} \left(-K_5 e_q + R I_q + L \dot{I}_{qref} \right) \tag{6-13}$$

6.2   Design of *d*-axis Reference Current Trajectory for the Single-Phase PV System

Replacing equations (6-12) and (6-13) into Eq. (6-9), the following equation is obtained.

$$C \dot{e}_v = -\frac{I_d}{V_{pv}} \left(-K_4 e_d + R I_d + V_{gd} + L \dot{I}_{dref} \right) - \frac{I_q}{V_{pv}} \left(-K_5 e_q + R I_q + L \dot{I}_{qref} \right)$$
$$+ I_{pv} - I_{rd} - C \dot{V}_{ref} \tag{6-14}$$

To ensure that the error signal $e_v \to 0$ as $t \to \infty$ the closed loop error signal of the PV voltage is designed as follows:

$$C \dot{e}_v = -K_6 e_v \tag{6-15}$$

where K_6 is a positive control gain. Combining Eq. (6-14) with Eq. (6—15), the equation to obtain the trajectory of the reference current $I_{dref}(t)$ is designed as:

$$\dot{I}_{dref} = \frac{K_5 e_q}{L} \frac{I_q}{I_d} + \frac{K_6 e_v}{L} \frac{V_{pv}}{I_d} + \frac{V_{pv} I_{pv}}{L I_d} - \frac{C}{L} \frac{V_{pv}}{I_d} \dot{V}_{ref} - \frac{I_q}{I_d} \dot{I}_{qref} - \frac{R I_q^2}{L I_d} +$$

$$\frac{K_4}{L} e_d - \frac{R}{L} I_d - \frac{1}{L} V_{gd} - \frac{V_{pv}}{L I_d} I_{rd}$$

(6-16)

Equation (6-16) contains the term that is a function of the estimated current ripple I_{rd}. Therefore, Eq. (6-16) is utilized to show the effect of the second harmonic current ripple in obtaining the maximum power, hence the reference current I_{dref}.

6.3 Stability Analysis

As it was stated in section 4.3, the Lyapunov stability theory is used to prove the stability of the system and convergence of the closed loop error signals.

Theorem 2: Using the closed loop error system given by (6-10), (6-11), and (6-15), the error signals defined in (6-1), (6-2), and (6-3) are exponentially regulated as follows:

$$e_d(t), e_q(t), e_v(t) \to 0 \ as \ t \to \infty$$

(6-17)

Proof: A non-negative Lyapunov function candidate is chosen as:

$$V_2 = \frac{1}{2} L e_d^2 + \frac{1}{2} L e_q^2 + \frac{1}{2} C e_v^2$$

(6-18)

The time derivative of Eq. (6-18) is:

$$\dot{V}_2 = e_d L \dot{e}_d + e_q L \dot{e}_q + e_v C \dot{e}_v.$$

(6-19)

To guarantee that the error signals e_d, e_q, and $e_v \to 0 \ as \ t \to \infty$ the closed loop error signals were defined by equations (6-10), (6-11), and (6-15). Then, replacing these equations into Eq. (6-19), the following equation is obtained:

$$\dot{V}_2 = -K_4 e_d^2 - K_5 e_q^2 - K_6 e_v^2 \tag{6-20}$$

Since the control gains K_4, K_5, K_6 are positive, it is clear that $\dot{V}_2$ is a negative definite function. Given by Eq. (6-18) and Eq. (6-20), utilizing *Definition 3.5* stated in [51] it can be shown that the origin $\left(e_d(t), e_q(t), e_v(t)\right) = (0,0,0)$ is globally exponentially stable. Exponential stability allows knowing the rate of exponential convergence γ [51] to estimate how fast the system trajectory tends to zero. The prove of the theorem is similar to that shown in section 4.3, ignoring previous values of the parameters R, L, and C and changing the control gains K_1, K_2, K_3 by K_4, K_5, K_6 respectively. For single-phase scheme, $\lambda_{Zmax} = L = 0.008$, $\lambda_{Zmin} = C = 0.0036$, $\lambda_{Kmax} = K_5 = 40$, $\lambda_{Kmin} = K_6 = 1$, $\gamma = \frac{\lambda_{Kmin}}{\lambda_{Zmax}} = 125$.

6.4 Simulation Results of the Single-Phase PV System

A numerical simulation was performed to validate the control design. The parameters of the single-phase PV system are summarized in Table 6.1 and Table 6.2.

Table 6.1 System Parameters of the Single-Phase PV System

Parameter	Value	Units	Parameter	Value	Units
R	0.1	Ω	K_4	16	$-$
L	8	mH	K_5	40	$-$
C	3600	μF	K_6	1	$-$
f_{sw}	12	kHz	v_{step}	$5e^{-4}$	V
f	60	Hz	V_g	120	$Vph(rms)$

f_{sw} is the switching frequency and v_{step} is the voltage step of the MPPT algorithm.

Table 6.2 Photovoltaic Module Parameters

Module Sunpreme SNPM-F60-02-180	
Maximum Power (180.42 W)	*Cells per module (60)*
Open circuit voltage Voc	36.6 V
Short circuit current Isc	6.9 A
Voltage MPP	29.1 V
Current MPP	6.2 A
Parallel string	2
Series strings	8
Vmpp at 25 °C and 1000 W/m^2	232.8 V
Impp at 25 °C and 1000 W/m^2	12.4 A
Pmax at 25 °C and 1000 W/m^2	2.887 KW
Pmax at 25 °C and 800 W/m^2	2.331 KW
Pmax at 25 °C and 600 W/m^2	1.759 KW

To show the effectiveness of the proposed method to mitigate the current ripple of the PV array, first, the I_{rd} component, which represents the estimated current ripple, was set to zero in Eq. (6-9) and Eq. (6-16). Figure 6.2 shows the PV voltage and the reference voltage at 1000 W/m². The PV voltage has a mean value of approximately 245.46 volts and a ripple of 9.8 volts peak to peak (4% ripple). Moreover, it can be seen that the deviation of the voltage mean value respect to the reference voltage is about 11.3 volts. Figure 6.3 shows that the PV current has a mean value of 11.25 amperes and a ripple of about 1.08 amperes peak to peak. The mean value of current is below the value given by the specifications in Table 6.2 (12.4 amperes). Figure 6.4 shows the PV power and the maximum power. The deviation of the power mean value respect to the maximum power is approximately 4.1%.
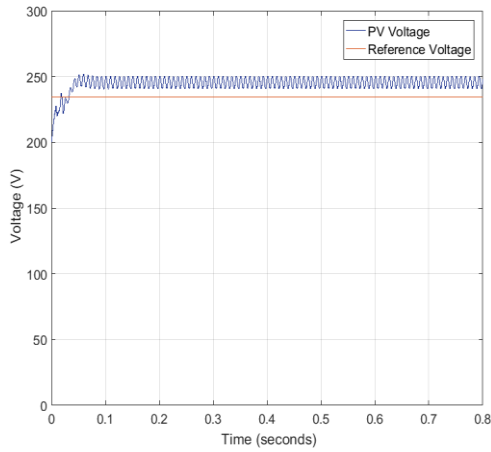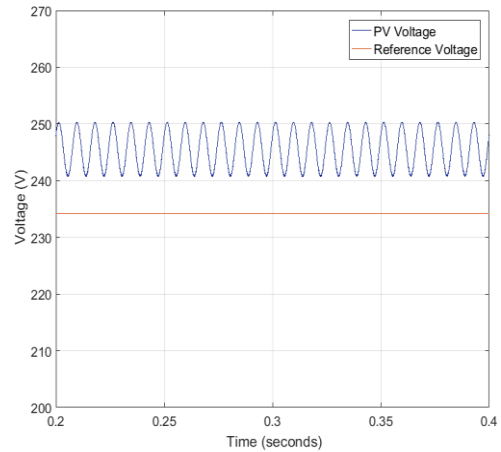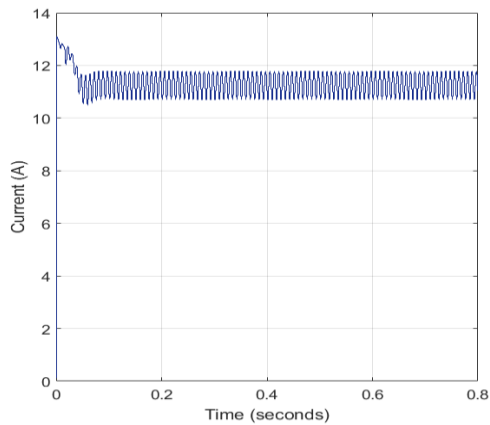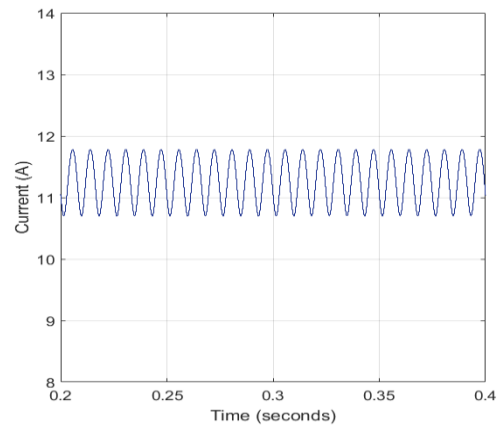
Figure 6.2 PV voltage and reference voltage without attenuation of current ripple, a) Full time scale, b) Time range from (0.2, 0.4 seconds).

Figure 6.3 PV current without attenuation of current ripple, a) Full time scale, b) Time range from (0.2, 0.4 seconds).

Second, applying the proposed approach to attenuate the current ripple, Figure 6.5 shows the PV voltage and the reference voltage. In this figure, the PV voltage mean value has zero deviation from the reference voltage demonstrating the effectiveness of the proposed method to attenuate the current ripple thus to diminish the voltage deviation.
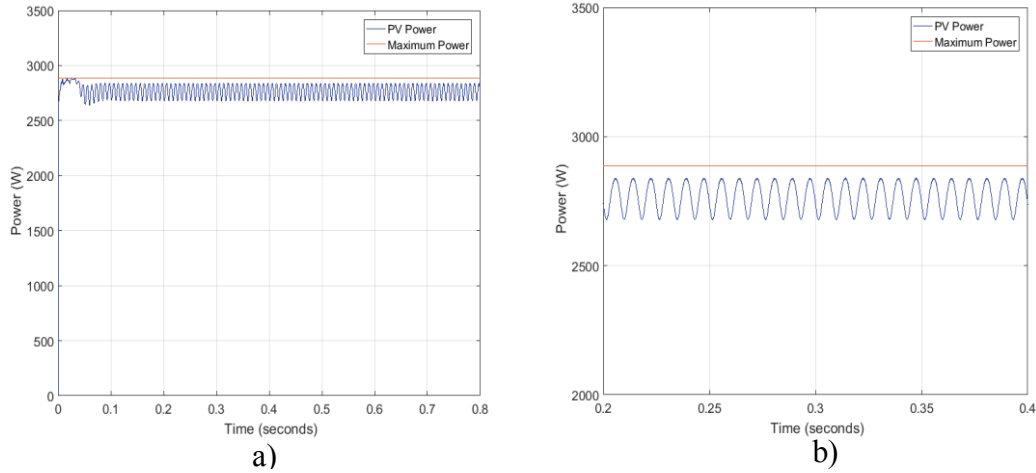
Figure 6.4 PV power and maximum power without attenuation of current ripple, a) Full time scale, b) Time range from (0.2, 0.4 seconds).
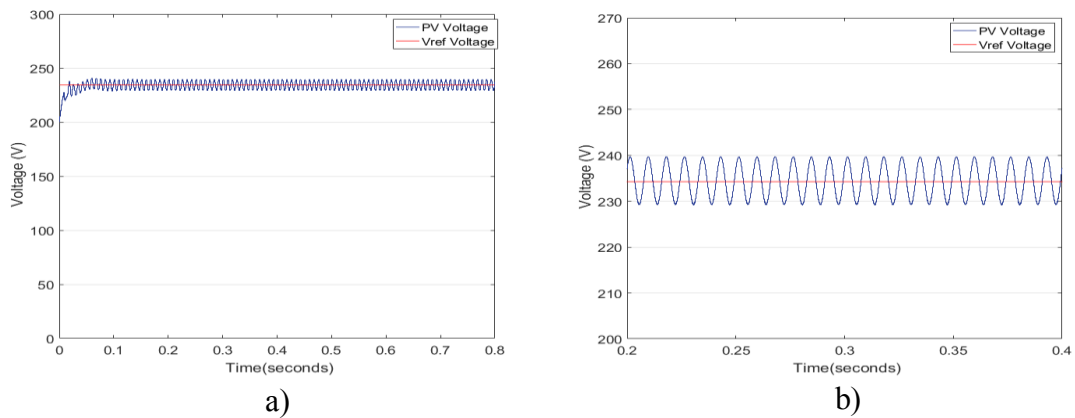
Figure 6.5 PV voltage at 1000 W/m^2 with mitigation of the current ripple, a) Full time scale, b) Time range from (0.2, 0.4 seconds).

Figure 6.6 shows the PV current, which mean value is about 12.2 amperes and a ripple of approximately 0.65 amperes peak to peak. It is clear that the mean value is very close to the mean value given in Table 6.2 (12.4 amperes). Figure 6.7 shows the PV power applying the proposed method for current ripple attenuation. The obtained PV power is very close to the maximum power given in Table 6.2. The deviation of the mean power respect to the maximum power is approximately 0.71 % at 1000 W/m².Thus, showing the effectiveness of the proposed approach to mitigate the current ripple.

71

Figure 6.6 PV Current with attenuation of the current ripple at 1000 W/m2, a) Full time scale, b) Time range from (0.2, 0.4 seconds).
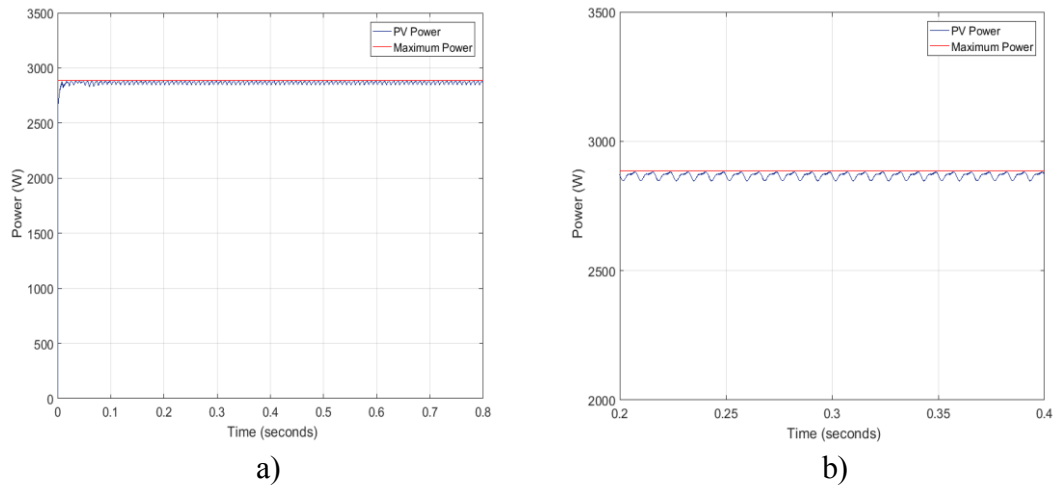
Figure 6.7 PV power and maximum power with attenuation of current ripple at 1000 W/m^2 , a) Full time scale, b) Time range from (0.2, 0.4 seconds).
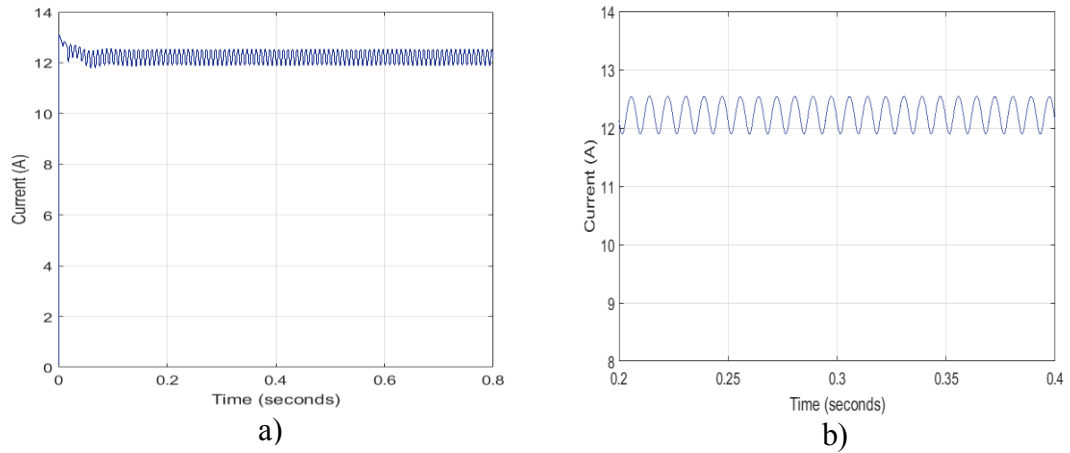
From the obtained results, it can be seen that the effect of the second harmonic component is to deviate the PV voltage from the voltage at MPP and therefore the drop of the maximum power. The power losses due to the deviation of the maximum power operation are decreased applying the proposed method. Additionally, the second harmonic PV current ripple has been attenuated by approximately 42 %, a value that is close to the value obtained in [45], showing the effectiveness of the proposed approach to mitigate the second harmonic photovoltaic current.

72

Second, to evaluate the performance of the control scheme under sudden changes in atmospheric conditions, the irradiance was changed in steps from 0 to 600 to 1000, and finally back to 800 W/m² at time t = 0, 0.3, 0.6 seconds respectively at a temperature of 25 ^0C as is shown in Figure 6.8. Figure 6.9 shows the steady state and dynamics response of the PV power as the irradiance changes, which power values, are close to the maximum values. Therefore, validating the use of the proposed model in a single-stage single-phase scheme combined with the incremental conductance algorithm to obtain the reference voltage and thus the maximum power.
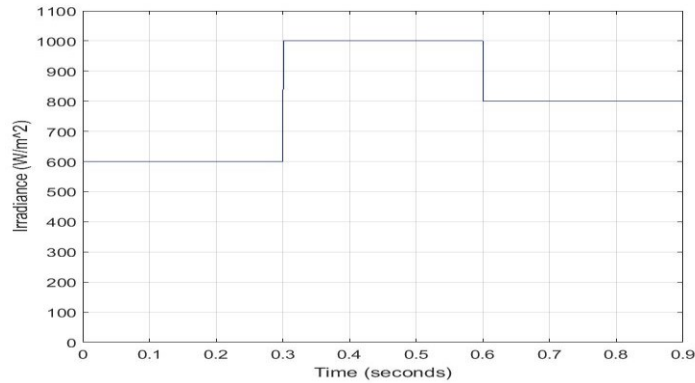
Figure 6.8 Irradiance for various atmospheric conditions
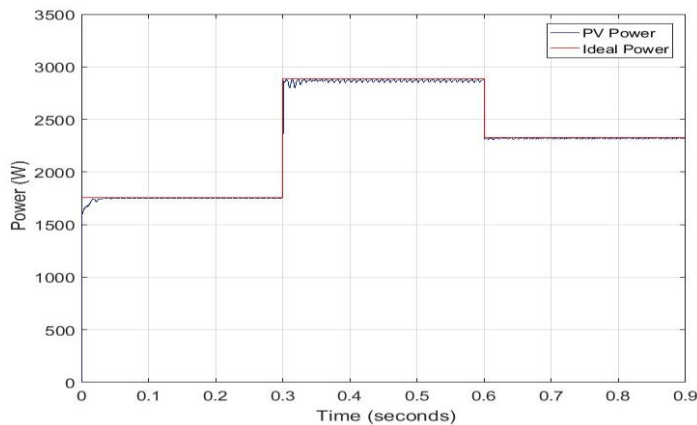
Figure 6.9 PV array power and ideal maximum power

The tracking errors $e_d(t)$, $e_q(t)$ and $e_v(t)$ are shown in Figure 6.10. It shows that the tracking errors are approximately regulated to zero, hence validating the performance of the proposed nonlinear controller. Fig. 6.11 shows the d-axis and q-axis currents both with their respective reference currents. It can be seen that the current $I_d(t)$ follows the reference current $I_{dref}(t)$, which novel trajectory was obtained using Eq. (6-16). The current $I_q(t)$ follows $I_{qref}(t)$ which, for this case example, was set to zero to guarantee unity power factor on the grid side.

a)

b)

c)
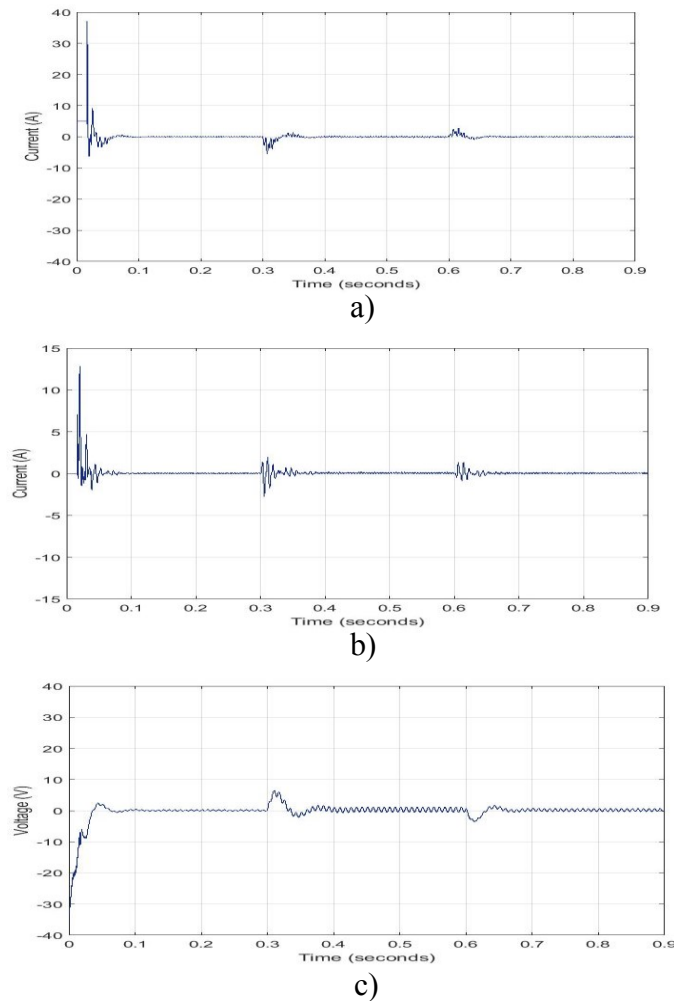
Figure 6.10 Tracking error a) error $e_d(t)$, b) error $e_q(t)$, c) error $e_v(t)$
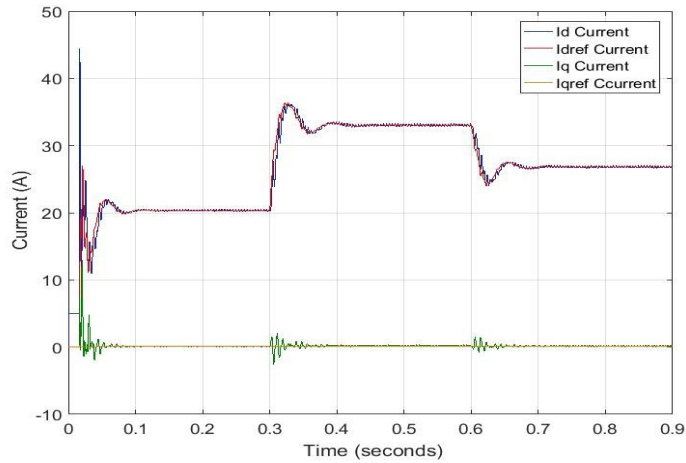
Figure 6.11 $I_d(t)$ and $I_q(t)$ currents with $I_{dref}(t)$ and $I_{qref}(t)$ reference currents

Figure 6.12 shows the reference voltage $V_{ref}(t)$, obtained from the INC algorithm, and the capacitor voltage, which is the voltage of the PV array $V_{pv}(t)$. It can be seen that the PV voltage follows the reference voltage and it is kept steady despite the sudden changes of the irradiance, thus showing the robustness of the proposed controller to rapid changes of the irradiance.
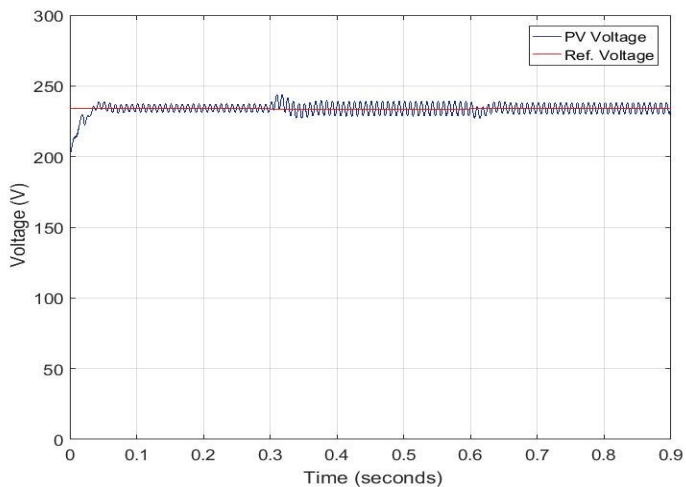
Figure 6.12 PV voltage $V_{pv}(t)$ and reference voltage $V_{ref}(t)$

Figure 6.13 shows the grid voltage and current for different values of irradiance. The current is sinusoidal and in phase with the voltage, meaning that the grid is only receiving active power. Therefore, the power factor is unity, as it was desired. Additionally, when there is a step change of the irradiance, the transient time to get the new steady state and therefore the synchronism between the phase-voltage and the current is approximately less than three cycles, thus showing the robustness of the proposed closed loop controlled PV system.
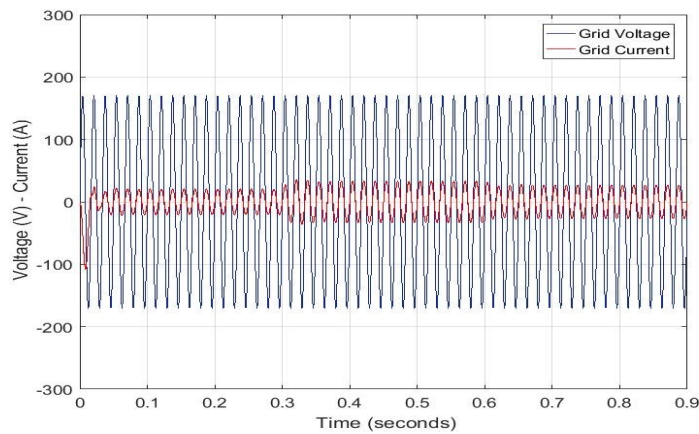
Figure 6.13 Grid voltage and current

Figure 6.14 shows a zoom-in version of Figure 6.13 where the transition of the grid current when the irradiance changes from 600 to 1000 W/m^2 at t= 0.3 seconds can be seen. Figure 6.15 shows the harmonic components of the grid current when the irradiance is 600 W/m^2. It shows that the current has harmonic components less than 0.3%, with total harmonic distortion of approximately 1.83 %. This value is well below the IEEE-519 standard requirements.
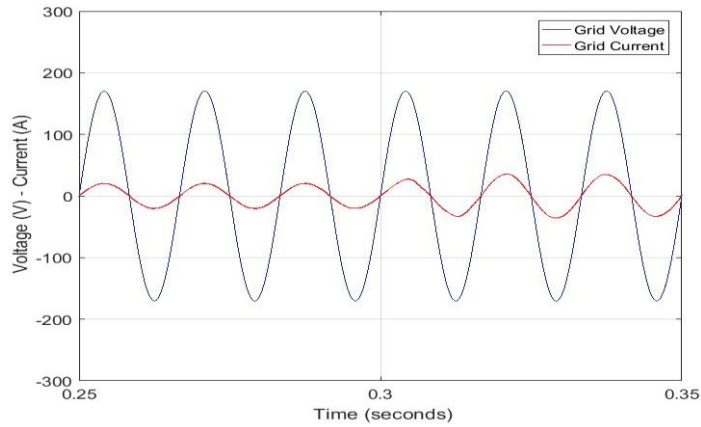
Figure 6.14 Transient response of the grid current at t=0.3 s.
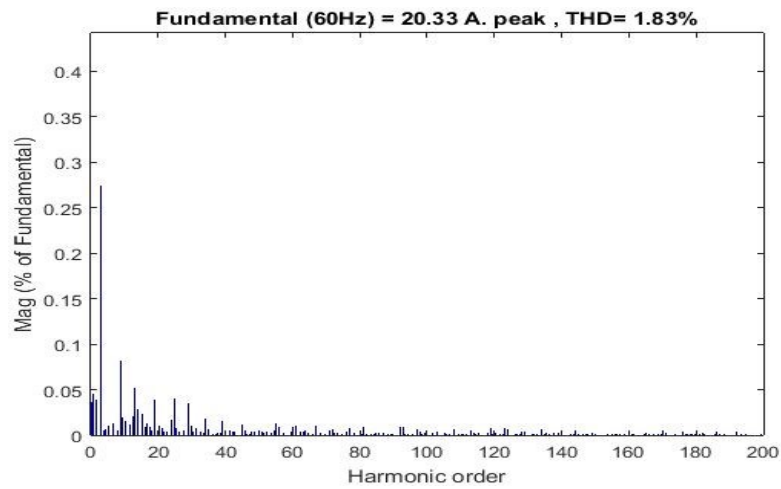
Figure 6.15 Harmonic components of the grid current at $600\ W/m^2$

Finally, at irradiance of $600\ W/m^2$, an *R-L* load was connected at time t = 0.3 seconds to see the performance of the controller to manage the active and reactive power. Figure 6.16 shows the grid voltage, grid current, and load current when it is connected a load of 1000 W, and 500 Var, 120 Vac. It can be seen that the current is lagging an angle of about 26.5 degrees. Moreover, despite that the load is requiring reactive power once the load is connected, the grid current is in phase with the voltage. Thus the power factor is the unity on the grid side, showing the effectiveness of the proposed controller on

compensating the reactive power required by the load. Figure 6.17 shows the harmonics components of the grid current when the load is connected to the point of common coupling. It has a THD of about 4.59%, a value that is below the IEEE-519 standard requirements.
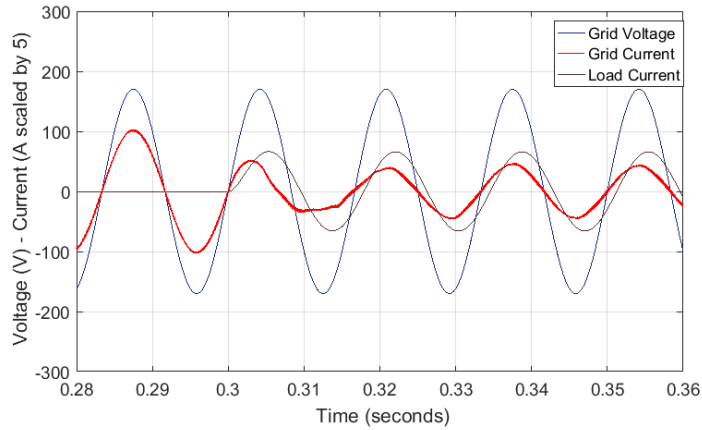
Figure 6.16 Grid voltage and current, and load current with an R-L load connected at time t= 0.3 s.
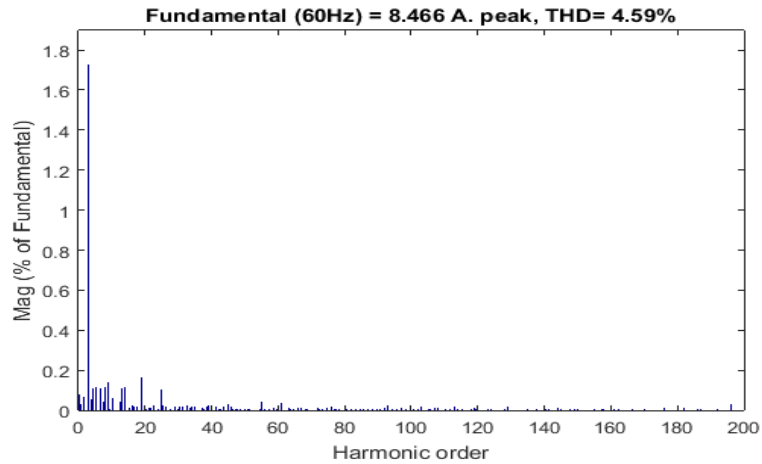
Figure 6.17 Harmonic components of the grid current with R-L load at 600 W/m^2

CHAPTER VII

ADAPTIVE ESTIMATION OF UNKNOW DISTURBANCES FOR THE SINGLE-PHASE SYSTEM

Physically the un-modeled non-idealities, such as unequal rising and falling edge delays of the gate drive circuit [55], could affect the performance of the controller in hardware implementation. Therefore, it is important to include these unknown disturbances in the design of the controller.

Due to the high-scale penetration of single-phase PV modules, transformerless PV inverters are being widely adopted [42]. However, this has imposed new challenges to distributed generation because grid standard and regulations (such as the IEEE standard 1547) require disconnecting the PV system in the event of grid faults [48], [58]. Disconnecting the PV system from the grid will cause adverse operations that could negatively affect the power quality supplied to the customer [60]. For that, some researchers as in [58] and [60] states that future PV systems will have to provide ancillary services, for example, low voltage ride through (LVRT) under grid faults.

Motivated by these ancillary services, the nonlinear controller analyzed in Chapter V is modified combining the nonlinear control with adaptive control, first, to include the constant unknown disturbances to the switching function of the inverter that will be adaptively estimated and second, to supply reactive power to the grid when there is an

LVRT event maintaining the maximum active power constant. For that, the q-axis reference current is calculated based on the equation stated in [58].

$$I_{qref} = K\left(1 - \frac{V_{gd}}{170}\right)I_N \tag{7-1}$$

where V_{gd} is the d-axis grid voltage, $K \geq 2\,p.u.$ [58], I_N is the rated current of the inverter. From Eq. (7-1) it can be seen that if $V_{gd} = 170\,V$ for normal operation, thus the q-axis reference current $I_{qref} = 0$.

The dynamic model of the system proposed in Chapter V is modified as follows:

$$L\frac{di_a}{dt} = -Ri_a + (d + d_0)V_{pv} - v_{ga} \tag{7-2}$$

$$C\frac{dV_{pv}}{dt} = I_{pv} - (d + d_0)i_a \tag{7-3}$$

where R and L are the series equivalent resistance and inductance of the output filter and the grid impedance respectively, C is the capacitance of the DC link, $v_{ga}(t)$ is the grid voltage, $i_a(t)$ is the inverter output current, $V_{pv}(t)$ and $I_{pv}(t)$ are the PV voltage and current, $d(t)$ is the duty ratio control signal, and d_0 represents the unknown disturbances, which could appear physically in the circuit such as imperfect switch timing [41].

In Section 5.2, an estimated current ripple of the PV array was considered on the voltage dynamics of the DC link capacitor to mitigate the current ripple. Moreover, the power factor on the grid side was assumed to be unity as it is required by current grid standards for PV applications [42]. However; for next-generation PV systems, PV systems could supply reactive power into the grid under grid faults or LVRT events [58]. Then, the power factor would not be unity. For that, in this section, the phase-angle between the voltage and the current of the grid is considered in the design.

To facilitate the analysis, the stored energy of the filter inductor is neglected [44]. Then, the instantaneous output power $p_{ac}(t)$ of the inverter is as follows:

$$p_{ac} = \frac{V_{gm}I_{am}}{2}cos\varphi - \frac{V_{gm}I_{am}}{2}cos(2\omega t - \varphi). \tag{7-4}$$

In Eq. (7-4), V_{gm} is the grid peak voltage, I_{am} is the inverter peak output current, ω represents the grid angular frequency, and φ the phase-angle between the grid voltage and current. Then, from the power balance relationship and dismissing the inverter power losses, the instantaneous input power of the inverter is given by the following equation:

$$V_{pv}I_{in} = \frac{V_{gm}I_{am}}{2}cos\varphi - \frac{V_{gm}I_{am}}{2}cos(2\omega t - \varphi). \tag{7-5}$$

From Eq. (7-5), the power of the PV array is equivalent to a DC power component and a double line frequency AC power component. Then, from the AC component, the estimated current ripple component $I_{rp}(t)$ is assumed equal to the following expression:

$$I_{rp} \triangleq -\frac{V_{gm}I_{am}}{2V_{pv}}cos(2\omega t - \varphi). \tag{7-6}$$

Eq. (7-6) differs from Eq. (5-9) in the phase-angle φ between the voltage and current of the grid because for this application, it is considered that the power factor is not unity, thus, $\varphi \neq 0$. The estimated current ripple $I_{rp}(t)$ given by (7-6) is subtracted from the current of the PV array to mitigate the current ripple component without the necessity of an additional power stage as is shown in Eq. (7-7).

$$C\frac{dV_{pv}}{dt} = I_{pv} - (d + d_0)i_a - I_{rp} \tag{7-7}$$

Following the same procedure as it was detailed in Chapter V, the equations of the model in dq frame are as follows:

$$LI_d = -RI_d + (d_d' + d_{0d})V_{pv} - V_{gd} \tag{7-8}$$

$$LI_q = -RI_q + (d_q' + d_{0q})V_{pv} - V_{gq} \tag{7-9}$$

$$C\dot{V}_{pv} = I_{pv} - (d_d' + d_{0d})I_d - (d_q' + d_{0q})I_q - I_{rd} - I_{rq} \tag{7-10}$$

where $I_d(t)$ and $I_q(t)$ are the d-axis and q-axis inverter output current components, $V_{gd}(t)$ and $V_{gq}(t)$ are the d- axis and q-axis grid voltage components, $d_{0d}(t)$ and $d_{0q}(t)$ are the constant unknown quantities in dq frame, that are adaptively estimated. $d_d'(t)$ and $d_q'(t)$, given by Eq. (7-11) and Eq. (7-12), are auxiliary control functions to decouple the dq power loops components and facilitate the model analysis [4].

$$d_d' = d_d + \frac{\omega L}{V_{pv}}I_q \tag{7-11}$$

$$d_q' = d_q - \frac{\omega L}{V_{pv}}I_d \tag{7-12}$$

$I_{rd}(t)$ and $I_{rq}(t)$ are dq components of the second harmonic current ripple for $\theta = 2\omega t$, which are defined as follows:

$$I_{rd} = -\frac{V_{gd}I_d}{2V_{pv}}cos\varphi \tag{7-13}$$

$$I_{rq} = \frac{V_{gd}I_d}{2V_{pv}}sin\varphi \tag{7-14}$$

where $\varphi = tan^{-1}\frac{I_q}{I_d}$.

7.1   Control Design

For the design, the assumptions of the system cited in section 6.1 are valid, and they are used for this scheme, with the unique difference that the q-axis reference current is obtained utilizing Eq. (7-1).

Assumption 1.- R, L, C are known constant parameters of the system.

Assumption 2. The q-axis reference current $I_{qref}(t)$ given by Eq. (7-1) is bounded and sufficiently differentiable. Thus, $I_{qref}(t)$ and $\dot{I}_{qref}(t)$ are bounded.

Assumption 3. The voltage of the grid $V_g(t)$ is measurable and sufficiently differentiable. It is sinusoidal and symmetrical. Then, the d-axis grid voltage $V_{gd}(t)$ and its derivative are bounded, and the q-axis grid voltage $V_{gq}(t)$ is zero.

Assumption 4. The reference voltage $V_{ref}(t)$ is measurable and sufficiently differentiable. Thus, $V_{ref}(t)$ and $\dot{V}_{ref}(t)$ are bounded.

Assumption 5. The current $I_{pv}(t)$ of the PV array is bounded on the condition that the voltage $V_{pv}(t)$ is bounded.

To meet with the desired currents and voltage to control the active and reactive power supplied to the grid with MPP operation, the tracking errors signals $e_d(t)$, $e_q(t)$, and $e_v(t)$ and their derivatives are defined by equations (6-1) – (6-6). The open loop system is developed substituting equations (7-8), (7-9), and (7-10) into equations (6-4), (6-5), and (6-6) respectively as follows:

$$L\dot{e}_d = -RI_d + (d'_d + d_{0d})V_{pv} - V_{gd} - L\dot{I}_{dref} \qquad (7\text{-}15)$$

$$L\dot{e}_q = -RI_q + (d'_q + d_{0q})V_{pv} - V_{gq} - L\dot{I}_{qref} \tag{7-16}$$

$$C\,\dot{e}_v = I_{pv} - (d'_d + d_{0d})I_d - (d'_q + d_{0q})I_q - I_{rd} - I_{rq} - C\dot{V}_{ref}. \tag{7-17}$$

From Eq. (7-15) and Eq. (7-16), the control functions d'_d and d'_q are designed as follows:

$$d'_d = \frac{1}{V_{pv}}\left(-K_7 e_d - \hat{d}_{0d}V_{pv} + RI_d + V_{gd} + L\dot{I}_{dref}\right) \tag{7-18}$$

$$d'_q = \frac{1}{V_{pv}}\left(-K_8 e_q - \hat{d}_{0q}V_{pv} + RI_q + L\dot{I}_{qref}\right) \tag{7-19}$$

where K_7, K_8 are positive constant control gains, and $\hat{d}_{0d}$ and $\hat{d}_{0q}$ are the estimated unknown disturbances that will be designed. Substituting Eq. (7-18) into Eq. (7-15) and Eq. (7-19) into Eq. (7-16), after some mathematical work, the following equations are obtained:

$$L\,\dot{e}_d = -K_7 e_d - \hat{d}_{0d}V_{pv} + d_{0d}V_{pv} \tag{7-20}$$

$$L\,\dot{e}_q = -K_8 e_q - \hat{d}_{0q}V_{pv} + d_{0q}V_{pv}. \tag{7-21}$$

The error signal $\tilde{d}_{0d}$ and $\tilde{d}_{0q}$ are defined as follows:

$$\tilde{d}_{0d} \triangleq d_{0d} - \hat{d}_{0d} \tag{7-22}$$

$$\tilde{d}_{0q} \triangleq d_{0q} - \hat{d}_{0q}. \tag{7-23}$$

Substituting Eq. (7-22) into Eq. (7-20) and Eq. (7-23) into Eq. (7-21) and then replacing V_{pv} from Eq. (6-3), the closed loop dynamics of the current tracking error signals are obtained:

$$L\,\dot{e}_d = -K_7 e_d + \tilde{d}_{0d}e_v + \tilde{d}_{0d}V_{ref} \tag{7-24}$$

$$L\,\dot{e}_q = -K_8 e_q + \tilde{d}_{0q}e_v + \tilde{d}_{0q}V_{ref}. \tag{7-25}$$

Substituting Eq. (7-18) and Eq. (7-19) into Eq. (7-17), along with Eq. (7-22) and Eq. (7-23), after some mathematical work, Eq. (7-26) is obtained:

$$C\dot{e}_v = -\frac{I_d}{V_{pv}}\left(-K_7 e_d + RI_d + V_{gd} + L\dot{I}_{dref}\right) - \frac{I_q}{V_{pv}}\left(-K_8 e_q + RI_q + V_{gq} + L\dot{I}_{qref}\right)$$

$$-\tilde{d}_{0d}I_d - \tilde{d}_{0q}I_q + I_{pv} - I_{rd} - I_{rq} - C\dot{V}_{ref}.$$

(7-26)

Then, $\dot{I}_{dref}$, found in Eq. (7-26) to obtain the trajectory of the d-axis reference current I_{dref}, is designed as follows:

$$\dot{I}_{dref} = \frac{K_7}{L}e_d + \frac{K_8 e_q}{L}\frac{I_q}{I_d} + \frac{K_9 e_v}{L}\frac{V_{pv}}{I_d} + \frac{V_{pv}I_{pv}}{LI_d} - \frac{C}{L}\frac{V_{pv}}{I_d}\dot{V}_{ref} - \frac{I_q}{I_d}\dot{I}_{qref} -$$

(7-27)

$$\frac{R}{L}\frac{I_q^2}{I_d} - \frac{R}{L}I_d - \frac{1}{L}V_{gd} - \frac{V_{pv}}{LI_d}\left(I_{rd} + I_{rq}\right)$$

where K_9 is a positive constant control gain. Substituting Eq. (7-27) into Eq. (7-26) the closed loop dynamics of the voltage tracking error $e_v(t)$ is obtained:

$$C\dot{e}_v = -K_9 e_v - \tilde{d}_{0d}I_d - \tilde{d}_{0q}I_q$$

(7-28)

7.2 Stability Analysis

Theorem 3: Using the closed loop error system given by equations (7-24), (7-25), and (7-28), the error signals defined in (6-1), (6-2), and (6-3), are regulated as follows:

$$e_d(t), e_q(t), e_v(t) \rightarrow 0 \ as \ t \rightarrow \infty$$

(7-29)

Proof: Choosing a non-negative Lyapunov function candidate as:

$$V_3 = \frac{1}{2}Le_d^2 + \frac{1}{2}Le_q^2 + \frac{1}{2}Ce_v^2 + \frac{1}{2}K_{ad}^{-1}\tilde{d}_{0d}^2 + \frac{1}{2}K_{aq}^{-1}\tilde{d}_{0q}^2$$

(7-30)

where K_{ad} and K_{aq} are positive constant gains. Then, the time derivative of (7-30) is as follows:

$$\dot{V}_3 = e_d L\dot{e}_d + e_q L\dot{e}_q + e_v C\dot{e}_v + K_{ad}^{-1}\tilde{d}_{0d}\dot{\tilde{d}}_{0d} + K_{aq}^{-1}\tilde{d}_{0q}\dot{\tilde{d}}_{0q}.$$

(7-31)

Assuming that d_{0d} and d_{0q} are slowly time-varying disturbances [41], the time

derivative of Eq. (7-22) and Eq. (7-23) are as follows:

$$\dot{\tilde{d}}_{0d} = -\dot{\hat{d}}_{0d} \tag{7-32}$$

$$\dot{\tilde{d}}_{0q} = -\dot{\hat{d}}_{0q} \tag{7-33}$$

The closed loop error signals are defined by equations (7-24), (7-25), and (7-28). Then,

substituting these equations into Eq. (7-31) along with Eq. (7-32) and Eq. (7-33), after

some mathematical work, the following equation is obtained.

$$\dot{V}_3 = -K_7 e_d^2 - K_8 e_q^2 - K_9 e_v^2 + \tilde{d}_{0d}\left(e_d V_{pv} - e_v I_d - \frac{1}{K_{ad}}\dot{\hat{d}}_{0d}\right)$$

$$+\tilde{d}_{0q}\left(e_q V_{pv} - e_v I_q - \frac{1}{K_{aq}}\dot{\hat{d}}_{0q}\right) \tag{7-34}$$

where the update laws for the unknown disturbances $\hat{d}_{0d}$ and $\hat{d}_{0q}$ are designed as

follows:

$$\dot{\hat{d}}_{0d} = K_{ad}\left(e_d V_{pv} - e_v I_d\right) \tag{7-35}$$

$$\dot{\hat{d}}_{0q} = K_{aq}\left(e_q V_{pv} - e_v I_q\right). \tag{7-36}$$

Substituting Eq. (7-35) and Eq. (7-36) into Eq. (7-34), after some mathematical work, the

following equation is obtained:

$$\dot{V}_3 = -K_7 e_d^2 - K_8 e_q^2 - K_9 e_v^2. \tag{7-37}$$

Given by Eq. (7-30) and Eq. (7-37), the error signals $e_d(t)$, $e_q(t)$, and $e_v(t)$ are square

integrable and bounded, and that $\tilde{d}_{0d}(t)$, $\tilde{d}_{0q}(t)$ are bounded. From *Assumption 4*, V_{ref} is

bounded then, Eq. (6-2) can be used to show that V_{pv} is bounded. As it was shown that V_{pv}

is bounded, from *Assumptions* 5, I_{pv} is bounded. From *Assumptions* 3 and 5, and from

the fact that the PV power is equal to the grid power from the power balance relationship, I_d is bounded. Therefore, from Eq. (6-1) along with the above boundedness statements, I_{dref} is bounded. From *Assumption* 2 and knowing that $e_q(t)$ is bounded, Eq. (6-2) is utilized to show that the current I_q is bounded. From *Assumption* 2, $\dot{I}_{qref}$ is bounded. From *Assumption* 3 and knowing that I_d and V_{pv} are bounded, Eq. (7-13) and Eq. (7-14) can be utilized to show that I_{rd} and I_{rq} are bounded. From *Assumption* 4, along with the above boundedness statements, Eq. (7-27) can be utilized to show that $\dot{I}_{dref}$ is bounded. From *Assumption* 5 along with the above boundedness statements, Eq. (7-35) and Eq. (7-36) can be utilized to show that $\hat{d}_{0d}$ and $\hat{d}_{0q}$ are bounded. Since $\hat{d}_{0d}$ and $\hat{d}_{0q}$ are shown to be bounded and knowing that $\tilde{d}_{0d}$ and $\tilde{d}_{0q}$ are bounded, Eq. (7-22) and Eq. (7-23) are utilized to show that d_{0d} and d_{0q} are bounded. Using the above boundedness statements, from Eq. (7-18) and Eq. (7-19) it can be proven that d_d' and d_q' are bounded. Similarly, based on the above boundedness statements, from equations (7-8), (7-9), and (7-10) it can be shown that $\dot{I}_d$, $\dot{I}_q$, and $\dot{V}_{pv}$ are bounded. Finally, from *Assumptions* 3, 4, and 5 along with the above boundedness statements, equations (7-15), (7-16), and (7-17) are utilized to show that $\dot{e}_d$, $\dot{e}_q$, and $\dot{e}_v$ are bounded. Therefore, all the signals of the closed loop system are bounded. From Barbalat's Lemma [51], it can be shown that the signals $\left(e_d(t), e_q(t), e_v(t) \right) \to 0$ *as* $t \to \infty$. Thus, the proof of *Theorem 3* is completed.

7.3 Simulation Results

The parameters of the PV system are the same as those presented in Table 6.1 and Table 6.2 except K_4, K_5, K_6, which are replaced by $K_7 = 16$, $K_8 = 40$, and $K_9 = 1$

respectively. Additionally, the values of the control gains of the adaptive control are designed as $K_{ad} = 0.005$ and $K_{aq} = 0.02$.

First, to see the performance of the adaptive control, an external known constant value of 0.2 was added to the duty ratio control signal in dq frame $(d_d + 0.2, d_q - 0.2)$ at t=0.3 seconds to simulate an imperfect switching time. The irradiance of the PV array is set at 800 W/m². At the rated grid voltage, the d-axis component of the grid voltage V_{dg} is 170V, then, from Eq. (7-1); the q-axis reference current $I_{qref}(t)$ is zero. Figure 7.1 shows the estimated signals $\hat{d}_{0d}$ and $\hat{d}_{0q}$. It can be seen that the signals are estimated to the assumed known values with a stabilization time of approximately 0.12 seconds.
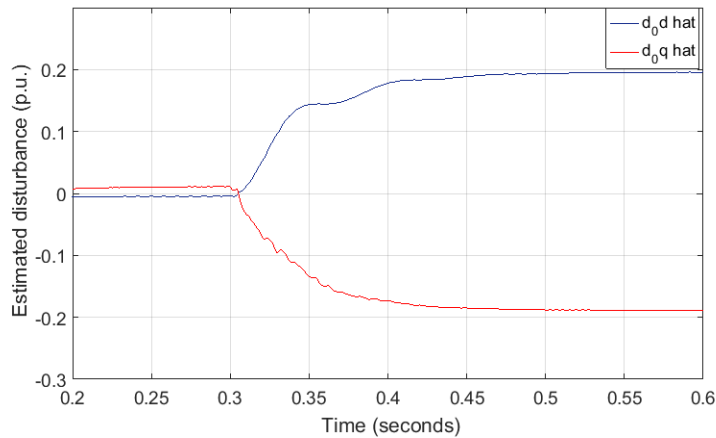

Figure 7.1 Estimated signals $\hat{d}_{0d}$ and $\hat{d}_{0q}$ utilizing adaptive control

To see the effects of the emulated imperfect switching, Figure 7.2 a) shows the grid power without the adaptive controller. It can see be seen that the reactive power settles to a value different than zero after the disturbance is added even though the reference current $I_{qref}(t)$ is zero to guarantee unity power factor. Figure 7.2 b) shows the grid power with the adaptive control. It is clear that the reactive power is zero after the disturbance is added, demonstrating the effectiveness of the proposed nonlinear controller combined

88

with adaptive control to diminish the unknown disturbance, therefore keeping the power factor at the desired value.
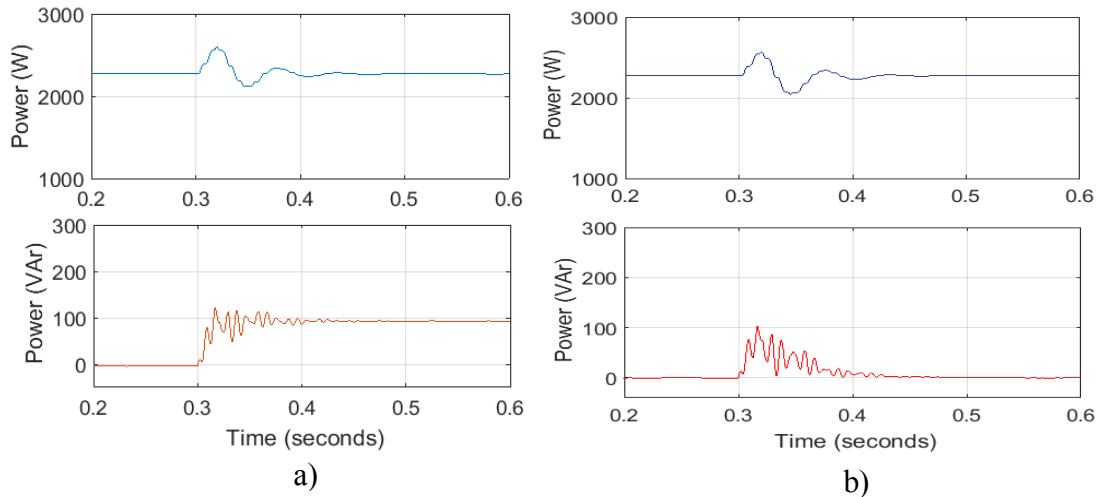

Figure 7.2 Grid active and reactive power: a) without adaptive control, b) with adaptive control

Second, the irradiance was changed in steps from 0 to 600 to 1000, and back to 800 W/m^2 at time t =0, 0.3, 0.6 seconds respectively at a temperature of 25 ^{0}C to see the performance of the proposed controller to sudden changes in atmospheric conditions. The current $I_{qref}(t)$ was set to zero to obtain unity power factor. Figure 7.3 shows the response of the PV power, which power values are close to the ideal maximum values.
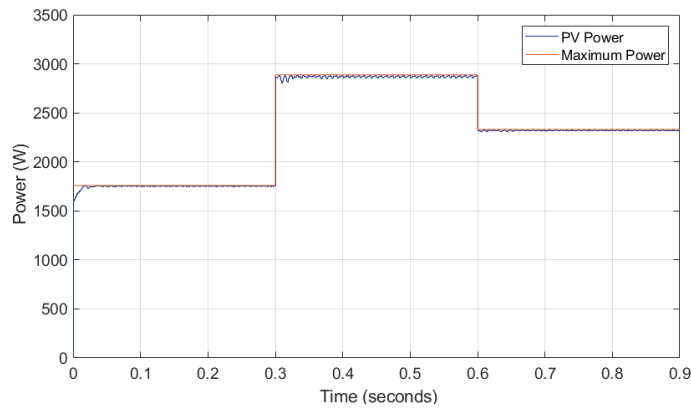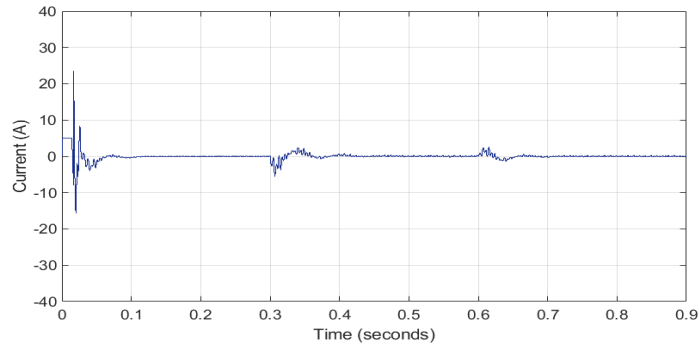

Figure 7.3 PV power and maximum power

The current tracking errors $e_d(t)$ and $e_q(t)$, and the voltage tracking error $e_v(t)$ are shown in Figure 7.4. It shows that the tracking errors are approximately regulated to zero showing the effectiveness of the nonlinear controller.

a)
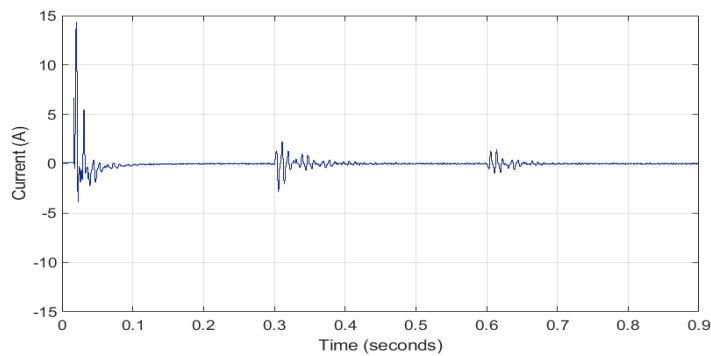
b)
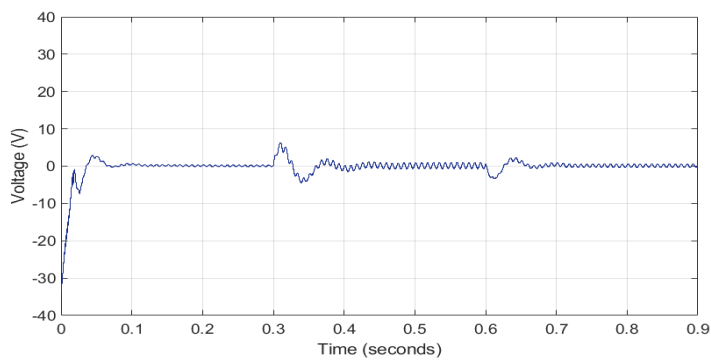
c)

Figure 7.4 Tracking error signals a) $e_d(t)$, b) $e_q(t)$, c) $e_v(t)$

Figure 7.5 shows the d-axis and q-axis current components, both with their corresponding reference currents. This figure shows that current $I_d(t)$ follows the reference current

$I_{dref}(t)$, trajectory obtained utilizing Eq. (7-27) and the current $I_q(t)$ follows the reference current $I_{qref}(t)$, which is set to zero to ensure unity power factor.
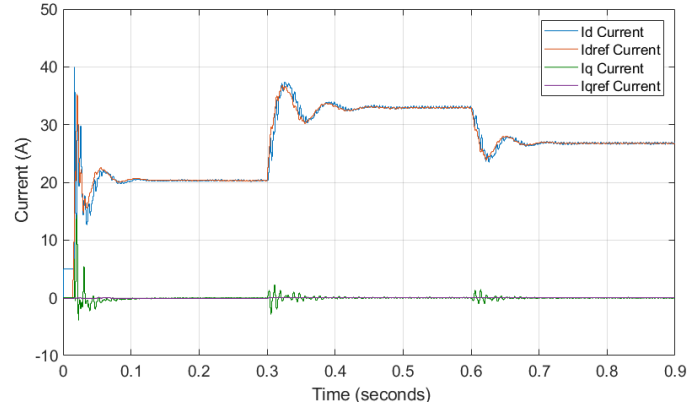
Figure 7.5 $I_d(t)$ and $I_q(t)$ currents with $I_{dref}(t)$ and $I_{qref}(t)$ reference currents

The PV voltage and the reference voltage, which was obtained using the INC algorithm, are shown in Figure 7.6. From this figure, it is clear that the PV voltage follows the reference voltage, and it is kept steady even though the rapid changes of the irradiance.

Figure 7.6 PV voltage $V_{pv}(t)$ and reference voltage $V_{ref}(t)$

The active and reactive power injected into the grid is shown Figure 7.7. It can be seen that active power supplied to the grid varies as the irradiance changes while the reactive power is approximately zero to obtain unity power factor on the grid side as it was desired.

91
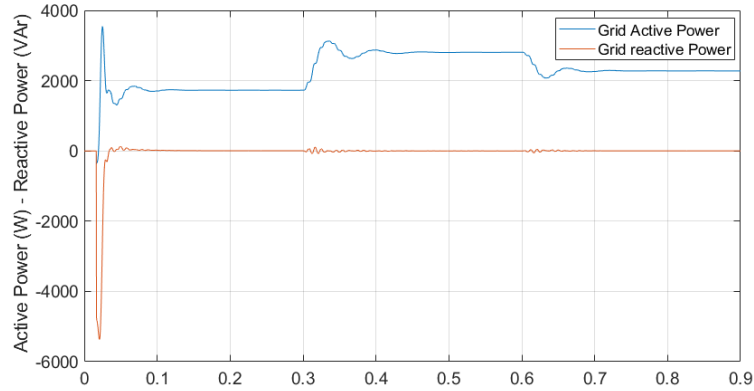
Figure 7.7 Active and reactive power supplied to the grid

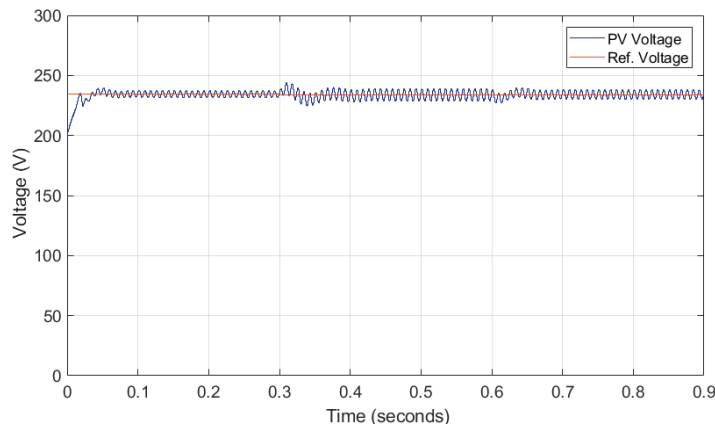To demonstrate that the power factor is unity on the grid side, Figure 7.8 shows the grid voltage and current for various values of irradiance. It is clear that the grid voltage and current are sinusoidal and they are in phase, thus showing that the power factor is unity as it was desired.
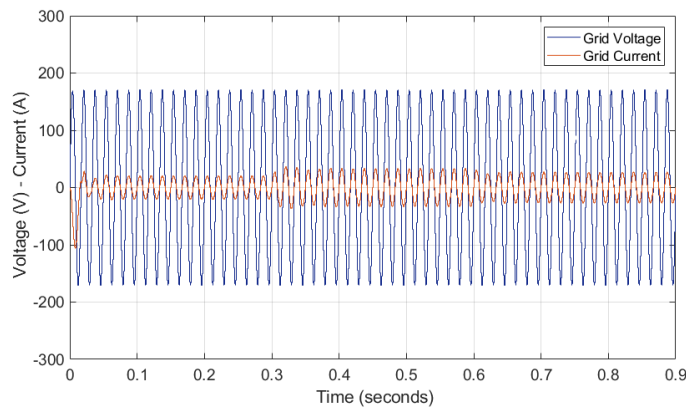
Figure 7.8 Grid voltage and current for various values of irradiance

Figure 7.9 shows a zoom in version of Figure 7.8. It is clear to see that besides that the voltage and the current are in phase, the time that the system takes to obtain the new steady state after a step change of the irradiance is approximately 0.12 seconds. In Figure 7.9, it can be seen the transient response of the grid current when the irradiance suddenly

92

changes from 600 W/m^2 to 1000 W/m^2 at time t=0.3 seconds. Figure 7.10 shows the

harmonic content of the grid current at 600 W/m^2. The THD of 1.84% meets the IEEE-

519 standard requirements.
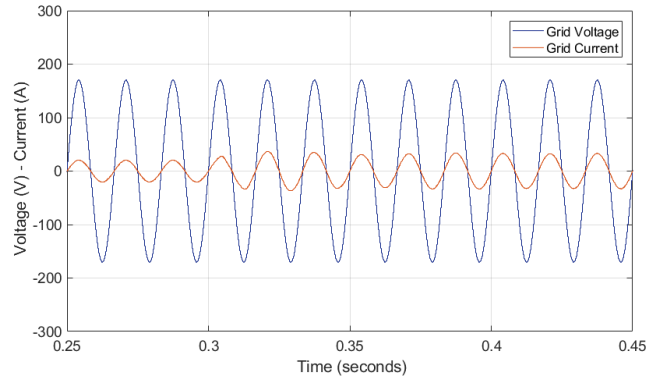
Figure 7.9 Grid voltage and current. Time range from (0.25, 0.45 seconds)
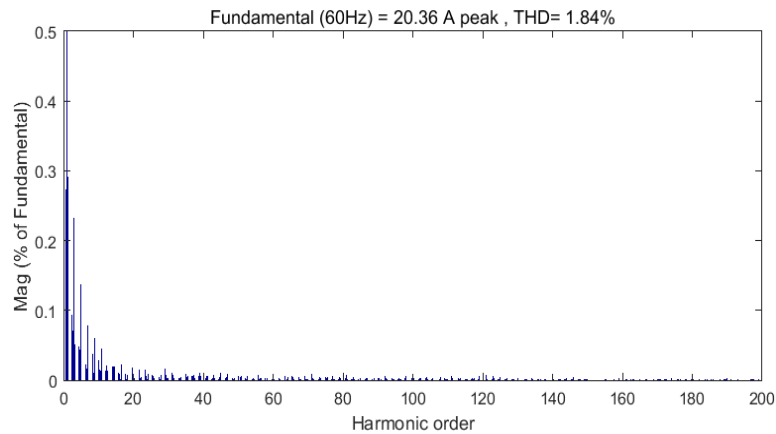

Figure 7.10 Grid current harmonic components at 600 W/m^2

A comparison of the obtained results with those found in Section 6, shows that the

proposed nonlinear control with adaptive control when unknown disturbances appear in

the circuit is more precise, as it was shown in Figure 7.2. Additionally, it was

demonstrated that the tracking errors are close to zero as it was desired, therefore showing

the performance of the proposed system. The settling time is approximately 120 [ms.] vs.

50 [ms.] of the nonlinear control without adaptive compensation presented in Section 6. In

the proposed strategy with adaptive control, the unknown disturbances are estimated. Thus, all the signals reach their steady state value as the estimator converges to its final value. As can be seen in Figure 7.11, the time that the update laws takes to estimate the unknown disturbances due to fast changes of the irradiance is approximately 120 [ms.].
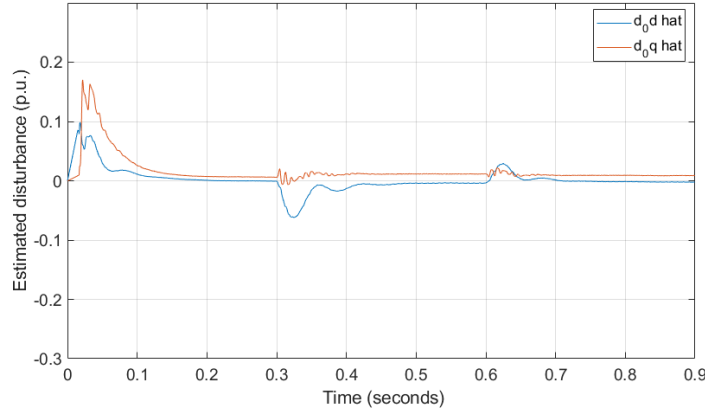
Figure 7.11 Transient response of estimated disturbance

Finally, a low voltage ride through (LVRT) event was introduced as a mean to demonstrate the effectiveness of the controller in supplying active and reactive power to the grid. A voltage sag of 20% was emulated from t=0.2 to t=0.5 seconds maintaining a constant maximum active power, where Eq. (7.1) was utilized to obtain the q-axis reference current and therefore the required reactive power. The voltage and current of the grid are shown in Figure 7.12. An expanded version is shown in Figure 7.13. From Figure 7.13a), it can be seen that; before the voltage sag event from t=0 to t=0.2 seconds, the current is sinusoidal and in phase with the voltage as desired. From t=0.2 to t=0.5 seconds, the current is still sinusoidal, but it is lagging from the voltage showing the injection of reactive power into the grid as desired. After the perturbation ends at t=0.5 seconds, again the current is in phase with the voltage as it can be seen in Figure 7.13b).
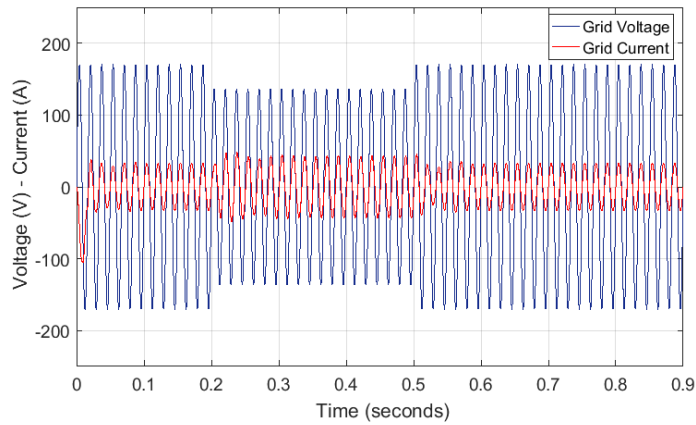
Figure 7.12 Grid voltage and current during an LVRT event
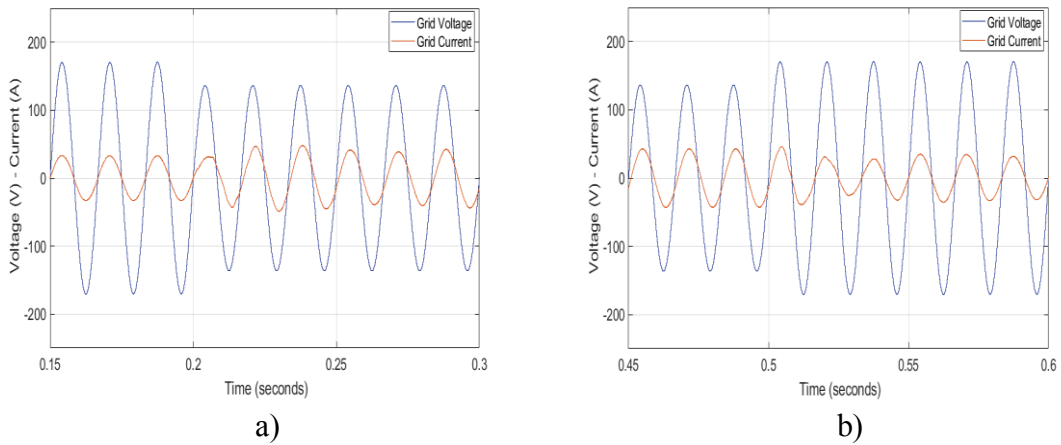
Figure 7.13 Grid voltage and current a) before LVRT, b) after LVRT event

Additionally, the active and reactive power supplied to the grid is shown in Figure 7.14. It can be seen that the active power is constant at its maximum value and the grid is receiving reactive power from the inverter during the LVRT event, therefore demonstrating that the proposed nonlinear control approach is effective and robust to a sudden change of the grid voltage.
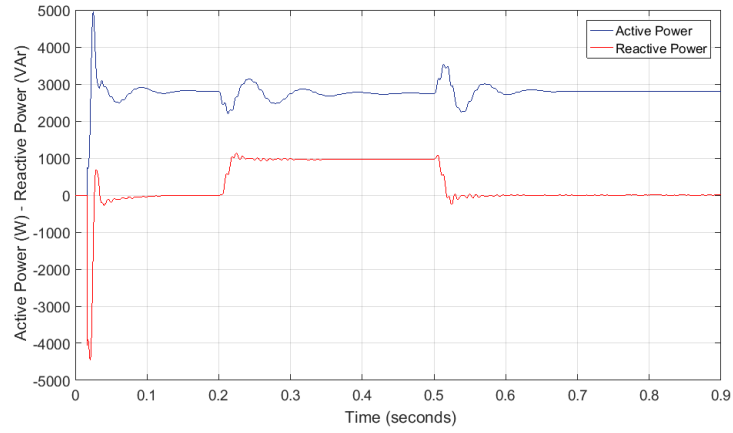
Figure 7.14 Grid active and reactive power during an LVRT event

CHAPTER VIII

CONCLUSIONS

The system performance was evaluated regarding tracking performance, stability, and system dynamics. The single-stage three-phase PV system and single-stage single-phase PV system, both with Lyapunov-based nonlinear control, were shown to be successful in tracking the reference voltage for maximum power operation without the necessity of an additional power converter stage. The novel trajectory generated online to obtain the d-axis reference current goes to an equilibrium point given by the maximum active power generated by the PV array. The proposed system was also successful in controlling the active and reactive power of the PV system, therefore compensating the reactive power required by the load to obtain unity power factor on the grid side. Moreover, the grid current showed low harmonic components with a total harmonic distortion below the values required by the IEEE-519 standard.

The single-stage three-phase grid-connected PV system and the single-stage single-phase grid-connected PV system analyzed in $dq0$ frame with Lyapunov-based nonlinear control showed effectiveness and robustness to fast changes in the irradiance and the load. Furthermore, for the case of single-stage single-phase scheme, it was successfully shown that the system could maintain the power factor approximately to unity, as well as the system could inject reactive power into the grid giving support to the grid in case of an LVRT event.

The proposed method to mitigate the current ripple in the single-phase scheme was effective, showing a reduction of the current ripple of approximately 40% therefore, decreasing the power loss of the PV array. Additionally, the adverse effect of unknown disturbances that physically could appear in the circuit was mitigated using adaptive control to estimate the unknown disturbances.

REFERENCES

[1] M. H. Rashid, *Alternative Energy in Power Electronics*, 1st ed. Butterworth-Heinemann, 2014.

[2] S. Kouro, J. I. Leon, D. Vinnikov, and L. G.Franquelo. "Grid-Connected Photovoltaic Systems: An Overview of Recent Research and Emerging PV Converter Technology," *IEEE Industrial Electronics Magazine*, March. 2015, pp. 47-61.

[3] J. M. Carrasco, et al. "Power-Electronic Systems for the Grid Integration of Renewable Energy Sources: A survey," *IEEE Transactions on Industrial Electronics,* vol. 53, no, 4, pp. 1002-1016, Aug. 2006.

[4] R. Kadri, J. P. Gaubert, and G. Champenois, "An Improved Maximum Power Point Tracking for Photovoltaic Grid-Connected Inverter Based on Voltage-Oriented Control," *IEEE Trans. Industrial Electronics*, vol. 58, no. 1, pp. 66-75, 2011.

[5] H. Zhang, H. Zhou, J. Ren, W. Liu, S. Ruan, and Y. Gao, "Three-Phase Grid-Connected Photovoltaic System with SVPWM Current Controller," in *Proc. of Power Electronics and Motion Conference, IPEMC*, 2009*,* pp 2161-2164.

[6] G. Tsengenes, G. Adamidis, "Investigation of the Behavior of a Three Phase Grid-Connected Photovoltaic System to Control Active and Reactive Power," *Electric Power System Research*, vol. 81, Issue 1, pp. 177-184, Jan 2011.

[7] M. F. Schonardie, D. C. Martins, "Three-Phase Grid-Connected Photovoltaic System with Active And Reactive Power Control Using dq0 Transformation," in *Proc. of Power Electronics Specialists Conference*, PESC, 2008, pp.1202-1207.

[8]   Y. Huang, M. Shen, F. Z. Peng, J. Wang, "Z-Source Inverter for Residential Photovoltaic Systems," *IEEE Transactions on Power Electronics*, vol. 21, no. 6, pp. 1776-1781, 2006.

[9]   B. Alajmi, K. Ahmed, G. Adam, and B. Williams, "Single-Phase Single-Stage Transformerless Grid-Connected PV System," *IEEE Transactions on Power Electronics* , vol. 28, no. 6, pp. 2664-2676, 2013.

[10] B. Crowhurst, E.F. El-Saadany, L. El Chaar, and L.A. Lamont, "Single-Phase Grid-Tie Inverter Control using DQ Transform for Active and Reactive Load Power Compensation," in *Proc. of Power and Energy Conference,* PECon, 2010*, pp 489-494.

[11] M. Ciobotaru, R. Teodorescu and F. Blaabjerg, "Control of Single-Stage Single-Phase PV Inverter," in *Proc. of Power Electronics and Applications European Conference, EPE*, 2005, pp. 1-6.

[12] F. El Aamri, H. Maker, A. Mouhsen , M. Harmouchi, "A New Strategy to Control the Active and Reactive Power for Single Phase Grid-Connected PV Inverter," in *Proc. of Renewable and Sustainable Energy Conference,* IRSEC, 2015*, pp 1-6.

[13] W. Sripipat and S. Po-Ngam , " Simplified Active Power and Reactive Power Control with MPPT for Single-Phase Grid-Connected Photovoltaic Inverters," in *Proc. of Electrical Engineering/Electronics Conference*, ECTI-CON, 2014, pp.1-4.

[14] N. E. Zakzouk, A. K. Abdelsalam, A. A. Helal, and B. W. Williams, "PV Single-Phase Grid-Connected Converter: DC-Link Voltage Sensorless Prospective," *IEEE Journal of Emerging and Selected Topics in Power Electronics*, vol. 5, no. 1, march 2017.

[15] M. Islam, M. Nadarajah, and J. Hossain, "Multifunctional Control of Single-Phase Transformerless PV Inverter Connected to a Distribution Network," in *Proc. of Power Engineering Conference*, AUPEC, 2016, pp. 1-6.

[16] B. Crăciun, T. Kerekes, D. Séra, R.Teodorescu, "Overview of Recent Grid Codes for PV Power Integration," in *Proc. of Optimization of Electrical and Electronic Equipment*, OPTIM, 2012, pp. 959-965.

[17] D. Sera, T. Kerekes, R. Teodorescu, and F. Blaabjerg,"Improved MPPT Algorithms for Rapidly Changing Environmental Conditions," in *Proc. of Power Electronics and Motion Conference,* EPE-PEMC, 2006, pp 1614-1619.

[18] A. Mohapatra, B. Nayak, B. Misra, "Model Validation and Maximum Power Point Tracking of Photovoltaic Module," in *Proc. of Power and Energy Systems: Towards Sustainable Energy*, PESTSE, 2014, pp 1-5.

[19] T. Esram, and P. L. Chapman, "Comparison of Photovoltaic Array Maximum Power Point Tracking Techniques," *IEEE Transactions on Energy Conversion*, vol. 22, pp. 439-499, June 2007.

[20] M. A. Farahat, M. A. Enany, and A. Nasr, " Assessment of Maximum Power Point Tracking Techniques for Photovoltaic System Applications," *Journal of Renewable and Sustainable Energy, American Institute of Physics*, vol.7, issue 4, pp.1-7, 2015.

[21] Z. Dejia, Z. Zhengming, M. Eltawil and Y. Liqiang, "Design and Control of a Three-Phase Grid-Connected Photovoltaic System with Developed Maximum Power Point Tracking," in *Proc. of IEEE Applied Power Electronics Conference ,* 2008, pp. 973-979.

[22] F. Liu, S. Duan, F. Liu, B. Liu, and Y. Kang, "A Variable Step Size INC MPPT method for PV Systems," *IEEE Transactions on Industrial Electronics*, vol.55, No. 7, July 2008, pp.2622-2628.

[23] D. Sera, L. Mathe, T. Kerekes, S. V. Spataru, and R. Teodorescu," On the Perturb-and-Observe and Incremental Conductance MPPT Methods for PV Systems," *IEEE Journal of Photovoltaic*, vol.3 No.3, July 2013, pp.1070-1078.

[24] T. K. Roy, M. A. Mahmud, M. J. Hossain, "Nonlinear Backstepping Controller Design for Sharing Active and Reactive Power in Three-Phase Grid-Connected Photovoltaic Systems," in *Proc. of Power Engineering Conference,* AUPEC, 2015, pp. 1-5.

[25] C. Aouadi, A. Abouloifa, A. Hamdoun, Y. Boussairi, "Nonlinear controller Design for Single-Phase Grid-Connected Photovoltaic Systems," in *Proc. of Renewable and Sustainable Energy Conference,* IRSEC, 2015, pp. 1-5.

[26] H. El Fadil, F. Giri, J.M. Guerrero, "Grid-Connected of Photovoltaic Module using Nonlinear Control," in *Proc. of Power Electronics for Distributed Generation*, PEDG, 2012, pp. 119 - 124.

[27] A. Elmahjoub, A. Alilane, M. Rachik, El Labriji, A. Abouloifa, A. Essadki, " A Non-Linear Controller for Single-Phase DC-AC Power Converter using in the Grid-Connected Photovoltaic," in *Proc. of International Conference Complex Systems,* ICCS, 2012, pp. 1-6.

[28] N. Skik, A. Abbou, "Robust Adaptive Integral Backstepping control for MPPT and UPF of PV System Connected to the Grid," in *Proc. of Renewable Energy Congress*, IREC, 2016, pp. 1-6.

[29] D. Lauria, M. Coppola, "Design and control of an advanced PV inverter," *Solar Energy* vol. 110, pp. 533–542, 2014.

[30] D. Gonzales, C. A. Ramos, and R. Giral, "Improved Design of Sliding-Mode Controllers Based on the Requirements of MPPT Techniques," *IEEE Transaction on Power Electronics,* vol. 31, no.1, pp. 235-247, January 2016.

[31] IS. Kim, "Sliding Mode Controller for the Single-Phase Grid-Connected Photovoltaic System," *Applied Energy*," vol. 83, pp. 1101–1115, 2006.

[32] R. Majdoul, E. Abdelmounim, M. Aboulfatah, A. Abouloifa, "The Performance comparative of Backstepping, Sliding Mode and PID controllers designed for a

single-phase inverter UPS," in *Proc. of Multimedia Computing and Systems,* ICMC, 2014, pp. 1-5.

[33] P. Henriquez, S. Cuevas, J. Rohten, S. Araya, V. Esparza, G. Sanhueza, and P.Melin, "Nonlinear Control for Power Converters Injecting the Maximum Power from PV Arrays," in *Proc. of International Conference of Automatica,* ICA-ACCA, 2016, pp. 1-6.

[34] M. A. Mahmud, H. R. Pota, M. J. Hossain, and N. K. Roy, "Robust Partial Feedback Linearizing Stabilization Scheme for Three-Phase Grid-Connected Photovoltaic Systems," *IEEE Journal of Photovoltaics*, vol.4 No. 1, pp. 422-431, Jan. 2014.

[35] M. A. Mahmud, H. R. Pota, M. J. Hossain, "Nonlinear Current Control Scheme for a Single-Phase Grid-Connected Photovoltaic System*," IEEE Transactions on Sustainable Energy*, vol. 5, no. 1, pp. 218-227, 2014.

[36] D. Lalili, A. Mellit, N. Lourci, B. Medjahed, E.M. Berkouk, "Input output feedback linearization control and variable step size MPPT algorithm of a grid-connected photovoltaic inverter," *Renewable Energy* vol. 36, pp. 3282-3291, 2011.

[37] IS. Kim, "Robust maximum power point tracker using sliding mode controller for the three-phase grid-connected photovoltaic system," *Solar Energy*, vol. 81, pp. 405–414, 2007.

[38] El Fadili , F. Giri, A. El Magri, "Reference Voltage Optimizer for Maximum Power Point Tracking in Three-phase Grid-Connected Photovoltaic Systems," *International Journal of Electrical Power & Energy Systems*, vol. 60, pp. 283–301, Sep. 2014.

[39] A. Yahya, H. El Fadil, J. M. Guerrero, F. Giri, and H. Erguig, "Three-Phase Grid-Connected of Photovoltaic Generator Using Nonlinear Control," in *Proc. of Conference in Control Applications,* CCA, 2014, pp 879-884.

[40] F. Blaabjerg, R. Teodorescu, M. Liserre, and A. V. Timbus, "Overview of Control and Grid Synchronization for Distributed Power Generation Systems," *IEEE Transactions on Industrial Electronics*, vol. 53, no.5, pp. 1398-1409, Oct. 2006.

[41] M. Mohebbi, M. L. McIntyre and J. Latham, P. Rivera, "Nonlinear Control of Standalone Inverter with Unbalanced, Nonlinear Load," in *Proc. of Power and Energy Conference,* PECI, 2017, pp. 1-7.

[42] Y. Yang, P. Enjeti, F. Blaabjerg, H. Wang, "Wide Scale Adoption of Photovoltaic Energy," *IEEE Industrial Electronics Magazine*, October 2015, pp. 22-31.

[43] T. Wu, C. Chang, L. Lin, and C. Kuo, "Power Loss Comparison of Single-Stage and Two-Stage Grid-Connected Photovoltaic Systems," *IEEE Transactions on Energy Conversion*, vol. 26, no. 2, pp. 707-715, 2011.

[44] N. A. Ninad and L. A. Lopes, "Operation of Single-Phase Grid-Connected Inverters with Large DC Bus Voltage Ripple," in *Proc. of Electrical Power Conference, CEP*, 2007, pp. 172-176.

[45] S. Lee, T. An, and H. Chay, "Mitigation of Low Frequency AC Ripple in Single-Phase Photovoltaic Power Conditioning Systems," *Korean Institute of Power Electronics Journal of Power Electronics*, vol.10, Issue 3, pp. 328-333, May 2010.

[46] R. Zhang, M. Cardinal, P. Szczesny and M. Dame, "A Grid Simulator with Control of Single-Phase Power Converters in D-Q Rotating Frame," in *Proc. of IEEE Power Electronics Specialists,* 2002, pp. 1431-1463.

[47] M. Villalva, J. Gazoli, and E. Filho, "Comprehensive Approach to Modeling and Simulation of Photovoltaic Arrays," *IEEE Transactions on Power Electronics*, vol. 24, no.5, pp. 1198-1208, May 2009.

[48] A. Kwasinski, W. Weaver, R. S. Balong, *Microgrids and other Local Area Power and Energy Systems*, 1st ed. Cambridge University Press, 2016.

[49] E. Cadaval, G. Spagnuolo, C. Ramos, T. Suntio, W. Xiao, "Grid-Connected Photovoltaic Generation Plants: Components and Operation," *IEEE Industrial Electronics Magazine*, September 2013, pp. 6-20.

[50] D. Cruz, "Analysis of a Three-Phase Grid-Connected PV Power System using a Modified Dual-Stage Inverter," *ISRN Renewable Energy*, pp. 1-18, 2013.

[51] J.E. Slotine, W. Li, *Applied Nonlinear Control*, Prentice Hall, 1991.

[52] H. J. Marquez, *Nonlinear Control System,* John Wiley & Sons, 2003.

[53] K. Khalil, *Nonlinear Control*, 1st. ed. Pearson Education, 2015.

[54] W. Dixon, A. Behal, D. Dawson, S. Nagarkatti, *Nonlinear Control of Engineering Systems:Lyapunov-Based Approach*, 3rd. ed. Birkhauser, 2003.

[55] V. Rao, A. Jain, K. Reddy, and A. Behal, "Nonlinear Control of a Single Phase Unity Power factor Rectifier: Design, Analysis, and Experimental Results," *IEEE Transactions on Control System Technology*, vol. 16, no. 6, pp. 1301-1307, 2008.

[56] N. Mohan, *Electrical Machines and Drives,* 2nd. ed. John Wiley & Sons, 2013.

[57] P. Krause, O. Wasynczuk, S. Sudhoff, *Analysis of Electrical Machinery and Drive System,* 2nd. ed. IEEE Press, John Wiley & Sons, 2002.

[58] Y. Yang, F. Blaabjerg, and Z. Zou, "Low-Voltage Ride-Through of Single-Phase Transformerless Photovoltaic Inverters," *IEEE Transactions on Industry Applications*, vol. 50, no. 3, pp. 1942-1950, 2014.

[59] M. Islam S. Mekhilef, M. Hasan, "Single phase transformerless inverter topologies for grid-tied photovoltaic system: A review," *Renewable and Sustainable Energy Reviews* vol. 45, pp. 69–86, 2015.

[60] Y. Yang, F. Blaabjerg, and Z. Zou, "Benchmarking of Grid Fault Modes in Single-Phase Grid-Connected Photovoltaic Systems," *IEEE Transactions on Industry Applications*, vol. 49, no. 5, pp. 2167-2176, 2013.

CURRICULUM VITAE

NAME: Pablo R. Rivera

ADDRESS: Department of Electrical and Computer Engineering

W.S. Speed Hall Room 207

University of Louisville

Louisville, Ky 40292

Email: pabli2009to@hotmail.com

DOB: Cayambe, Ecuador, October, 31, 1959

EDUCATION
& TRAINING: B.S. Electronic and Control Engineering

National Polytechnic University, Quito-Ecuador

1978-1984

M.S. Power Electronics

University of Bradford, England

1992-1993

Ph.D. Electrical Engineering

University of Louisville

2014-2018

AWARDS: Ecuadorian Secretary of Science and Technology; scholarship for

university teachers, 2014.

PUBLICATIONS:

[1] P. R. Rivera, M. L. McIntyre, M. Mohebbi, and J. Latham, "Single-Stage Three-Phase Grid-Connected Photovoltaic System with Maximum Power Tracking and Active and Reactive Power Control based on Nonlinear control," in *Proc. of Energy Conversion Congress and Exposition, ECCE*, October 2017, pp. 1-7.

[2] P. R. Rivera, M. L. McIntyre, M. Mohebbi, and J. Latham, " Nonlinear Control for Single-Stage, Single-Phase Grid-Connected Photovoltaic Systems," in *Proc. of Control and Modelling for Power Electronics, COMPEL*, July 2017.

[3] P. R. Rivera, M. L. McIntyre, M. Mohebbi, and J. Latham, "Single-Stage Single-Phase Grid-Connected Photovoltaic System with Current Ripple Mitigation based on Nonlinear Control," in *Proc. of International Conference on Energy and Environment CIEM*, October 2017, pp. 321-325.

[4] M. Mohebbi, M. L. McIntyre, J. Latham, and P. R. Rivera, "A Filter-Based Control of an H-Bridge inverter with output LC filter," in *Proc. of American Control Conference, ACC*, May 2017.

[5] M. Mohebbi, M. L. McIntyre, J. Latham, and P. R. Rivera, "A Filter-Based Controller for Buck Converter," in *Proc. of Control and Modelling for Power Electronics, COMPEL*, July 2017.

[6] M. Mohebbi, M. L. McIntyre, J. Latham, and P. R. Rivera, "Nonlinear Control of Standalone Inverter with Unbalanced, Nonlinear Load," in *Proc. of Power and Energy Conference, PECI* , Febryary 2017, pp. 1-7.

[7] M. Alqatamin, M. L. McIntyre, J. Latham, P. R. Rivera, and N. Hawkins "Nonlinear Adaptive Control Design for Power System with STATCOM device," paper acccepted to be presented in *American Control Conference, ACC*, June 2018.